A Structural, Geochronological & Geochemical Investigation of the Abt Schist; Ad Dawadimi Terrane; Central Saudi Arabia.

Christopher J. Lewis

E-mail address: christopher.lewis@student.adelaide.edu.au

Tectonics, Resources and Exploration (TRaX), University of Adelaide, SA 5005, Australia

Supervisors: Alan Collins, Galen Halverson & John Foden

Table of Contents

ABSTRACT **3**

INTRODUCTION **5**

GEOLOGICAL SETTING **7**

METHODS **8**

STRUCTURE 8
Field Work/Data Collection *8*
GEOCHRONOLOGY 8
U-Pb Laser Ablation Inductively Coupled Plasma Mass Spectrometry (LA-ICPMS) *8*
$^{40}Ar/^{39}Ar$ Muscovite Analyses *9*
GEOCHEMISTRY 10
Major Elements *10*
Trace Elements *10*
Sm-Nd Thermal Ionisation Mass Spectrometry (TIMS) *11*

RESULTS **12**

STRUCTURE 12
Maps and Structural Representations *12*
GEOCHRONOLOGY 13
U-Pb Laser Ablation Inductively Coupled Plasma Mass Spectrometry (LA-ICPMS) *13*
$^{40}Ar/^{39}Ar$ Muscovite Analyses *16*
GEOCHEMISTRY 16
Metasedimentary Rocks *16*
Igneous Rocks *18*
Sm-Nd Thermal Ionisation Mass Spectormetry (TIMS) *18*

DISCUSSION **21**

AGE OF METASEDIMENTARY PROTOLITHS 21
PROVENANCE OF METASEDIMENTARY ROCKS & TECTONIC ENVIRONMENT OF THE ABT SCHIST 22
Provenance of Metasedimentary Rocks *22*
Tectonic Environment *23*
STRUCTURAL EVOLUTION OF THE AD DAWADIMI TERRANE 24
TECTONIC EVOLUTION OF THE AD DAWADIMI TERRANE 25

CONCLUSION **28**

ACKNOWLEDGEMENTS **29**

REFERENCES **30**

FIGURE CAPTIONS **33**

FIGURES **37**

TABLES **76**

A Structural, Geochronological & Geochemical Investigation of the Abt Schist; Ad Dawadimi Terrane; Central Saudi Arabia.

Christopher J. Lewis

E-mail address: christopher.lewis@student.adelaide.edu.au

Tectonics, Resources and Exploration (TRaX), University of Adelaide, SA 5005, Australia

Abstract

The Ad Dawadimi Terrane lies on the eastern margin of the Arabian-Nubian Shield between the ~800-600 Ma Ar Rayn Terrane to the east and the Palaeo-Neoproterozoic (1800-630 Ma) Afif Terrane to the west. The Ad Dawadimi Terrane is considered to be one of the most homogeneous terranes of the Arabian Shield and is dominated by the Abt Schist, a greenschist facies metamorphic unit of fine grained sandstones and siltstones. Structural data shows variations in the foliations between the Ad Dawadimi Terrane's eastern and western margins. The east is dominated by west-south-west verging sub-horizontal, moderately inclined, open, asymmetrical folds with a sub-horizontal to gentle south-south-east plunge. The western margin, although less well constrained, is dominated by folds with a west-north-west vergence, sub-horizontal, moderately – gently inclined, open, asymmetrical geometry; with a north-east south-west extensional component. $^{206}Pb/^{238}U$ data of Abt Schist samples within the Ad Dawadimi Terrane give a maximum depositional age of 594 ± 14 Ma (2σ error at ≥95-105% concordance). Two $^{40}Ar/^{39}Ar$ metamorphic muscovite step-heating analyses yield peak metamorphic of ages ~616 ± 3 Ma and ~613 ± 6 Ma thus being within error of the youngest $^{206}Pb/^{238}U$ detrital zircon age. A number of zircon grains yield $^{206}Pb/^{238}U$ ages >1 Ga suggest a Mesoproterozoic, or older, influence on the source for the Abt sediments. This is supported by TIMS T_{DM} model ages ~1154 ± 19 Ma suggesting Abt Schist protolith sediments were

influenced by late Mesoproterozoic sources. Sedimentary geochemical analyses of immobile elements suggest sediments derived from the Afif Terrane were deposited into a fore-arc setting above a west dipping subducting slab. The very short time period between deposition and basin closure also suggests a fore-arc setting. Post deformation mafic dykes cross-cut the dominant foliation of the Ad Dawadimi Terrane, suggesting a period of extension after basin closure.

Introduction

The formation of the Arabian-Nubian Shield (ANS) in the Late Neoproterozoic was a result of accretion between oceanic and intermediate crustal rocks associated with the closure of the Mozambique Ocean (Stern 1994; Johnson & Woldehaimanot 2003). The majority of the terranes that make up the ANS are a combination of juvenile oceanic crustal (MORB), fore-arc and back-arc basin sediments, and island arc volcanics (Figure 1) (Frisch & Al-Shanti 1977; Johnson & Stewart 1995; Blasband *et al.* 2000; Johnson & Woldehaimanot 2003; Allen 2007).

ANS terrane formation began shortly after the breakup of Rodinia ~800 Ma during the opening of the Mozambique Ocean (Li *et al.* 2008). The east-west closure of the Mozambique Ocean resulted in the ANS proto-terranes being accreted together (Abdelsalam & Stern 1996; Hargrove *et al.* 2006). Older terranes such as the Halfa and Haya dominate the west of the ANS, while younger terranes such as the Ad Dawadimi and Ar Rayn lie in the east (Figure 2b) (Johnson & Woldehaimanot 2003). Sutures between terranes are dominantly ophiolite decorated, however other subtle shear zones also mark terrane boundaries (Agar 1992). Ages of suturing are between 780-600 Ma when final amalgamation of the ANS is interpreted to have occurred (Johnson & Woldehaimanot 2003; Allen 2007).

Post amalgamation tectonics in the form of the Najd Fault Zone (NFZ) developed through the collision of the eastern ANS and a "rigid indenter" to the east (Duncan *et al.* 1990) from 630-530 Ma (Agar 1987). The Indian subcontinent collided with the eastern margin of West Gondwana ~600-550 Ma, with some authors suggesting faults south in Madagascar are the southern equivalents of the Najd Faults (Stern 1994) and may be interpreted as the "rigid indenter" suggested by Duncan *et al.* (1990). Other authors (Husseini 1988) claim it was the Idsas collision (the Ar Rayn Terrane's collision and suture to the Ad Dawadimi Terrane) that resulted in the formation of the NFZ between 640-600 Ma. The model for the NFZ formation is thought to be very similar to the Himalayan model, where the faults act as escape structures in a transpressional environment (Stern 1994).

Final formation of Gondwana was not until ~530 Ma, with the collision of the Australo-Mawson continent to the eastern margin of the Indian subcontinent (Collins & Pisarevsky 2005). Exact timing for the amalgamation of Arabia is still very much debated. Recent unpublished detrital zircon SHRIMP U-Pb data suggest that Abt protoliths may be as young as ~570-560 Ma. Many authors have interpreted the amalgamation of Arabia to have been completed by ~640 Ma (Allen 2007), ~620 Ma (Stern & Abdelsam 1998) and alluded to ~600 Ma (Johnson & Woldehaimanot 2003). Adding to the controversy is recent work by Collins *et al.* (2009) suggesting that the final suture of the Mozambique Ocean lies within the central Arabian Shield and facilitated amalgamation of India and Africa in Gondwana between 600 and 530 Ma.

To limit the amount of ambiguity that is often associated with numerous authors referring to the same geological terrane by an even greater number of names, it is important to bring to the reader's attention to what is referred to in this thesis as the Ad Dawadimi Terrane (Figure 1), and to point out that it has other names in further literature. Previous authors do not refer to the Ad Dawadimi Terrane as its own unique terrane (Agar 1987, 1992; Al-Saleh *et al.* 1998; Al-Saleh & Boyle 2001a, b), but instead refer to the area between the Halaban ophiolite and the Ar Rayn Terrane as the Al Amar Suture (Figure 3). Furthermore the basin that is in-filled is referred to as both the Ad Dawadimi Basin and the Abt Basin. In this thesis the region between the Halaban-Zharghat Fault and the Al Amar Fault is referred to as the Ad Dawadimi Terrane and the basin in which the Abt Schist protoliths were deposited in is the Abt Basin.

The aim of this thesis is to understand the tectonic evolution of the eastern most, and youngest, part of the ANS, by studying the structure, geochronology (both U-Pb detrital zircon and $^{40}Ar/^{39}Ar$ muscovite grains), and geochemical evolution of both the Abt Schist (the dominantly homogeneous rock type of the Ad Dawadimi Terrane) and a number of post deformational dykes that cross cut the Abt Schist fabric. The following pages will present new U-Pb Laser Ablation Inductively Coupled Plasma Mass Spectrometry (LA-ICPMS) detrital zircon analyses with the aim of constraining the age of the Abt protoliths and examining their provenance. $^{40}Ar/^{39}Ar$ muscovite single grain incremental heating data will be interpreted to directly date metamorphism related to the final closure of the Abt Basin. The structure of the Ad Dawadimi Terrane will also be addressed by presenting the results of two transects that were conducted in January 2009 that produce a cross-section through the Ad Dawadimi Terrane. Abt sediment geochemical analyses will illustrate depositional environments with Sm-Nd Thermal Ionisation Mass Spectrometry (TIMS) displaying the εNd model ages for the Abt sediment protoliths.

Geological Setting

The Ad Dawadimi Terrane is a 600x200 km crustal unit exposed on the eastern margin of the Arabian Shield (Figure 2c). Aeromagnetic data identifies the Ad Dawadimi Terrane as a distinctive low that continues ~300km north beneath Phanerozoic cover (Stacey & Hedge 1984; Kröner 1985; Stern 1994; Johnson & Stewart 1995; Johnson *et al.* 2003; Johnson & Woldehaimanot 2003). The Ad Dawadimi Terrane is perhaps one of the most homogenous terranes in the Arabian Shield, and is dominated by the Abt Schist. A number of previous authors have suggested that the Ad Dawadimi Terrane is comprised of sandstone and siltstone deposited in a back-arc basin, most probably as turbidites, and then deformed into an accretionary prism (Johnson & Woldehaimanot 2003). Sediments have since been metamorphosed into a sericite-chlorite schist. Results from this study will show a second fore-arc model is preferred over the back-arc model.

The Ad Dawadimi Terrane is bounded by the Halaban Ophiolite Complex and Afif Composite Terrane on its western margin and the Al Amar Fault and Ar Rayn Terrane on its eastern margin (Figure 2c).

The Afif Composite Terrane is composed of at least four sub-terranes of varying ages and compositions. Most of these sub-terranes are described as volcanic and sedimentary arc related, with greenschist facies metamorphism common throughout with minor post-metamorphic volcanics also present (Johnson & Woldehaimanot 2003). Only the ~1800-1600 Ma Khida sub-terrane (Figure 3) (Hargrove *et al.* 2006) shows a different composition of granites, schists and gniesses.

The Ar Rayn Terrane (Figures 1 & 2) has also been suggested as a composite terrane (Doebrich *et al.* 2007) and is characterised by an anomalously high magnetic signature extending hundreds of kilometres below the Phanerozoic cover to the east of the Arabian shield (Stern 1994; Johnson & Stewart 1995). The Ar Rayn Terrane has been described as a bimodal volcanic-volcanosedimentary terrane with transitions between the tholeiitic and calc-alkaline series (Johnson & Woldehaimanot 2003), with two syn-orogenic and one post-orogenic plutonic bodies (Doebrich *et al.* 2007). Volcanosedimentay units are U-Pb zircon dated from >689-625 Ma and plutonic rocks with varying ages from ~689-583 Ma. Doebrich *et al.* (2007) has suggested that formation of the Ar Rayn Terrane was in a continental margin setting above an east dipping subduction zone. This thesis will show that the subducting slab was west dipping.

The Ad Dawadimi Terrane is decorated by serpentinised peridotite, gabbro and metabasalt ophiolites that in many cases have been tectonically altered into an ultramafic mélanges (Frisch & Al-Shanti 1977; Kröner 1985). The four dominant ophiolites related to the Ad Dawadimi are the Halaban, Jebal Tays, Al Amar and Ar Ridayniyah (Figure 3). Emplacement of these ophiolites was coeval with the closure of the Abt Basin as the Ar Rayn Terrane collided with the Afif Terrane (Figure 48 & 50) (Al-Saleh & Boyle 2001b).

Methods

Structure

Field Work/Data Collection

Field work consisted of five weeks collecting structural data and samples for further analysis. Two transects were carried out, one (approximately 30 kilometres) on the eastern edge of the Ad Dawadimi Terrane. The other section (approximately 10 kilometres) was on the western edge of the terrane (Figure 2c). Data collection involved recording dip and dip-directions of bedding and cleavage planes, and plunge plunge-directions of lineations. The sampling process had a strong focus on the rocks from the eastern transect as the length of the transect allowed for any variations in the rock to be sampled and analysed. Samples were collected for geochronological; geochemical and mineral identification via thin section analysis.

Geochronology

U-Pb Laser Ablation Inductively Coupled Plasma Mass Spectrometry (LA-ICPMS)

Four samples were selected to be crushed and milled for detrital zircon extraction. Three of these samples (Abt-025, Abt-042 and Abt-Z_1) were from the eastern edge of the Ad Dawadimi Terrane and the other (Abt-057) from the western edge. Sample locations are marked on Figures 9 & 13.

Samples were cut to size and crushed in a large steel jaw crusher. Crushed samples were milled in a chrome-steel alloy mill, and then sieved through 425µm and 79µm mesh. The 79µm > 425µm fraction was used for zircon extraction. This fraction was panned and run through the Franz magnetic separator for further separation. Finally the sample was passed through methylene iodine-heavy liquid separation processes. Individual zircons were collected and mounted in an epoxy-resin. Resin was allowed to harden overnight then ground with corundum paper until a half thickness of zircons was exposed. The mounts were then polished to remove surface defects.

Samples were carbon coated and groups of zircons were imaged using the Philips XL20 SEM with Gatan monochromatic CL detector at Adelaide Microscopy, University of Adelaide.

Age dating was carried out using the LA-ICPMS method, where individual zircons were ablated by the New Wave UP-213 laser ablation system hooked up to an Agilent 7500cx ICP-MS. Ablation was conducted under a helium atmosphere, with a beam diameter of 30µm, 5Hz repetition rate and 75% laser intensity. Acquisition of analysis took approximately 110 seconds. The data obtained from these experiments were compared to the standard GJ-1 purchased from GEMOC at Macquarie University that was $^{206}Pb/^{238}U$, $^{207}Pb/^{235}U$, $^{207}Pb/^{206}Pb$ and $^{208}Pb/^{232}Th$ with values 0.09761, 0.8093, 0.060138, and 0.03074 respectively. An internal standard was also run (BJWP from Sri Lanka) that

was $^{207}Pb/^{206}Pb$, $^{206}Pb/^{238}U$ and $^{207}Pb/^{235}U$ values of 0.063377, 0.118223 and 1.033089 respectively, as communicated to the author by B. Wade (2009) from Adelaide Microscopy. Data reduction was carried out using GLITTER version 3.0 software (Van Achterbergh *et al.* 2001).

Presentation of data is in the form of concordia plots generated using Isoplot/Ex 3.00 for Microsoft Excel (Ludwig 2003) and probability density distribution plots generated and modified from the Excel workbook by Sircombe (2004). Concordia diagrams (Figures 28, 30, 32, 33 35 & 36) and data tables (Tables 2, 3, 4 & 5) are presented with 1σ errors on individual analyses. Probability density distribution plots (Figures 29, 31, 34 & 37) are presented with varying degrees of concordancy e.g. 90-110% concordancy, 95-105% concordancy etc.

$^{40}Ar/^{39}Ar$ Muscovite Analyses

Two samples were selected from the Ad Dawadimi Terrane for $^{40}Ar/^{39}Ar$ dating. These samples were collected on a reconnaissance trip to Saudi Arabia in 2008 by Dr. Alan Collins. Samples were crushed and milled to enable the extraction of muscovite grains. Crushing involved putting the samples through a steel jaw crusher then coarsely milled.

Further separation was carried out on the Franz magnetic separator, after which individual muscovite grains were hand-picked under a binocular microscope. These selected muscovite grains were further leached in HF for one minute and thoroughly rinsed in deionised water in an ultrasonic cleaner.

These two muscovite aliquots were mounted into large wells of a 1.9 cm diameter and 0.3 cm depth aluminium disc. These large wells were bracketed by smaller wells containing Fish Canyon sanidine (FCs), which is used as a neutron fluence monitor for which an age of 28.03 ± 0.08 Ma was adopted (Renne *et al.* 1998). The disc was irradiated for 25 hours in the Hamilton McMaster University nuclear reactor (Canada).

Analysis was undertaken at the Western Australia Argon Isotope Facility, at Curtin University of Technology, Perth. Samples of the Fish Canyon Tuff were used as standards and one blank was carried out for every four experiments undertaken. Typical ^{40}Ar blanks range from 1×10^{-16} to 2×10^{-16} mol. Sample values were corrected for using this blank.

Step-heating of the samples was carried out using a 110 W Spectron Laser Systems, with a continuous Nd-YAG (IR; 1064 nm) laser rastered over the sample for a duration of 1 minute to ensure a homogenously distributed temperature. Analyses on unknowns were carried out using a 350µm spot size, on a raster spacing of 120µm, with a scan speed and depth/pass of 100µm/sec and 5µm respectively.

Data was acquired with the Argus program written by M.O. McWilliams and ran using a LabView environment. The raw data were processed using the ArArCALC software (Koppers 2002) and the ages have been calculated using the decay constants recommended by Steiger & Jäger (1977).

Criteria for the determination of plateau were as follows:

- Plateaus must include at least 70% of ^{39}Ar.
- The plateau should be distributed over a minimum of 3 consecutive steps agreeing at 95% confidence level and satisfying a probability of fit (P) of at least 0.05.
- Plateau ages are given at the 2σ level and are calculated using the mean of all the plateau steps, each weighted by the inverse variance of their individual analytical error.
- Mini-plateaus are defined similarly except that they include between 50% and 70% of ^{39}Ar.

Uncertainties on the ^{40}Ar*/^{39}Ar ratios of the monitors are included in the calculation of the integrated and plateau age uncertainties, but not the errors on the age of the monitor and on the decay constant (internal errors only, see discussion in Min *et al.* 2000).

Geochemistry

Major Elements

Major elements were prepared by using finely crushed and milled (>79 μm) samples. Rock powder was then heated at 110°C for two hours to remove absorbed moisture. Samples were then weighed out into alumina crucibles and ignited overnight in a furnace at 960 °C and thus yielding 'Loss on Ignition' (LOI) values. One gram of ignited sample and four grams of flux were accurately weighed. Sample-flux mixture was fused using a propane-oxygen flame at ~1150°C. Fusion took place in Pt-Au crucibles and cast into a preheated mould to produce a glass disc. These glass discs were analysed using X-Ray Fluorescence (XRF). Flux material is commercially available as type 12:22, comprising 35.3% lithium tetraborate and 64.7% lithium metaborate, as personally communicated to the author by J. Stanley (2009). The samples were analysed with a Philips PW 1480 X-Ray Fluorescence (XRF) Spectrometer, using an analysis program calibrated against several international and local Standard Reference Materials (SRMs). A dual-anode (Sc-Mo) X-Ray tube was used, operating at 40kV, 75mA. XRF data is presented in Table 8 for major elements.

Trace Elements

Trace elements were prepared by using the same fine crushed and milled samples as the major elements. Approximately 5-10g of powdered sample was mixed with an approximate 1 ml of binder solution (Poly Vinal Alcohol). The mixture was pressed into pellet form and allowed to dry in air before heated again for 1 to 2 hours at 60°C in an oven to ensure complete dryness. The samples

were analysed using a Philips PW 1480 XRF Spectrometer, using several analysis programs covering suites of from 1 to 7 trace elements, with conditions optimised for the elements being analysed. The programs were calibrated against many (30 or more in some cases) local and international SRMs. The dual-anode Sc-Mo tube (operated at sufficient voltage to excite the Mo) and a Au tube were used for the analyses. Matrix corrections are made using either the Compton Scatter peak, or mass absorption coefficients calculated from the major element data as personally communicated to the author by J. Stanley (2009). XRF data is presented in Table 9 for trace elements.

Sm-Nd Thermal Ionisation Mass Spectrometry (TIMS)

Powdered samples were heated with multiple acids of varying strengths to ensure that the entire samples were completely dissolved and homogenised. A known concentration of Sm/Nd spike was then added to these samples to elevate the suspected very low Sm/Nd ratios and thus make the Sm and Nd detectable for analyses. Spike was accounted for in processing of data. Analysed samples included two mafic dykes and six were metasedimentary rocks of the Abt Schist. The internal TAS BAS sample was run as a standard to ensure preparation quality. Sedimentary units were processed by using steel-jacket bombs during the heating stage to ensure all Nd that may have been present within individual zircon grains was released Analysis for neodymium isotopes was carried out on the Finnigan MAT 262 (thermal ionisation) mass spectrometer (TIMS); samarium analysis was carried out on the Finnigan MAT 261 (thermal ionisation) mass spectrometer. Both of these machines were located at the University of Adelaide.

Results

Field observations show that the dominant structure of the Ad Dawadimi Terrane has a westward verging series of folds whose axial planes steepen-up closer to the contact with the Ar Rayn Terrane (Figure 14). All stereonet data was produced using GEOrient (Holcome 2009).

The Ad Dawadimi Terrane is largely homogenous and does not have widely varying lithologies. Mineralogically the Abt Schist is composed of biotite, muscovite and chlorite with variable amounts of quartz and feldspars. Individual beds show variable grain sizes from sand to clay, and varying thicknesses from 5-30 cm. It is the muscovite and biotite minerals that distinguish the dominant foliation of the Ad Dawadimi (Figure 56). Metamorphic grade increases to the west of the Ad Dawadimi Terrane, where andalusite growth is common, and overprints the muscovite-biotite dominant foliation. The east of the Ad Dawadimi Terrane is largely of lower grade than the western margin, however, the degree of deformation and metamorphism increases eastward closer to the Al Amar Fault.

Structure

Maps and Structural Representations

Eastern Transect of the Ad Dawadimi Terrane – (Sha'ib Khanuqah)

The eastern margin of the Ad Dawadimi Terrane was examined along the walls of the Sha'ib Khanuqah – a large east-west wadi. This part of the Ad Dawadimi Terrane is dominated by north-south striking beds that are generally westerly dipping. These bedding planes become increasingly obscured towards the east as multiple stages of cleavage development heavily overprint these features. The result of this is that bedding planes were progressively more difficult to clearly identify towards the east of the transect and were no longer the dominant foliation feature. There is a steepening up of bedding plane dips closer to the contact with the Ar Rayn Terrane (Figure 53). The degrees of dip at the western edge of the eastern transect have very shallow values of ~10 degrees, while dip angle increases to over 80 degrees in the eastern edges of the terrane near the Ar Rayn-Ad Dawadimi contact or Al Amar Fault (Figures 14 & 15).

There were three stages of cleavage development that were identified, often crenulating the bedding plane and preceding cleavages (Figure 51). These three cleavages, like the bedding planes, strike roughly north-south. With each new cleavage development the preceding cleavage was deformed and rotated. This is best seen in the data that is represented in stereonet form in Figures 17, 18 & 19 and the transect cross-section (Figure 14). In the stereonets, poles to the new cleavage (S_3) (Figure 19) are concentrated in a smaller area than poles to the preceding cleavages (S_2, S_1) (Figure 18, S_1

cleavage is not presented). Multiple cleavage development indicates that there are three stages of deformation preserved in the Ad Dawadimi Terrane.
Intersection lineations between bedding and all three of the cleavages are plunging shallowly to the south (Figures 20, 21 & 22). Mineral lineations, usually in the form of elongated quartz aggregates, mimic the shallow southerly plunge (Figure 23) of the intersection lineations; however there is a secondary mineral lineation developed that plunges towards the south-west (~225°).

A combination of these data suggest that the eastern transect shows west-south-west verging sub-horizontal, moderately inclined, open, asymmetrical folds with sub-horizontal, gentle south-south-east plunges (Figure 53). Extension occurred parallel to the fold hinges in a SSE-NNW direction.

Western Transect of the Ad Dawadimi Terrane.
Unlike the eastern transect, the west completely lacks clear bedding planes. Cleavage planes also show a much more erratic arrangement. Two cleavages were identified in the west, where the second cleavage (S_2) (Figure 25) is overprinting and crenulating the preceding cleavage (S_1) (Figure 24). Similarly to the eastern transect the S_2 cleavage is concentrated in a smaller area than the S_1 cleavage. Although very erratic in places, strike of cleavages is 240-60 degrees (Figures 10, 11, 24 & 25).

Folds are west-north-west verging, sub-horizontal, moderately – gently inclined, open, asymmetrical geometry; with a north-east south-west extensional component. Plunge of folds are 1-199 (Figures 24 & 25). This is supported by quartz mineral stretching lineations with a principle direction of 6-215 (Figure 27) and intersection lineations between the two cleavages, 5-017 (Figure 26).

Rock types are of higher metamorphic grade than in the eastern transect as expressed by the growth of andalusite (Figure 54) with biotite (Figure 55), muscovite and chlorite in abundance, growth of tourmaline was also common.

Geochronology

U-Pb Laser Ablation Inductively Coupled Plasma Mass Spectrometry (LA-ICPMS)

Cathode luminescence (CL) response of rims and cores vary considerably between individual zircon grains in all of the samples, this is likely due to the variety of source rocks from which these zircons were originally derived. Zircon cores and rims are identified in CL images and labelled as ‘c’ and ‘r’ in Tables 2, 3, 4 & 5. A ‘u’ determination indicates that no core-rim determination could be made and these grains show highly convoluted patterns under CL.

Eastern Transect of the Ad Dawadimi Terrane – (Sha'ib Khanuqah)

Sample Abt-025 ~ (N: 23°56'17.3", E: 44°50'09.3")

Zircon grains from this sample are subhedral to euhedral. They dominantly have clear oscillatory zoning in CL, suggesting being derived from an igneous source rock. Structureless overgrowth rims are present in some of the zircons. However, this appears to be very limited in extent and is not always easily distinguishable. Zircons that displayed convolute internal CL patterns were avoided (Figure 57).

From a total of seventy zircon grains, fifty-four of these were analysed and are presented (Table 2). The sixteen analyses that were rejected were done so because processing errors resulting in concordancy values being very high (> 110% conc.) or very low (< 5% conc.) and could not be corrected for. Targeted areas include both rims and cores with a concentration on the latter. Age data are plotted on a conventional concordia with accompanying probability density distribution diagrams in Figures 28 & 29. Many analyses were discordant, which may be due to Pb loss or common Pb in the zircon. Analyses that are 90-110% concordant range in $^{206}Pb/^{238}U$ age from 783 ± 11 Ma to 606 ± 8 Ma (1σ error).

Two major $^{206}Pb/^{238}U$ age peaks can be identified at 615-610 Ma and 650-645 Ma. It is possible that a third peak exists at 680-675 Ma, however, this may only represent one or two zircons that would otherwise be masked by the larger 650-645 Ma peak.

Sample Abt-042 ~ (N: 23°58'28.5", E: 44°54'54.1")

Zircons in this sample, while still retaining the dominant subhedral to euhedral form, appear to have had a dramatic increase in the degree of internal alteration compared to the previous sample as very few grains preserve rims and cores identifiable in CL (Figure 58). Without the clear rims and cores of these zircons many have been assigned as indistinguishable ('u') previously mentioned (Table 3). Limited overgrowth of rims is present in a number of zircons from this sample.

Sixty zircons were analysed targeting rims and cores. However, due to the high number of zircons that have heavy internal alteration most of the spot target areas are labelled as indistinguishable. Age data is plotted on a conventional concordia with accompanying probability density distribution diagrams in Figures 30 & 31. Data appear largely concordant with some of the discordant data being below the concordia. Maximum and minimum $^{206}Pb/^{238}U$ ages are 686 ± 10 Ma and 608 ± 9 Ma (1σ error) respectively for data with a >90% concordancy. There is only one major $^{206}Pb/^{238}U$ peak that can be identified from this sample. This occurs at 655-650 Ma. The weighted mean is given at ~652 ± 4 Ma (1σ error) with 2 of 60 spots rejected giving an MSWD of 2.5. Admittedly this is a rather high MSWD value; however this can be explained by the younger zircons as in Figure 31 that skew

the probability density plot. There is therefore one population of zircons within this sample with a small number of younger individual zircons that give an elevated MSWD.

Sample Abt-Z_1 ~ (N: 23°56'14.5", E: 44°50'15.2")

The zircons from this sample appear similar to those from sample Abt-025. Grains are subhedral to euhedral, with oscillatory zoning, and limited rim overgrowth development (Figure 59). As with previous samples there are a number of zircons present that preserve convolute CL patterns and appear to have undergone some alteration.

Seventy zircons were analysed. Analysis spots were targeted on centres and uncertain zones of zircons only. Data is displayed as both conventional concordia and probability density distributions (Figure 32, 33 & 34). Data is largely concordant with some of the discordant data being below the concordia. Maximum and minimum ages are 1396 ± 17 Ma and 572 ± 8 Ma (1σ error) respectively for data with a >90% concordancy. This minimum age is one of three that can be seen in the raw data set in Table 4 to be anomalously young compared to the >90% concordant data from the other samples from this transect. These three ages are as follows; 572 ± 8 Ma, 581 ± 10 Ma, and 594 ± 7 Ma (1σ error). Of these samples only the 594 ± 7 Ma (1σ error) zircon grain has a >95% concordancy. These will be compared to other $^{206}Pb/^{238}U$ ages from other authors as well as $^{40}Ar/^{39}Ar$ data and discussed later.

There are two major peaks that can be identified at 630-625 Ma and 680-675 Ma. Minor peaks can also be identified; however, these are representative of only one or two individual zircons. An example of this can be seen in Figure 34 where the small peak at ~1400 Ma is the prior mentioned oldest zircon of 1396 ± 17 Ma.

Western Transect of the Ad Dawadimi Terrane

Sample Abt-057 ~ (N: 24°12'21.3", E: 44°09'29.4")

Zircon grains are subhedral to euhedral, with clear oscillatory zoning (Figure 60). Overgrowth rims appear to be absent in most cases, zircons that do have this overgrowth have rims that are too small to be analysed accurately. Zircons display oscillatory zoning in most cases thus are interpreted as representing zircon growth in a magma (Corfu *et al.* 2003). Rocks from this transect are of higher grade showing signs of andalusite growth in hand and thin section specimens.

One hundred individual zircon grains were analysed concentrating on cores, with four rims and nine uncertainties, these are shown is Table 5. Data are mostly discordant below the concordia. Minimum and maximum ages are 2543 ± 28 Ma and 616 ± 9 Ma (1σ error) respectively for data with a >90% concordancy (Figures 35 & 36).

Two major peaks can be identified at 650 Ma and 715-720 Ma (Figure 37). A minor peak identifies a zircon age of 800 Ma. Small peaks are also represented with ages > 1 Ga; however as with previous samples these peaks only represent one or two individual zircons.

$^{40}Ar/^{39}Ar$ Muscovite Analyses

$^{40}Ar/^{39}Ar$ dating techniques allow for information on the time at which a rock cooled below the effective closure temperature of Ar in muscovite (~350°C) (Haines *et al.* 2004) or if the rock had never been above this temperature, the technique can date muscovite growth, and therefore directly date metamorphism. In this study there were two samples analysed using the metamorphic mineral muscovite. For sample descriptions see Table 1. Due to the lengthy preparation time for this technique of geochronological dating, analyses were conducted on samples that were collected by Dr. Alan Collins on the 2008 reconnaissance trip and prepared in early 2009 by Grant Cox.

Sample S08-15 ~ (N: 23°54'51.8", E: 44°43'32.3")

Tabulated results from the analysis on this sample can be viewed in Table 6. Incremental raster heating of S08-15 yields a weighted plateau age of 613 ± 5.9 Ma (2σ error), with an admittedly high MSWD of 1.6 and probability of 0.11 (Figure 38). Normal isochron data give an age of 615.51 ± 6.42 Ma and better MSWD value of 0.12 (Table 6).

Sample S08-17 ~ (N: 23°56'58.3", E: 44°32'16.0")

Tabulated results from the analysis on this sample can be viewed in Table 7. Incremental raster heating of S08-17 yields a weighted plateau age of 616 ± 2.8 Ma (2σ error), with an MSWD of 0.63 and probability of 0.76 (Figure 39) and thus giving much more statistically convincing data than S08-15. Normal isochron data for this sample yield complementary statistically significant values with ages of 617.52 ± 5.25 Ma with a MSWD of 0.11 (Table 7).

Geochemistry

Metasedimentary Rocks

During metamorphism, with either the addition or depletion of mobile elements, chemically immobile elements will maintain their invariant rations (Fralick & Kronberg 1997). Elements that are chemically immobile and have undergone similar depositional dynamics are able to be used to determine the source terrane from sedimentary geochemistry. Major and trace geochemical analysis of metasedimentary rocks for the Abt Schist (meta-sandstones and meta-siltstones) were undertaken in an attempt to identify the tectonic setting of deposition and the nature of potential source rocks for these sediments. Sample descriptions can be viewed in Table 1.

Figure 40 is a broad classification of the analysed metasedimentary rocks that are located in the Ad Dawadimi Terrane. This total alkalis vs. silica plot is based on Le Maitre *et al.* (1989). This identifies the Abt Schist rocks as iron-rich shales. It must be noted that there is the potential for potassium and silica mobilisation during metamorphism of the basin, which would reduce the usefulness of this plot and not give an accurate representation of the sediments deposited prior to metamorphism. However, compared to field and laboratory observations, the clustering of the data in the classification figure is sufficiently accurate and metamorphism is thought not to have contributed to extensive elemental mobilisation.

Figure 41 displays TiO_2 vs. Ni (after Floyd 1987) and Th/Sc vs. Cr (after McLennan 1990) for metasedimentary rocks from the Ad Dawadimi Terrane. The reasoning for using these elements is due to their low mobility during greenschist facies metamorphism (Mielke 1979). Cr will also often be enriched in clays (~90 mg kg^{-1}), with concentrations usually being lower in sandstones (~35 mg kg^{-1}) (Mielke 1979). The low Th/Sc values may represent not very evolved source rock (Totten *et al.* 2000). The TiO_2 vs. Ni part of this figure shows that source materials for these sediments are largely acidic in nature. The Th/Sc vs. Cr plot places all of the sediments in a fore-arc setting; however there is overlap between other fields. The conclusion that the fore-arc setting is the more probable setting is based on the Th/Sc vs. Cr plot (Figure 41), where all of the samples plot within this field, and correspond with low Th/Sc fore-arc setting values in work conducted by McLennan (1990).

The final sedimentary plot (Figure 42) is a Th/Sc vs. Zr/Sc plot which shows the amount of reworking through the upper crust that has been experienced by these sediments after McLennan *et al.* (1993) and modified from Lopez de Luchi *et al.* (2003). Lopez de Luchi *et al.* (2003) suggest that hydraulic sorting and reworking of sediments can influence their chemical compositions. Over time this can lead to a concentration in Th, Sc and Zr. These elements are immobile during greenschist metamorphism and therefore are not readily transported out of the system. Generally Th/Sc indicates the degree of igneous differentiation (McLennan *et al.* 1990; McLennan *et al.* 1993). Th/Sc values that are below 0.8 are considered to reflect input of mafic sources. If Th/Sc values <0.8 are coupled with high Zr/Sc values then this is thought to reflect mature or recycled sources (Lopez de Luchi *et al.* 2003). High Zr values indicate extensive reworking. In the case of the Abt sedimentary rocks, protolith material have intermediate provenance. Figure 42 shows that sediments have not experienced a lot of reworking and are most probably deposited in an Ocean Island Arc (OIA) or Continental Island Arc (CIA) setting. This plot will also be discussed further in relation to TIMS analyses and model ages of source rocks for the Abt Schist sediments.

Igneous Rocks

Numerous dykes that cross cut the foliation of the Ad Dawadimi Terrane were chemically analysed to infer the terrane's evolution after basin closure.

Field observations suggest that the majority of the dykes are of mafic composition, with only samples Abt-062, Abt-026 and Abt 008 displaying a more felsic appearance. By using a Zr/Ti vs. Nb/Y diagram (Figure 43) modified from Winchester & Floyd (1977), the types of igneous dykes were determined. This form of diagram was chosen because elements used are immobile and not readily lost during low grade geological processes. Winchester & Floyd (1977) state that both Zr/Ti and Nb/Y ratios are both indices of alkalinity, but only Zr/Ti is a differentiation index. If these ratios are plotted against each other they are able to discriminate between different volcanic rock types. As can be seen in this figure dykes are dominantly andesitic and basaltic, with a few being more felsic in nature.

Conventional AFM diagrams suggest that the majority of the dykes are tholeiitic in nature, with only three samples, Abt-062, Abt-026 and Abt-008 plotting as calc-alkaline (Figure 44).

By plotting major XRF data on a Zr/Y vs. Zr diagram after Pearce & Norry (1979) a tectonic environment could be suggested. This plot (Figure 45) suggests that these dykes are mostly within-plate basalts. Samples Abt-008, Abt-026 and Abt-062 were excluded as these are not considered to be mafic dykes based on elevated SiO_2 (Table 8).

The final diagram is a Zr-Ti-Y ternary discrimination diagram for basalts (Figure 46) after Pearce & Cann (1973). This is a complementary diagram to the Zr/Y vs. Zr diagram previously mentioned, again felsic samples Abt-008, Abt-026 and Abt-062 were excluded. Ti values appear to be highly variant as a number of the dykes that plotted in the WPB field of the Zr/Y vs Zr diagram do not plot in the same field for the Zr-Ti-Y diagram. Both the Zr-Ti-Y ternary discrimination diagram for basalts and the Zr/Y vs. Zr diagram are presented because elements are immobile and not likely to have been lost from the system during any alteration that may have occurred.

Sm-Nd Thermal Ionisation Mass Spectormetry (TIMS)

Sm/Nd analysis on a number of samples of the Abt Schist was carried out to determine their model ages. This, in turn, gives an average model age of the source rocks to the protolith from which the Abt Schist is derived (Figures 47). Model ages are older than detrital zircon ages, which suggest that older components occur in the source rocks and may have been incorporated into the sediments of

the Abt Basin during deposition. Rock descriptions can be found in Table 1. εNd values and T_{DM} model ages in this section were obtained by using the file:
(TIMS Spreadsheet)Sm-Nd_spike_F_Reduction_Template_Adel_(Goldstein_update)_8.1
supplied to the author by D. Bruce, University of Adelaide.

Sample Abt-016 ~ (N: 23°55'27.2", E: 44°47'35.5")
Analysis of this sample yielded an εNd value of -2.13 ± 0.31, with a T_{DM} model age of 1112 ± 26 Ma (2σ error). The model age suggests sediments from this sample have not experienced major recycling.

Sample Abt-033 ~ (N: 23°57'32.8", E: 44°52'47.4")
Analysis of this sample yielded an εNd value of -3.29 ± 0.22, with T_{DM} model age of 1281 ± 18 Ma (2σ error). The model age suggests sediments from this sample have not experienced major recycling.

Sample Abt-038 ~ (N: 23°57'47.0", E: 44°53'51.7")
Analysis of this sample yielded an εNd value of -2.40 ± 0.17, with a T_{DM} model age of 1138 ± 15Ma (2σ errors). The model age suggests sediments from this sample have not experienced major recycling.

Sample Abt-039 (N: 23°57'47.0", E: 44°53'51.7")
Although sampled from the same location as Abt-038, there were significant differences between the two samples to consider them as two independent sedimentary units. Analysis of this sample yielded an εNd value of -2.28 ± 0.25, with a T_{DM} model age of 1168 ± 22 Ma (2σ errors). The model age suggests sediments from this sample have not experienced major recycling.

Sample Abt-042 (N: 23°58'28.5", E: 44°54'54.1")
Analysis of this sample yielded an εNd value of -4.32 ± 0.20, with a T_{DM} model age of 1132 ± 15Ma (2σ errors). Sediments have not experienced major recycling. This sample has the lowest εNd value. The T_{DM} model age is approximately the same as the other samples except sample Abt-033, which has a much older T_{DM} model age.

Sample Abt-Nd_1 (N: 23°57’47.0”, E: 44°53’51.7”)

Also located in the same place as Abt-038 and Abt-039, this sample showed enough variation from the other two samples to be analysed. Analysis of this sample yielded an εNd value of -2.09 ± 0.18, with a T_{DM} model age of 1097 ± 15 Ma (2σ errors). Sediments have not experienced major recycling.

Discussion

Age of Metasedimentary Protoliths

Al-Saleh *et al.* (1998) carried out $^{40}Ar/^{39}Ar$ analyses on the Halaban ophiolite (Figure 3) suggesting two stages of orogenesis for the region with maximum orogenic dates at 680 Ma and 600 Ma. Thus Al-Saleh *et al.* (1998) suggests that deposition of Abt protolith was complete by 680 Ma. Johnson & Woldehaimanot (2003) support this by stating that the life of the Abt Basin was relatively short (~15 Ma) and closure occurred at ~680 Ma. This scenario that the Abt Basin was closed between ~680-620 Ma has been suggested by numerous other authors (Al-Saleh & Boyle 2001b, a; Hargrove *et al.* 2006; Stoeser & Frost 2006; Doebrich *et al.* 2007). Results from this study suggest that closure was not completed at least for another seven million years (~613 Ma) and sediments were still being deposited up until this time.

$^{40}Ar/^{39}Ar$ dating from this study has yielded muscovite closure plateau ages of 613 ± 5.9 Ma (2σ errors) and 616 ± 2.8 Ma (2σ errors). As the muscovite is of metamorphic origin and the rock is unlikely to have reached temperatures above ~350°C (the closure temperature for Ar in muscovite), these ages are interpreted to date muscovite growth during greenschist facies metamorphism.

The $^{40}Ar/^{39}Ar$ dates from Al-Saleh *et al.* (1998) do not support new $^{206}Pb/^{238}U$ zircon LA-ICMPS dates from this study. Al-Saleh *et al.* (1998) data suggests that all sedimentary material in the Abt Basin must be younger than ~680 Ma, however, the data from this study shows zircon ages are far younger than ~680 Ma, thus not supporting the work by Al-Saleh *et al.* (1998).

Sample Z_1 yielded three $^{206}Pb/^{238}U$ detrital zircon ages that were lower than the other samples analysed. The youngest zircons give ages of 572 ± 16 Ma, 581 ± 20 Ma, and 594 ± 14 Ma (2σ error) at ≥90-110% concordancy. If the concordancy is refined to ≥95-105% only the 594 ± 14 Ma (2σ error) zircon is considered concordant. The 594 ± 14 Ma (2σ error) age is within the error of the 613 ± 5.9 Ma (2σ error) $^{40}Ar/^{39}Ar$ metamorphic age. However this is based on a single detrital zircon. This ~594 Ma zircon age is not within error of the more precise $^{40}Ar/^{39}Ar$ metamorphic age of 616 ± 2.8 Ma (2σ error). The next youngest detrital zircon in this sample (at ≥95-105% concordancy) is 612 ± 22 Ma (2σ error) and fits well within error of both the $^{40}Ar/^{39}Ar$ metamorphic ages.

Maximum depositional ages from the samples give ages at 606 ± 16 Ma, 608 ± 18 Ma, 594 ± 14 Ma (612 ± 22 Ma) and 644 ± 16 Ma (2σ errors) at ≥95-105% concordancy. All of these maximum depositional ages are within error of both the 616 ± 2.8 Ma and 613 ± 5.9 Ma (2σ errors) $^{40}Ar/^{39}Ar$ metamorphic muscovite ages, except the single 594 ± 14 Ma (2σ error) aged grain. If the absolute maximum and minimum depositional ages are considered, not including the young single zircon 594

± 14 Ma (2σ error), we are able to determine that deposition continued up to a ~616 Ma maximum and metamorphism occurred as late as ~613 Ma.

A concurrent study conducted by Cox (2009) on the Jebel Tays ophiolite complex has revealed Abt Schist detrital zircon ages are younger on average than zircons obtained in this presented study. Cox (2009) gives the youngest zircon age as 596 ± 14 Ma (2σ error), at 97% concordancy, again this date is only obtained from a single detrital zircon. The Abt Schist surrounding the Jebel Tays ophiolite complex has not experienced greenschist metamorphism but rather zeolite metamorphism. There have been suggestions that there may be two slightly differing Abt Schists within the Ad Dawadimi Terrane, one with greenschist metamorphic characteristics and the other only zeolite characteristics, however, these claims require further research into the relationship between the northern and southern regions of the Ad Dawadimi Terrane.

Finally new results from this study suggest that deposition of Abt Schist sediments was on going as late as ~616-613 Ma when basin closure occurred, and not ~680 as previous research has suggested.

Provenance of Metasedimentary Rocks & Tectonic Environment of the Abt Schist

Provenance of Metasedimentary Rocks

The ages of the detrital zircons can be used to determine the provenance of the Abt Basin sediments. The majority of zircons dated in this study have ages of 715-720 Ma, 680-675Ma, 655-645 Ma, 630-625 Ma and ~615 Ma, which can be explained by material shedding off the adjacent Afif Terrane or intrusive granites within the Afif Terrane. A number of samples had zircons that were of Mesoproterozoic, or older, ages. These dates are 2543 ± 28 Ma and 1396 ± 17 Ma. This suggests that there is a Mesoproterozoic or older source rock for the sediments of the Abt Basin. The closest source rock for the 1396 ± 17 Ma aged zircon is the Khida Subterrane, one of the Afif subterranes, which is dated ~1.86-1.66 Ga (Johnson & Woldehaimanot 2003) (Figures 1 & 2b). The source of the 2543 ± 28 Ma zircon is enigmatic. The Halfa Terrane on the far western edge of the ANS has protolith ages of ~2.6-1.2 Ga (Johnson & Woldehaimanot 2003), however it is not know how sediments from the Halfa Terrane were transported to the Abt Basin as they are on opposite sides of the ANS (Figure 1). Another explanation is material is derived from the southern extension of the Afif Terrane in Yemen – the Neoarchaean Al Mafid Block (Collins & Windley 2002; Collins & Pisarevsky 2005). A final possibility is these anomalously old zircons may have also been sourced from a terrane that remains elusive and has not yet been identified.

The εNd model ages suggest that the protoliths of the Abt Schist are derived from source rocks that mixed together to produce late Mesoproterozoic T_{DM} model ages. Figure 47 shows that the T_{DM}

model ages of the samples are from 1168 ± 22Ma to 1097 ± 15 Ma (2σ errors), with one sample being much older at 1281 ± 26 Ma. Sample Abt-033's older T_{DM} model age may be explained by this sample being finely grained and probably a clay rich unit prior to metamorphism. Clay commonly has significantly higher abundances of Nd than sands, usually from 13% to >300% (McLennan *et al.* 1989). The clay unit from this study yields low εNd values, and so must be at the lower end of this range. Higher εNd values can be explained by coarser grained samples being enriched in REE and thus Nd was liberated from zircon and monazite (McLennan *et al.* 1989) minerals during the sample preparation processes. These model ages fit to published U-Pb ages of the Afif Terrane (Johnson & Woldehaimanot 2003) and thus support U-Pb detrital zircon data from this study, suggesting sediments in the Abt Basin were derived from the Afif Terrane.

Both the εNd model ages (Figure 47) and the Th/Sc vs. Zr/Sc diagram (Figure 42) show that the sediments of the Ad Dawadimi Terrane are have not experienced extensive reworking. The Th/Sc vs. Zr/Sc diagram is also unique and can give both an indication of provenance and potential depositional environments for the Abt Schist sediments. Sediments that show Th/Sc values that are lower than 1 ppm are considered to be from a mixed mafic-felsic source, values above 1 ppm are considered to be of felsic origins (Taylor & McLennan 1985; McLennan *et al.* 1990; McLennan *et al.* 1993; LaMaskin *et al.* 2008). In the case of this study the Abt Basin sediments are showing mixed mafic-felsic source signatures. The Afif Terrane is composed of both mafic and felsic rocks (Johnson & Woldehaimanot 2003), and contributed to the material deposited into the Abt Basin.

Tectonic Environment

The Th/Sc vs. Zr/Sc diagram (Figure 42) suggests that the Abt protoliths were deposited into a basin that had both Ocean Island Arc (OIA) and Continental Island Arc (CIA) characteristics. The OIA setting implies that there is oceanic crust being subducted beneath oceanic crust. This may hold true prior to Abt protolith deposition, however, provenance work from this study suggest that the Afif Terrane was the source for the material that was deposited into the Abt Basin. Therefore sediments were being deposited into the Abt Basin when an east dipping slab was subducting beneath the Afif Terrane and so the CIA depositional setting is preferred over the OIA. Figure 41shows that more of the samples fall within the fore-arc field, and better accommodates the provenance of the Abt protolith.

This study shows, with some confidence, that the tectonic environment for the Abt Bain was a fore-arc basin. Figure 41, a Th/Sc vs. Cr diagram, shows that sedimentary samples were all deposited into a fore-arc basin. There is overlap between the fore-arc and back-arc tectonic setting fields. The fore-arc setting is preferred because all analysed samples plot within this field and only vary in

concentrations of Cr. Increased Cr levels are an indicator of mafic to ultramafic sources of sediments (Danchin 1967), and so the variable levels of Cr may be explained by variations between more mafic and more felsic sources within the Afif Terrane (Agar 1992; Johnson & Woldehaimanot 2003), from where sediments of the Abt Schist were derived. Th/Sc ratios are characteristically low supporting the fore-arc setting as suggested by McLennan *et al.* (1990).

Structural Evolution of the Ad Dawadimi Terrane

To date there has been little to no work on the structure of the Ad Dawadimi Terrane. The research conducted in this study will be discussed and presented as new material that has in no way been exhausted.

Closure of the Abt Basin was a result of east-west closure between the eastern Ar Rayn and western Afif Terranes. Basin closure was accompanied by multiple stages of cleavage development with each subsequent cleavage overprinting the bedding plane preceding cleavage. Stereonet data shows this by each successive cleavage occupying a smaller area than the cleavage that formed before (Figures 18, 19, 20, 24 & 25). This is seen in both the east and the west of the Ad Dawadimi Terrane.

Eastern Transect of the Ad Dawadimi Terrane – (Sha'ib Khanuqah)

The broad spread of poles to bedding planes shows the highly folded nature of the Ad Dawadimi Terrane (Figure 17). The bedding plane does not dip to the south and very little dip towards the north, thus suggesting that all of the shortening was from the east to west. The S_2 cleavage has a large spread which is also has dip confined to the east and west. S_3 cleavage similarly does not dip to the north or south, but has a reduced area of spread (Figure 19) suggesting it to be the last cleavage to develop in this area.

The dominant foliation expressed in the Ad Dawadimi Terrane steepens toward the east where it gets closer to the Al Amar Fault (Figure 14). This is interpreted to be a result of the thrusting of the Ar Rayn Terrane over the Abt Basin.

Western Transect of the Ad Dawadimi Terrane

Distinctive bedding planes on the western margin of the Ad Dawadimi Terrane are heavily overprinted by two cleavages that have developed as a result of basin closure. The schistose foliation is also overprinted by andalusite growth.

Poles to the S_1 cleavage are concentrated in a broad area mostly dipping westward.

Compared to the eastern margin of the Ad Dawadimi Terrane, the west has much more open folds that are of lower westerly dipping angle (Figures 14 & 16). Similarly to the eastern Ad Dawadimi

Terrane, the latter cleavage (S_2) that had developed has a reduced spread and is confined to a roughly east-west dipping orientation with little to no dip towards the north and south.

Generally folds in the Ad Dawadimi Terrane are a series of antiforms and synforms that verge towards the west. Both the east and west of the Ad Dawadimi Terrane folds vary from having regular to irregular hinge lines. There is variability to the direction of plunge for folds between each margin of the Ad Dawadimi; the eastern margin's folds plunge roughly SSE, while the western margin's folds plunge approximately SSW. Stretching mineral lineations of quartz in both the east and west of the Ad Dawadimi Terrane indicate the presence of a north-south extensional component, parallel to the hinge of the folds. This feature is related to the east-west shortening to accommodate the stress built up during basin closure.

Tectonic Evolution of the Ad Dawadimi Terrane

Previous authors have been reluctant to assign a definitive depositional environment to the Ad Dawadimi Terrane. There have been two models proposed for the evolution of the Ad Dawadimi Terrane. The first of these models is the back-arc setting as proposed by Al-Saleh and Boyle (2001b). This model suggests that the Afif and Ar Rayn Terranes were once joined and then rifted with later back-arc extension, forming the Abt Back-Arc Basin. Work by Johnson & Stewart (1995) and Doebrich *et al.* (2007) show that the Ar Rayn is characterised by a positive magnetic anomaly that extends to the north and south beneath the Phanerozoic cover, a feature not identified with the Afif Terrane, thus disputing the back-arc model. To date there is little convincing evidence to suggest a back-arc tectonic setting for the Ad Dawadimi Terrane.

The second model is a fore-arc setting (Figures 49 & 50), where the Abt Basin, on the eastern margin of the Afif Terrane, receives sediments directly from the Afif Terrane. The results from this study show that this second fore-arc model is the preferred basin evolution model for the Ad Dawadimi Terrane.

There is some debate on the orientation of the subducting slab associated with basin closure. Authors such as Al-Saleh & Boyle (2001a, b) and Quick (1991) suggest a westerly dipping subduction slab, while other authors such as Al-Shanti & Mitchell (1976) and Stacey & Hedge (1984) suggest an easterly dipping subducting slab. Johnson & Stewart (1995) admit that this is problematic as the accretionary structures associated with the direction of subduction that differentiate between these two ideas cannot be identified within the Abt Schist. This study concludes that sediments derived from the Afif are being deposited into a fore-arc setting, and thus the dip of subducting slab must be towards the west. The combination of: 1) detrital zircon and

geochemical provenance shows the protolith of the Abt Schist was derived from the Afif Terrane; 2) geochemical analysis suggest a fore-arc tectonic setting; 3) short timing between sedimentary deposition and basin closure; and 4) the east-west deformation within the Ad Dawadimi Terrane all support this.

The fore-arc model suggests that the Ar Rayn was never a part of the Afif Terrane and it was in fact a volcanic-arc that formed in the Mozambique Ocean to the east of the Afif Terrane, as the subduction zone beneath the Afif Terrane migrated out board to the eastern margin of the Ar Rayn after the first stages of Abt Basin closure (Figures 49 & 50 ~670-615 Ma). The emplacement of the Halaban and Jebel Tays Ophiolites is best illustrated by Stern (2004), where the oceanic crust on the eastern edge of the Afif Terrane is uplifted and deformed. During this deformation the Abt sediments that were deposited into the fore-arc basin are also uplifted and deformed (Figure 48). This theory is supported by recent work from Doebrich *et al.* (2007) who suggest that the Ar Rayn represents a continental margin arc above a westward dipping subduction zone along a continental block represented by the Afif Terrane.

Prior to ~615 Ma, sediments were shed off the Afif Terrane (1860-667 Ma) and deposited into the Abt Basin - a fore-arc along the Afif Terrane's eastern margin. At 615 Ma, the Abt Basin was closed through the east-west shortening between the Afif and Ar Rayn Terranes. New structural mapping from this study has revealed that there are three stages of deformation related to this east-west shortening. These stages of deformation led to the growth of metamorphic minerals such as biotite, muscovite and chlorite, which dominate the mineralogy of the Ad Dawadimi Terrane. Greenschist facies metamorphism has been experienced throughout the Ad Dawadimi Terrane, but evidence for slightly higher metamorphism exists in the west of the terrane. These higher grade rocks are easily identified by andalusite growth which appears to overprint the schistose texture of the Ad Dawadimi Terrane.

The Ad Dawadimi Terrane is generally characterised by north-south striking, westward verging, and slightly inclined, asymmetrical folds. Folds are broad and open in the west of the terrane (Figure 16) tightening and steeping in the east of the terrane (Figure 14). North-south extensional components in the folds are parallel to the fold hinges and lineations suggesting that folds plunge towards the south.

Multiple interrupted stages of extension after basin inversion resulted in dyke intrusions into the Ad Dawadimi Terrane. The evidence for this is provided by geochemical analysis suggesting dykes are with-in plate basalts (WPBs) (Figure 45) dominantly composed of tholeiitic and minor calc-alkaline characteristics (Figure 44). From this study extension of the eastern ANS can be no earlier than the

peak metamorphism (Johnson & Woldehaimanot 2003) in this study ~615 Ma, when the Ar Rayn Terrane was amalgamated to the Afif-Ad Dawadimi Terrane. Extensional tectonics was the reason for the formation of many of the pull-apart and half-graben basins that formed after the final amalgamation of the ANS (Johnson & Woldehaimanot 2003), one such half-graben basin is the Antaq Basin between the Afif and Ad Dawadimi Terranes (Johnson 2003; Nettle 2009).

In summary, new work presented in this thesis shows that the timing between sediment deposition of Abt sediments was in a fore-arc basin on the eastern margin of the Afif Terrane. Provenance studies from detrital zircons and geochemical analyses support this view suggesting that sediments from the Abt Basin were derived from the Mesoproterozoic, or older, Afif Terrane. East-west closure of the Abt Basin resulted in deformation of the sediments into westward verging asymmetrical folds of greenschist facies metamorphic grade. Multiple stages of cleavage development over printed the preceding cleavages. Late stage extension throughout the eastern ANS resulted in emplacement of mafic dykes.

Conclusion

Although there are two potential models for the formation of the Ad Dawadimi Terrane, this study yields results that are preferential to the Model 2. The evolution of the Ad Dawadimi Terrane can be summarised as the following:

- Felsic-mafic sediments derived from the Afif Terrane are deposited into the Abt Fore-Arc Basin on the eastern margin of the Afif until ~615 Ma.
- The Abt Schist protoliths contain pre-Neoproterozoic detrital zircons and T_{DM} ages consistent with them being sourced from the Afif Terrane.
- Complete closure of the Abt Basin resulted in deformation of the sediments into N-S trending folds with two distinct cleavages being formed by progressive E-W shortening. Oceanic crust beneath Abt sediments was uplifted and emplaced in ophiolite complexes on the margins of and within the Ad Dawadimi Terrane.
- Final basin closure is dated at ~615 Ma by $^{40}Ar/^{39}Ar$ muscovite analysis.
- Post closure out-board slab roll-back resulted in extension of the Ad Dawadimi Terrane and subsequent tholeiitic and calc-alkaline dyke emplacement. These dykes were one of the final features in the Ad Dawadimi Terrane, cross cutting the dominant foliation.

Acknowledgements

The author would like to thank Mobarak Al-Nahdi, Mulfi Al-Rshidi and Fayek Kattan from the Saudi Geological Survey for the financial, logistical, and technical support that was provided while in the field. Special thanks to Alan Collins, Galen Halverson and John Foden for their supervision and guidance on this project. Thanks to David Bruce for his expertise with the clean laboratory and TIMS, John Stanley for his demonstrations on correct laboratory procedures as well as running the XRF on both trace and major elements. Special thanks to Grant Cox for his demonstrations on sample preparation, and guidance on LA-ICPMS, ICPMS, plus other techniques; but especially for his patience with my constant questions. Benjamin Wade and Fred Jourdan for their laboratory support with using LA-ICPMS and $^{40}Ar/^{39}Ar$ dating techniques. I would like to thank my family for the financial and emotional support provided and my partner for being so understanding and supportive this past year. Finally thanks to my research colleagues Grant Cox and David Nettle for the many discussions and support on this study and their individual projects.

References

ABDELSALAM M. G. & STERN R. J. 1996. Sutures and shear zones in the Arabian-Nubian Shield. *Journal of African Earth Sciences* **23**, 289-310.

AGAR R. A. 1987. The najd fault system revisited; a two-way strike-slip orogen in the saudi arabian shield. *Journal of Structural Geology* **9**, 41-48.

AGAR R. A. 1992. The tectono-metallogenic evolution of the arabian shield. *Precambrian Research* **58**, 169-194.

AL-SALEH A. M. & BOYLE A. P. 2001a. Neoproterozoic ensialic back-arc spreading in the eastern Arabian shield: geochemical evidence from the Halaban Ophiolite. *Journal of African Earth Sciences* **33**, 1-15.

AL-SALEH A. M. & BOYLE A. P. 2001b. Structural rejuvenation of the eastern Arabian Shield during continental collision: 40Ar/39Ar evidence from the Ar Ridayniyah ophiolitic mélange. *Journal of African Earth Sciences* **33**, 135-141.

AL-SALEH A. M., BOYLE A. P. & MUSSETT A. E. 1998. Metamorphism and $^{40}Ar/^{39}Ar$ dating of the Halaban Ophiolite and associated units: evidence for two-stage orogenesis in the eastern Arabian Shield. *Journal of the Geological Society, London* **155**, 165-175.

AL-SHANTI A. M. S. & MITCHELL A. H. G. 1976. Late Precambrian subduction and collision in the Al Amar--Idsas region, Arabian Shield, Kingdom of Saudi Arabia. *Tectonophysics* **30**, T41-T47.

ALLEN P. A. 2007. The Huqf Supergroup of Oman: Basin development and context for Neoproterozoic glaciation. *Earth-Science Reviews* **84**, 139-185.

BLASBAND B., WHITE S., BROOIJMANS P., BOORDER H. D. & VISSER W. 2000. Late Proterozoic extensional collapse in the Arabian-Nubian Shield. *Journal of the Geological Society, London* **157**, 615-628.

COLLINS A. S., HALVERSON G. P., FODEN J., COX G., LEWIS C., NETTLE D. & KATTAN F. 2009. The Palaeogeography of the North Gondwanan Ediacaran-Cambrian Petroleum Province. Paper presented at Rodinia: Supercontinents, Superplumes and Scotland, Edinburgh, Scotland(unpubl.).

COLLINS A. S. & PISAREVSKY S. A. 2005. Amalgamating eastern Gondwana: The evolution of the Circum-Indian Orogens. *Earth-Science Reviews* **71**, 229-270.

COLLINS A. S. & WINDLEY B. F. 2002. The tectonic evolution of central and northern Madagascar and its place in the final assembly of Gondwana. *Journal of Geology* **110**, 325-340.

CORFU F., HANCHAR J. M., HOSKIN P. W. O. & KINNY P. 2003. Atlas of Zirocn Textures. *In:* Hanchar J. M. & Hoskin P. W. O. eds. *Reviews in Mineralogy & Geochemistry*, pp. 468-500. Zircon **53** Mineralogical Society of America, Washington, DC.

COX G. M. 2009. Jebel Tays ophiolitic melange, Saudi Arabia: Tectonic setting, petrogenesis and geochronological framework. University of Adelaide, Adelaide (unpubl.).

DANCHIN R. V. 1967. Chromium and Nickel in the Fig Tree Shale from South Africa. *Science* **158**, 261-262.

DOEBRICH J. L., AL-JEHANI A. M., SIDDIQUI A. A., HAYES T. S., WOODEN J. L. & JOHNSON P. R. 2007. Geology and metallogeny of the Ar Rayn terrane, eastern Arabian shield: Evolution of a Neoproterozoic continental-margin arc during assembly of Gondwana within the East African orogen. *Precambrian Research* **158**, 17-50.

DUNCAN I. J., RIVARD B., ARVIDSON R. E. & SULTAN M. 1990. Structural interpretation and tectonic evolution of a part of the Najd Shear Zone (Saudi Arabia) using Landsat thematic-mapper data. *Tectonophysics* **178**, 309-315, 319-333, 335.

FRALICK P. W. & KRONBERG B. I. 1997. Geochemical discrimination of clastic sedimentary rock sources. *Sedimentary Geology* **113**, 111-124.

FRISCH W. & AL-SHANTI A. 1977. Ophiolite belts and the collision of island arcs in the Arabian Shield. *Tectonophysics* **43**, 293-306.

HAINES P. W., TURNER S. P., KELLEY S. P., WARTHO J.-A. & SHERLOCK S. C. 2004. 40Ar-39Ar dating of detrital muscovite in provenance investigations: a case study from the Adelaide Rift Complex, South Australia. *Earth and Planetary Science Letters* **227**, 297-311.

HARGROVE U. S., STERN R. J., KIMURA J. I., MANTON W. I. & JOHNSON P. R. 2006. How juvenile is the Arabian-Nubian Shield? Evidence from Nd isotopes and pre-Neoproterozoic inherited zircon in the Bi'r Umq suture zone, Saudi Arabia. *Earth and Planetary Science Letters* **252**, 308-326.

HOLCOME R. 2009. GEOrient 9.4.3. *Brisbane*.

HUSSEINI M. I. 1988. The Arabian Infracambrian extensional system. *Tectonophysics* **148**, 93-103.

JOHNSON P. R. 2003. Post-amalgamation basins of the NE Arabian shield and implications for Neoproterozoic III tectonism in the northern East African orogen. *Precambrian Research* **123**, 321-337.

JOHNSON P. R., ABDELSALAM M. G. & STERN R. J. 2003. The Bi'r Umq-Nakasib Suture Zone in the Arabian-Nubian Shield: A Key to Understanding Crustal Growth in the East African Orogen. *Gondwana Research* **6**, 523-530.

JOHNSON P. R. & STEWART I. C. F. 1995. Magnetically inferred basement structure in central Saudi Arabia. *Tectonophysics* **245**, 37-52.

JOHNSON P. R. & WOLDEHAIMANOT B. 2003. Development of the Arabian-Nubian Shield: perspectives on accretion and deformation in the northern East African Orogen and the assembly of Gondwana. *Proterozoic East Gondwana: Supercontinent Assembly and Breakup* **206**, 289-325.

KOPPERS A. P. 2002. ArArCALC--software for 40Ar/39Ar age calculations. *Computers & Geosciences* **28**, 605-619.

KRÖNER A. 1985. Ophiolites and the evolution of tectonic boundaries in the late proterozoic Arabian--Nubian shield of northeast Africa and Arabia. *Precambrian Research* **27**, 277-300.

LAMASKIN T. A., DORSEY R. J. & VERVOORT J. D. 2008. Tectonic controls on mudrock geochemistry, Mesozoic rocks of eastern Oregon and western Idaho, U.S.A.: Implications for Cordilleran Tectonics. *Journal of Sedimentary Research* **78**, 765-783.

LE MAITRE R.W. B. P., DUDEK A., KELLER J., LAMEYRE LE BAS M.J., SABINE P.A., SCHMID R., SORENSEN H., STRECKEISEN A., WOOLLEY A.R., ZANETTIN B. 1989. A classification of igneous rocks and glossary terms. *Blackwell, Oxford*.

LI Z. X., BOGDANOVA S. V., COLLINS A. S., DAVIDSON A., DE WAELE B., ERNST R. E., FITZSIMONS I. C. W., FUCK R. A., GLADKOCHUB D. P., JACOBS J., KARLSTROM K. E., LU S., NATAPOV L. M., PEASE V., PISAREVSKY S. A., THRANE K. & VERNIKOVSKY V. 2008. Assembly, configuration, and break-up history of Rodinia: A synthesis. *Precambrian Research* **160**, 179-210.

LOPEZ DE LUCHI M. G., CEREDO M. E., SIEGESMUND S., STEENKEN A. & WEMMER K. 2003. Provenance and tectonic setting of the protoliths of the Metamorphic Complexes of Sierra de San Luis. *Rev. Asoc. Geol. Argent* **58**, 524-540.

LUDWIG K. R. 2003. User's manual of Isoplot 3.00. A geochronological Toolkit for Microsoft Excel. Berkeley Geochronology Center, Special Publication No. 4a, Berkeley, California.

MCLENNAN S. M., HEMMING S., MCDANIEL D. K. & HANSON G N. 1993. Geochemical approaches to sedimentation, provenance and tectonics. In: Johnson, M.J. and Basu, A. (Eds.): Processes controlling the composition of clastic sediments. *Geological Society of America, Special Paper* **285**, 21-40.

MCLENNAN S. M., MCCULLOCH M. T., TAYLOR S. R. & MAYNARD J. B. 1989. Effects of sedimentary sorting on neodymium isotopes in deep-sea turbidites. *Nature* **337**, 547-549.

MCLENNAN S. M., TAYLOR S. R., MCCULLOCH M. T. & MAYNARD J. B. 1990. Geochemical and Nd-Sr isotopic composition of deep-sea turbidites: crustal evolution and plate tectonic associations. *Geochemica et Comochimica Acta* **54**, 2015-2050.

MIELKE J. E. 1979. Composition of the Earth's crust and distribution of the elements. *In:* Siegel F. R. ed. *Review of Research on Modern Problems in Geochemistry*, pp. 13-36. UNESCO, Paris.

MIN K., MUNDIL R., RENNE P. R. & LUDWIG K. R. 2000. A test for systematic errors in 40Ar/39Ar geochronology through comparison with U-Pb analysis of a 1.1 Ga rhyolite. *Geochemica et Comochimica Acta* **64**, 73-98.

NETTLE D. 2009. A sequence stratigraphic, geochronological and chemostratigraphic investigation of the Ediacaran Antaq Basin, Eastern Arabian Shield, Saudi Arabia. University of Adelaide, Adelaide (unpubl.).

PEARCE J. A. & CANN J. R. 1973. Tectonic setting of basic volcanic rocks determined using trace element analyses. *Earth and Planetary Science Letters* **19**, 290-300.

PEARCE J. A., NORRY, M.J. 1979. Petrogenetic implications of Ti, Zr, Y and Nb variations in volcanic rocks. *Contributions to Mineralogy and Petrology* **69**, 33-47.

QUICK J. E. 1991. Late Proterozoic transpression on the Nabitah fault system--implications for the assembly of the Arabian Shield. *Precambrian Research* **53**, 119-147.

RENNE P. R., SWISHER C. C., DEINO A. L., KARNER D. B., OWENS T. L. & DEPAOLO D. J. 1998. Intercalibration of standards, absolute ages and uncertainties in 40Ar/39Ar dating. *Chemical Geology* **145**, 117-152.

SIRCOMBE K. N. 2004. AgeDisplay: an EXCEL workbook to evaluate and display univariate geochronological data using binned frequency histograms and probability density distributions. *Computers and Geosciences* **30**, 21-31.

STACEY J. S. & HEDGE C. E. 1984. Geological and isotopic evidence for early Proterozoic crust in the eastern Arabian Shield. *Geology* **12**, 310-313.

STEIGER R. H. & JÄGER E. 1977. Subcommission on geochronology: Convention on the use of decay constants in geo- and cosmochronology. *Earth and Planetary Science Letters* **36**, 359-362.

STERN R. J. 1994. ARC ASSEMBLY AND CONTINENTAL COLLISION IN THE NEOPROTEROZOIC EAST-AFRICAN OROGEN - IMPLICATIONS FOR THE CONSOLIDATION OF GONDWANALAND. *Annual Review of Earth and Planetary Sciences* **22**, 319-351.

STERN R. J. 2004. Subduction initiation: spontaneous and induced. *Earth and Planetary Science Letters* **226**, 275-292.

STERN R. J. & ABDELSAM M. G. 1998. Formation of juvenile continental crust in the Arabian-Nubian shield: evidence form granitic rocks of the Nakasib suture, NE Sudan. *Geologische Rundschau* **87**, 150-160.

STOESER D. B. & FROST C. D. 2006. Nd, Pb, Sr, and O isotopic characterization of Saudi Arabian Shield terranes. *Chemical Geology* **226**, 163-188.

TAYLOR S. R. & MCLENNAN S. M. 1985. The Continental Crust: Its Composition and Evolution: Oxford, U.K. *Blackwell*, 312.

TOTTEN M. W., HANAN M. A. & WEAVER B. L. 2000. Beyond whole-rock geochemistry of shales: The importance of assessing mineralogic controls for revealing tectonic discriminants of multiple sediment sources for the Ouachita Mountain flysch deposits. *Geological Society of America, Bulletin* **112**, 1012-1022.

VAN ACHTERBERGH E., RYAN C. G., JACKSON S. E. & GRIFFIN W. L. eds. 2001. *Data reduction software for LA-ICP-MS.* . In: Laser-ablation-ICPMS in the earth sciences; principles and applications. (edited by Paul, J.S.). Mineralogical Association of Canada, Ottowa, ON, Canada.

WINCHESTER J. A. & FLOYD P. A. 1977. Geochemical discrimination of different magma series and their differentiation products using immobile elements. *Chemical Geology* **20**, 325-343.

Figure Captions

Figure 1: The Arabian Nubian Shield (ANS). a) The ANS; also with shield related rocks from Yemen and Oman. See following Figure for b) and c) inserts.

Figure 2: Inserts from Figure 1. b) Terranes of the Arabian-Nubian shield (ANS) with estimated protolith ages, after Johnson and Woldehaimanot (2003). Khida Sub-Terrane is the southernmost area in the Afif Composite Terrane with ages 1.86-1.66 Ga. c) The Ad Dawadimi Terrane; blue coloured markers show the transects that were conducted.

Figure 3: Terranes, basins, ophiolites and igneous intrusives of the Ad Dawadimi Terrane modified after Cox (2009).

Figure 4: Eastern Transect; (S0) Bedding Planes.

Figure 5: Eastern Transect; (S1) Cleavage Planes and (S2) Cleavage Planes.

Figure 6: Eastern Transect; (S3) Cleavage Planes.

Figure 7: Eastern Transect; (S0/S1, S0/S2, S0/S3) Intersection Lineations.

Figure 8: Eastern Transect; Grooved and Mineral Stretching Lineations.

Figure 9: Sample Locations and Cross-Section.

Figure 10: Western Transect; (S0) Bedding Planes and (S1) Cleavage Planes.

Figure 11: Western Transect; (S2) Cleavage Planes and (S0/S1) Intersection Lineations.

Figure 12: Western Transect; Grooved and Mineral Stretching Lineations.

Figure 13: Western Transect; Sample Locations and Cross Section.

Figure 14: Cross section of Wadi Sha'ib Khanuqah. Small scale folds are represented by orange line with the larger scale regional folds in black.

Figure 15: Cross section of Wadi Sha'ib Khanuqah. Displays progressive folding of cleavage planes.

Figure 16: Cross section of Western Transect. Small scale folds are represented by orange line with the larger scale regional folds in black.

Figure 17: (S0) Bedding Plane

Figure 18: (S2) Cleavage Plane

Figure 19: (S3) Cleavage Plane

Figure 20: (S0/S2) Intersection Lineation

Figure 21: (S0/S3) Intersection Lineation

Figure 22: (S2/S3) Intersection Lineation

Figure 23: Mineral Stretching Lineation

Figure 24: (S1) Cleavage Plane

Figure 25: (S2) Cleavage Plane

Figure 26: (S1S2) Intersection Lineation

Figure 27: Mineral Stretching Lineation

Figure 28: Abt-025, concordia of data 90-110% concordancy. Insert: concordia showing data between 95-105%.

Figure 29: Abt-025, probability density distribution plot. Note that this sample had 16 analyses rejected during the data processing stage and as such only 54 of the total 70 zircons can be displayed here.

Figure 30: Abt-042, concordia of data 90-110% concordancy. Insert: concordia showing data between 95-105%.

Figure 31: Abt-042, probability density distribution plot.

Figure 32: Abt-$0Z_1$, concordia of data 90-110% concordancy.

Figure 33: Abt-$0Z_1$, concordia of data 90-110% concordancy, 400-120 Ma age range. Insert: concordia showing data between 95-105%.

Figure 34: Abt-$0Z_1$, probability density distribution plot.

Figure 35: Abt-057, concordia of data 90-110% concordancy.

Figure 36: Abt-057, concordia of data 90-110% concordancy, 400-1200 Ma age range. Insert: concordia showing data between 95-105%.

Figure 37: Abt-057, probability density distribution plot.

Figure 38: $^{40}Ar/^{39}Ar$ weighted plateau for individual incremental heated Abt Schist muscovite grain.

Figure 39: $^{40}Ar/^{39}Ar$ weighted plateau for individual incremental heated Abt Schist muscovite grain.

Figure 40: Classification of Abt Schist Sedimentary Rocks after Le Maitre *et al*., (1989). K and SiO2 mobilisation may have occurred during metamorphism.

Figure 41: **Top**) fields for acidic and basic materials after Floyd (1987). **Bottom**) boxed areas produced after McLennan (1990) for greywackes and mudstones of modern sedimentary basins, both these plots were obtained and adapted from Lopez de Luchi *et al.*,(2003). Settings are labelled accordingly in graph. Note the overlap between fields, consistency in all samples plotting in the fore-arc field suggest this to be the most likely depositional environment, however this does not completely exclude the other fields that are overlapped.

Figure 42: Th/Sc vs. Zr/Sc diagram after McLennan *et al.,* (1993) modified from Lopez de Luchi *et al.,* (2003). **1)** Ocean Island Arc **(OIA), 2)** Continental Island Arc **(CIA), 3)** Active Continental Margin **(ACM**), and **4)** Passive Margin (**PM**), after Bhatia & Crook (1986). Note the concentration of points around fields 1 and 2. Increased sediment recycling results in data concnetration around fields 3 and 4, this thereofre suggests that the sediments are both juvenile and deposited in and OIA and/or CIA.

Figure 43: Zr/Ti vs. Nb/Y diagram for volcanic rocks, dyke discrimination after Winchester and Floyd (1977). Note the dominance of samples plotting in either the trachytes andesite or alkali basalt fields. These are the mafic dykes that were probably a result of an extensional phase after foliation development of the Ad Dawadimi Terrane. The other dykes are much more felsic in nature and are thought to be related to the volcanism of the Ar Rayn Terrane that continued after the development of the Ad Dawadimi foliation. The issue arises as Abt-008 was an intrusive dyke that was cross cut by Abt -009. The above diagram suggests that Abt-008 is an extrusive andesite. A possible explanation is there is greater Zr in this sample, or the rock unit is the intrusive equivalent, a granodiorite, however field observations do not favour this theory.

Figure 44: AFM diagram adapted from Kuno (1968) and Irvine & Baragar (1971). The majority of the dykes sampled clearly plot in the tholeiitic field with Abt-008, Abt-026 and Abt-062 plotting as calc-alkaline.

Figure 45: Zr/Y vs. Zr diagram modified from Pearce and Norry (1979). Mafic dykes plot in the within plate basalts field, suggesting dyke emplacement within continental crust. Conclude that these dykes are related to post amalgamation deformation of the Ad Dawadimi Terrane, most probably due to slab roll-back of a subducting slab east of the Ar Rayn Terrane.

Figure 46: Zr-Ti-Y ternary discrimination diagram for basalts after Pearce & Cann (1973). **A**) Island-Arc Tholeiites, **B**) Mid-Ocean Ridge Basalt + Island-Arc Tholeiites and Calc-Alkaline Basalts, **C**) Calc-Alkaline Basalts, and **D**) Within Plate Basalts.

Figure 47: εNd model ages for Ad Dawadimi Terrane sediments. These ages are older than the ~650-680 Ma detrital zircons. This is probably a result of materials mixing from multiple sources prior to depositin. Interestingly sample Abt-033 has a much older model age than the other samples. Abt-033 was much more clay rich than the other samples which were dominated by silts and sands, this may explain the elevated εNd model ages obtained.

Figure 48: Cartoon of emplacement of the Halaban and Jebel Tays Ophiolite Complexs in a fore-arc basin, modified after Stern (2004). **Top;** sediment deposition into Abt Fore-Arc Basin, **bottom;** closure of basin with deformation and uplift of ophiolites and Ad Dawadimi Terrane and thrust faulting of the Ar Rayn Terrane over the Ad Dawadimi Terrane.

Figure 49: Fore-arc setting for the deposition of sediments into the Abt Basin.

Figure 50: Fore-arc setting for the deposition of the Abt Basin continued.

Figure 51: S_1 and S_2 cleavage planes. Note how the S1 cleavage is being crenulated by the later S_2 cleavage. S3 cleavage has not been well developed in this photograph. Bedding plane is approximately horizontal in this photograph. Standard size writing pencil used for scale.

Figure 52: Open, antiformal, asymmetrical folds. Fractures are preferentially forming along the bedding plane. Card is approximately 8-9 cm in scale.

Figure 53: Steeping up of bedding plane with closer proximity to the Al Amar Fault, eastern Ad Dawadimi Terrane. Photograph taken looking north. Shrubs at base of outcrop face are approximately 2.5 m high.

Figure 54: Western transect, higher grade mineral assemblages with the inclusion on andalusite. Andalusite appears as black-brown specks on the top surface of a bedding plane.

Figure 55: Western Transect, extensive biotite sheeting between bedding planes.

Figure 56: Folds highlighted by biotite and muscovite mineralisation. Hammer for scale. Photograph taken facing north.

Figure 57: Cathodoluminescence (CL) response images of zircons from Sample Abt-025. Red circle represents size and position of laser spot. Zircons not showing spots were not selected for analysis due to convolute internal structure.

Figure 58: Cathodoluminescence (CL) response images of zircons from Sample Abt-042. Red circle represents size and position of laser spot. Zircons not showing spots were not selected for analysis due to convolute internal structure. Alteration is more intense in this sample than previous Abt-025. Rims are present in a number of these zircons.

Figure 59: Cathodoluminescence (CL) response images of zircons from Sample Abt-Z_1. Red circle represents size and position of laser spot. Zircons not showing spots were not selected for analysis due to convolute internal structure.

Figure 60: Cathodoluminescence (CL) response images of zircons from Sample Abt-057. Red circle represents size and position of laser spot. Zircons not showing spots were not selected for analysis due to convolute internal structure. Oscillatory zoning are interpreted as representing zircon growth in a magma.

Figures

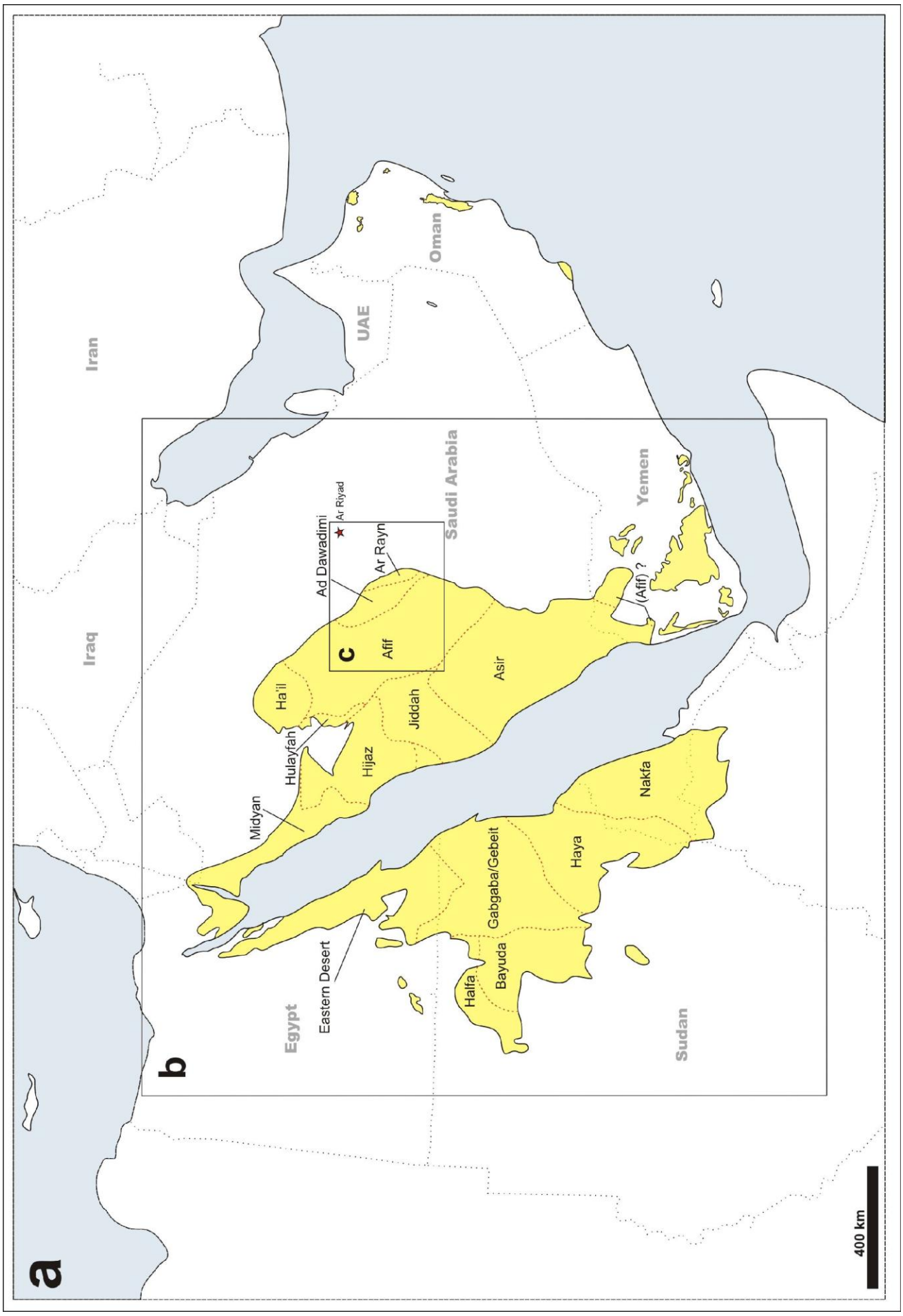

Figure 1

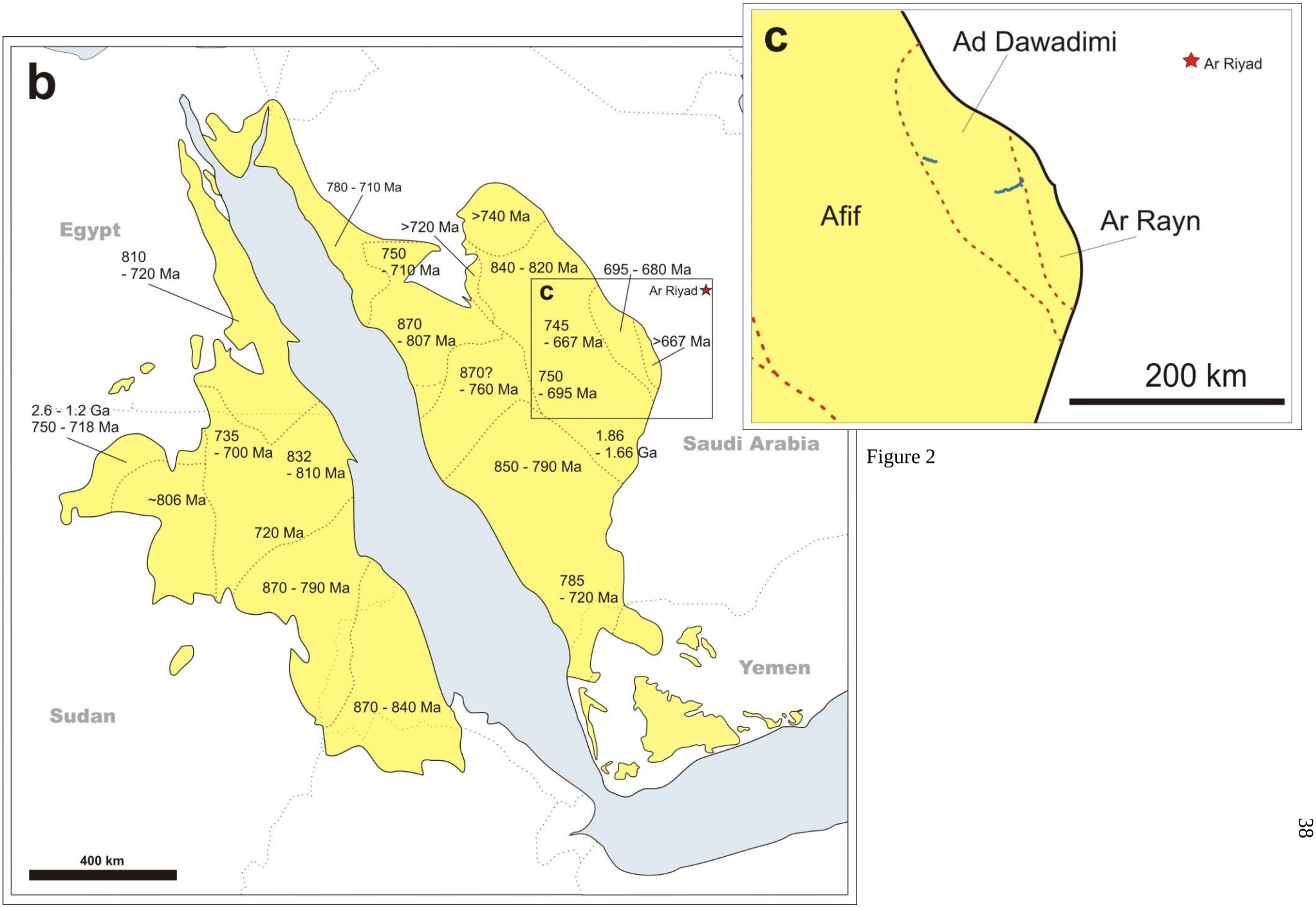
b
780 - 710 Ma
>740 Ma
>720 Ma
Egypt
810
- 720 Ma
750
- 710 Ma
840 - 820 Ma
695 - 680 Ma
c
Ar Riyad
870
- 807 Ma
745
- 667 Ma
>667 Ma
870?
- 760 Ma
750
- 695 Ma
2.6 - 1.2 Ga
750 - 718 Ma
735
- 700 Ma
832
- 810 Ma
1.86
- 1.66 Ga
Saudi Arabia
850 - 790 Ma
~806 Ma
720 Ma
870 - 790 Ma
785
- 720 Ma
Yemen
Sudan
870 - 840 Ma
400 km
c
Ad Dawadimi
Ar Riyad
Afif
Ar Rayn
200 km

Figure 2

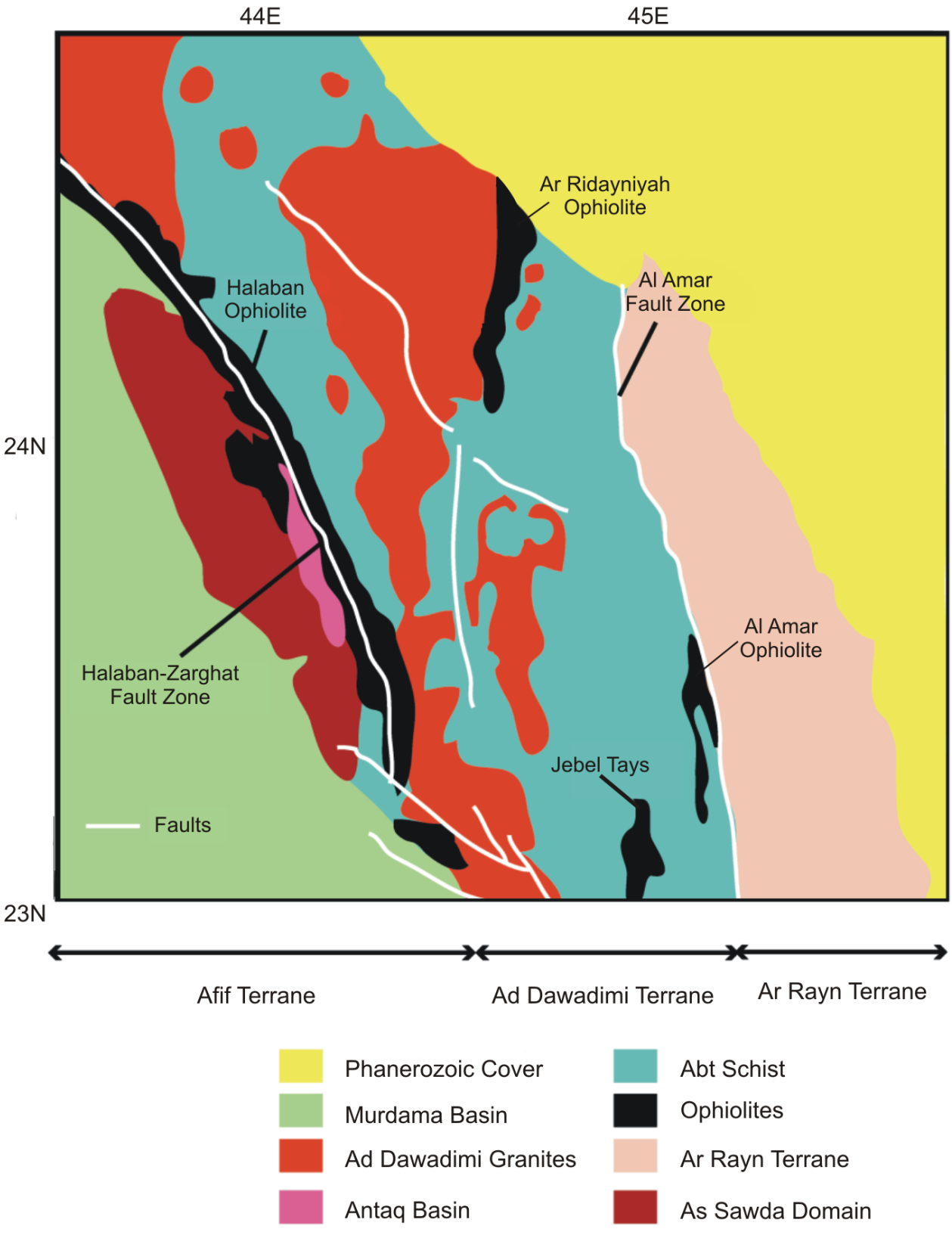
44E
45E
24N
23N
Ar Ridayniyah
Ophiolite
Halaban
Ophiolite
Al Amar
Fault Zone
Al Amar
Ophiolite
Halaban-Zarghat
Fault Zone
Jebel Tays
Faults
Afif Terrane
Ad Dawadimi Terrane
Ar Rayn Terrane
Phanerozoic Cover
Murdama Basin
Ad Dawadimi Granites
Antaq Basin
Abt Schist
Ophiolites
Ar Rayn Terrane
As Sawda Domain

Figure 3

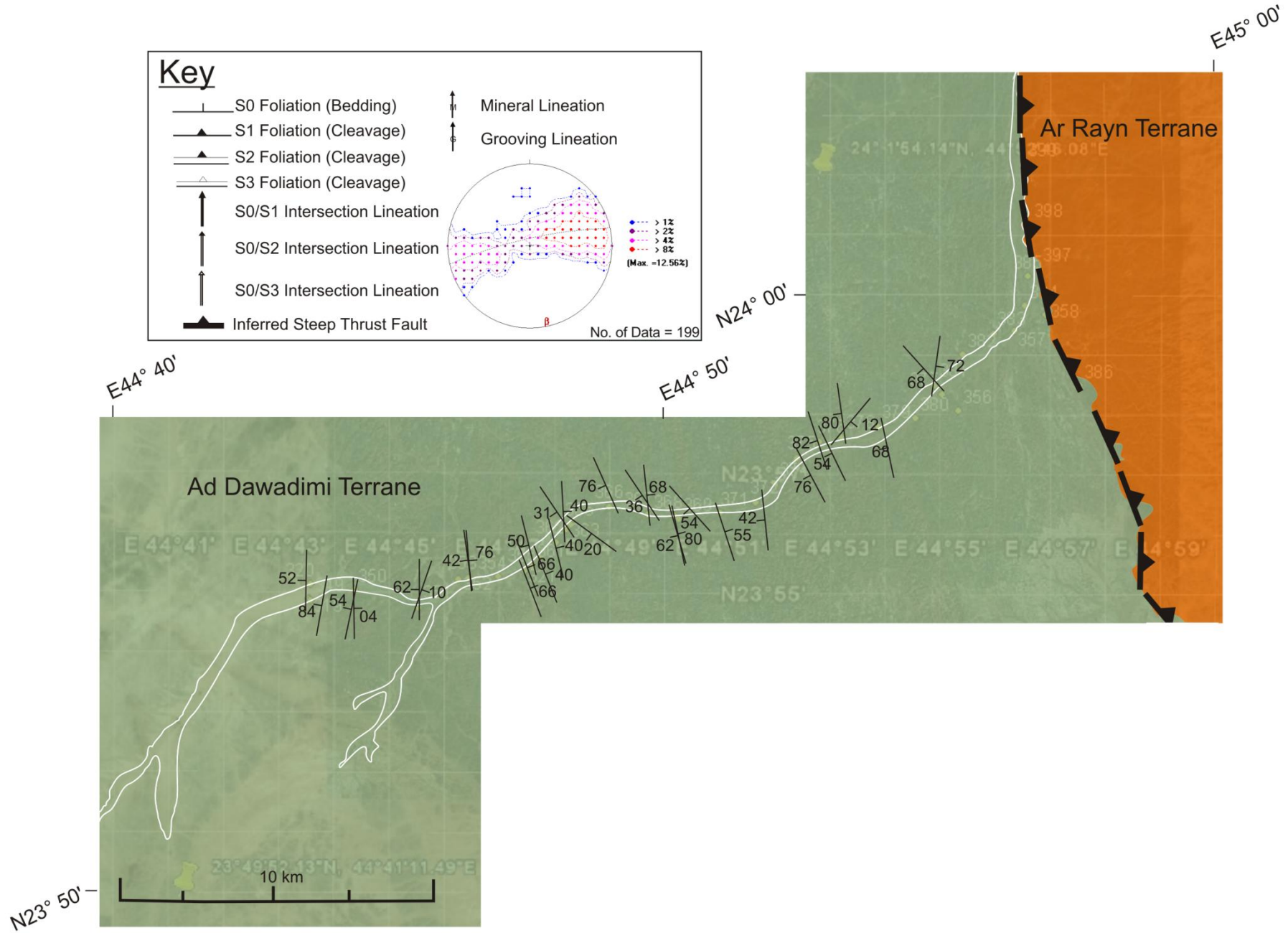
Key
S0 Foliation (Bedding)
S1 Foliation (Cleavage)
S2 Foliation (Cleavage)
S3 Foliation (Cleavage)
S0/S1 Intersection Lineation
S0/S2 Intersection Lineation
S0/S3 Intersection Lineation
Inferred Steep Thrust Fault
Mineral Lineation
Grooving Lineation
> 1%
> 2%
> 4%
> 8%
(Max. =12.56%)
No. of Data = 199
E45° 00'
N24° 00'
E44° 40'
E44° 50'
N23° 50'
Ar Rayn Terrane
Ad Dawadimi Terrane
10 km

Figure 4

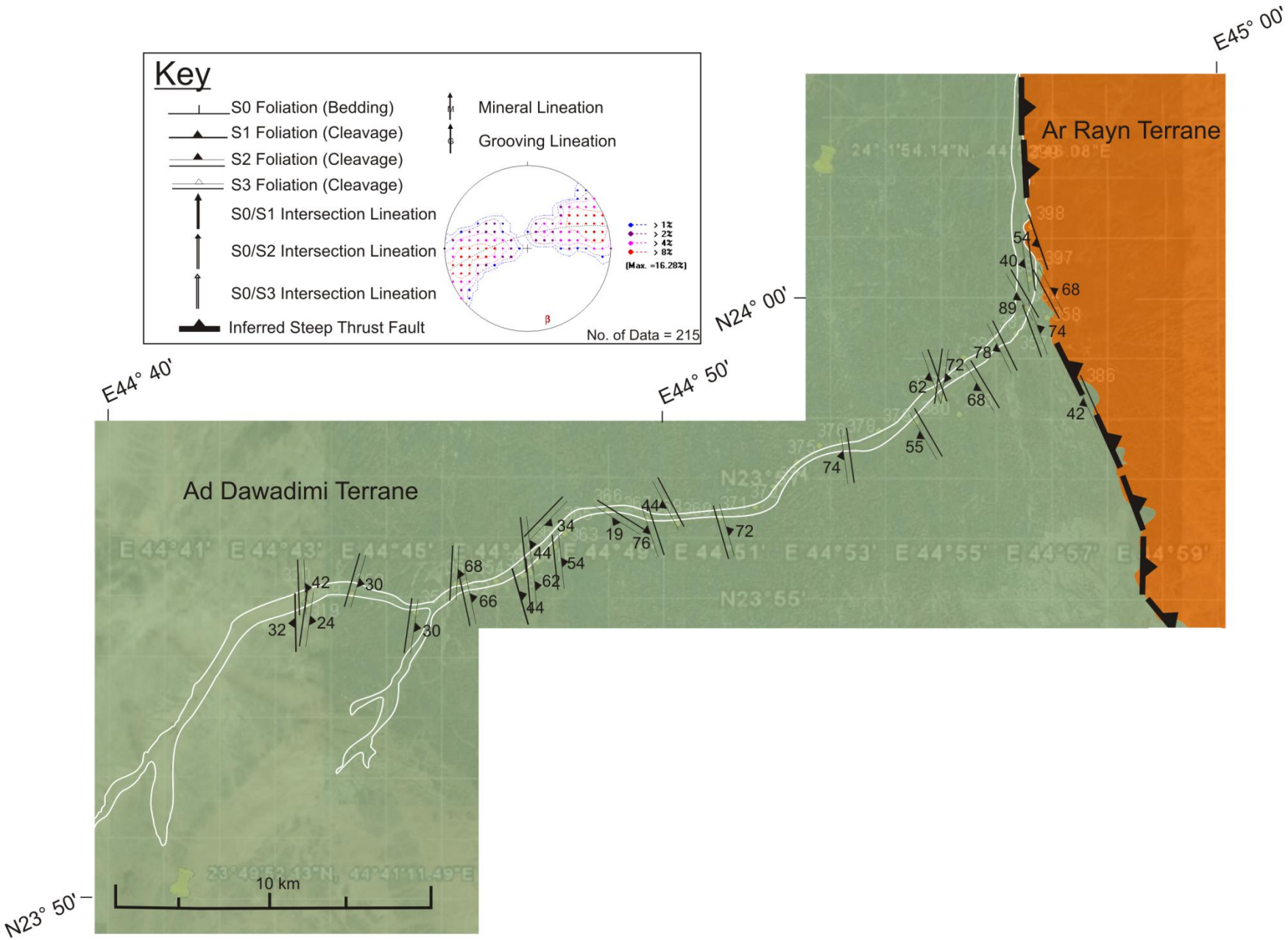
Key
S0 Foliation (Bedding)
S1 Foliation (Cleavage)
S2 Foliation (Cleavage)
S3 Foliation (Cleavage)
S0/S1 Intersection Lineation
S0/S2 Intersection Lineation
S0/S3 Intersection Lineation
Inferred Steep Thrust Fault
Mineral Lineation
Grooving Lineation
> 1%
> 2%
> 4%
> 8%
(Max. =16.28%)
No. of Data = 215
Ar Rayn Terrane
Ad Dawadimi Terrane
E45° 00'
N24° 00'
E44° 40'
E44° 50'
N23° 50'
10 km

Figure 5

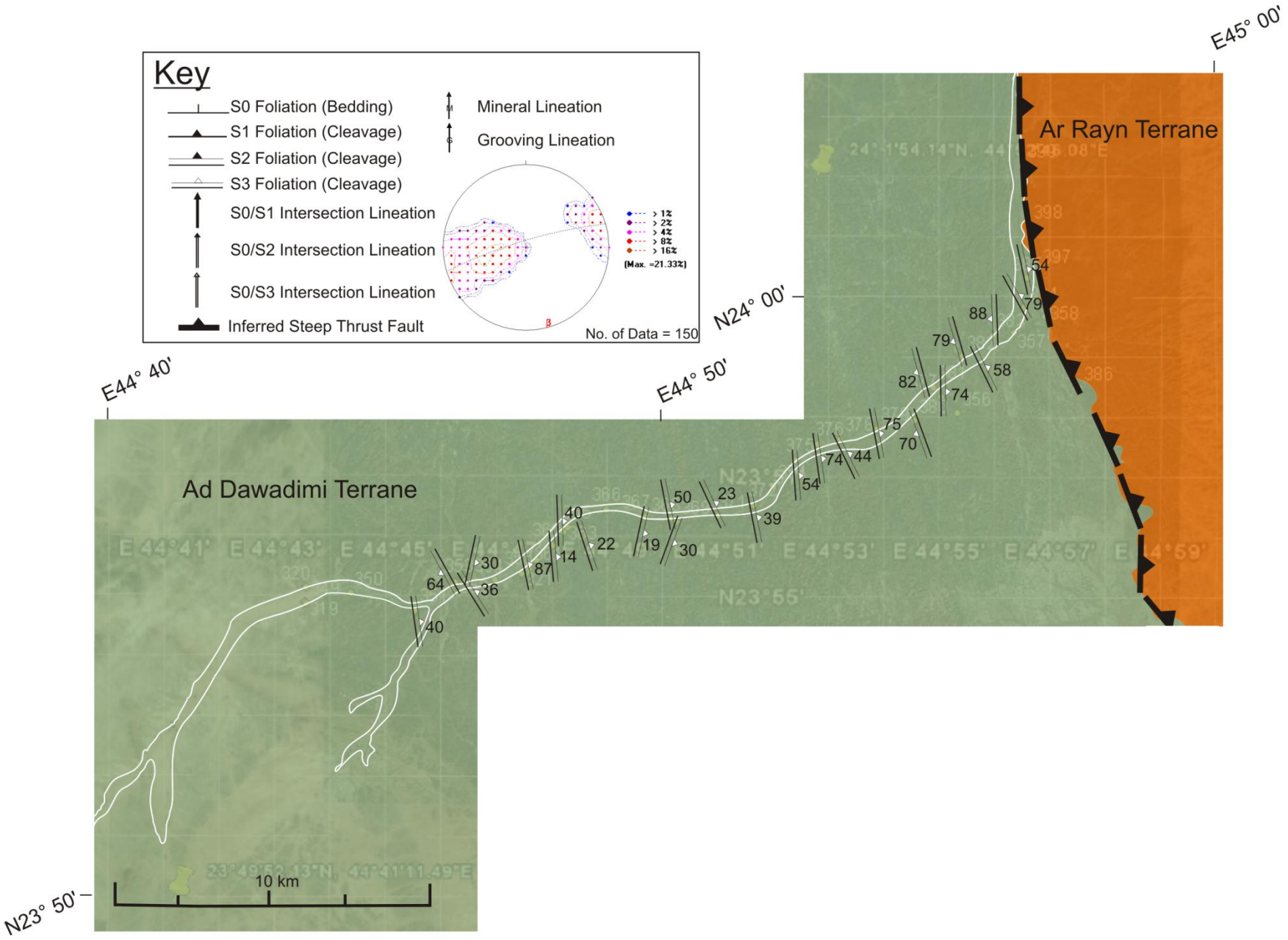
Key
S0 Foliation (Bedding)
S1 Foliation (Cleavage)
S2 Foliation (Cleavage)
S3 Foliation (Cleavage)
S0/S1 Intersection Lineation
S0/S2 Intersection Lineation
S0/S3 Intersection Lineation
Inferred Steep Thrust Fault
Mineral Lineation
Grooving Lineation
> 1%
> 2%
> 4%
> 8%
> 16%
(Max. =21.33%)
No. of Data = 150
Ar Rayn Terrane
Ad Dawadimi Terrane
E45° 00'
N24° 00'
E44° 50'
E44° 40'
N23° 50'
10 km
54
79
88
79
58
82
74
75
70
74
44
54
39
23
50
19
30
22
40
14
87
30
36
64
40

Figure 6

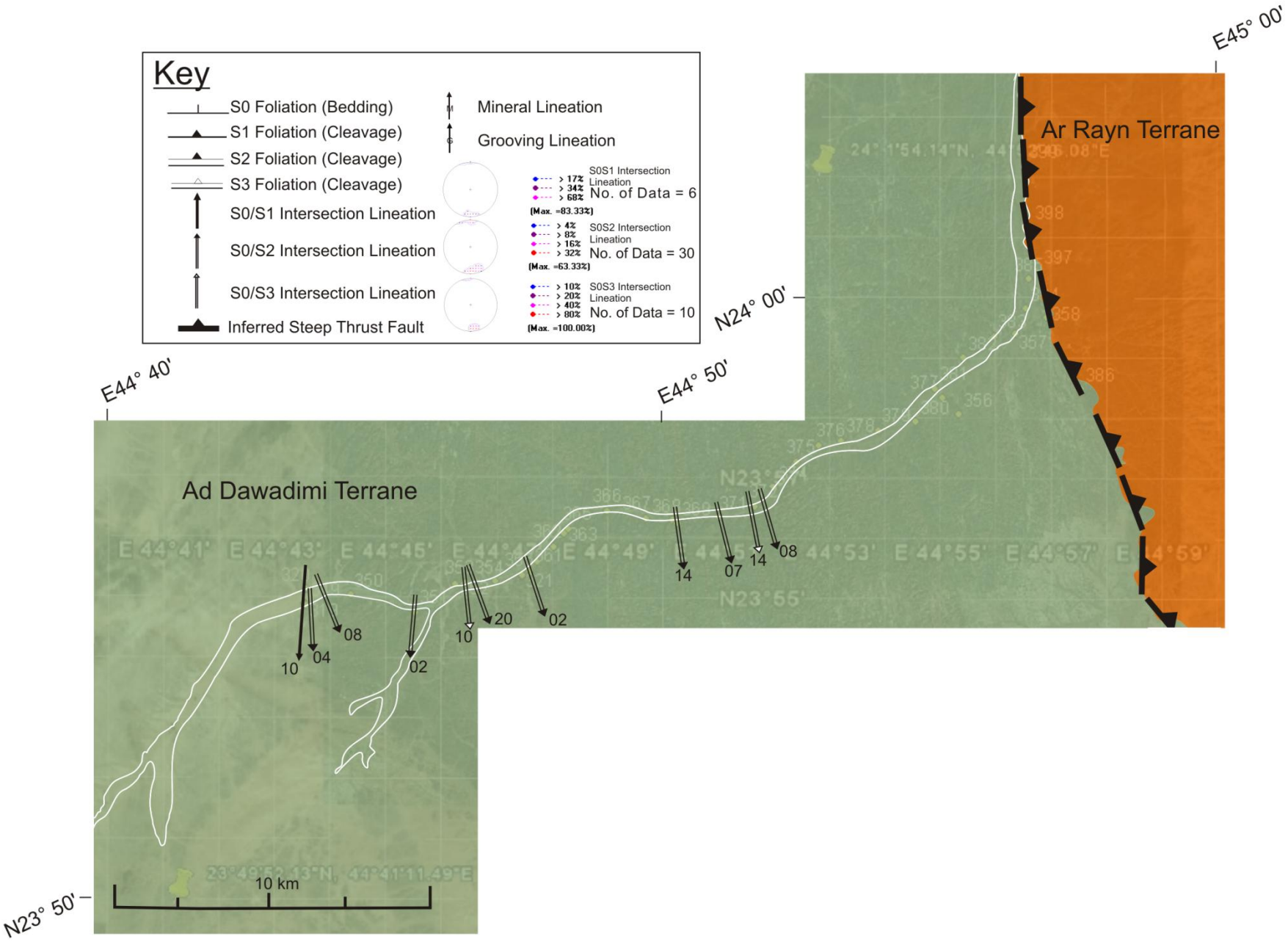
Key
S0 Foliation (Bedding)
S1 Foliation (Cleavage)
S2 Foliation (Cleavage)
S3 Foliation (Cleavage)
S0/S1 Intersection Lineation
S0/S2 Intersection Lineation
S0/S3 Intersection Lineation
Inferred Steep Thrust Fault
Mineral Lineation
Grooving Lineation
S0S1 Intersection Lineation
> 17%
> 34%
> 68%
No. of Data = 6
(Max. =83.33%)
S0S2 Intersection Lineation
> 4%
> 8%
> 16%
> 32%
No. of Data = 30
(Max. =63.33%)
S0S3 Intersection Lineation
> 10%
> 20%
> 40%
> 80%
No. of Data = 10
(Max. =100.00%)
E45° 00'
N24° 00'
E44° 40'
E44° 50'
N23° 50'
Ar Rayn Terrane
Ad Dawadimi Terrane
10 km

Figure 7

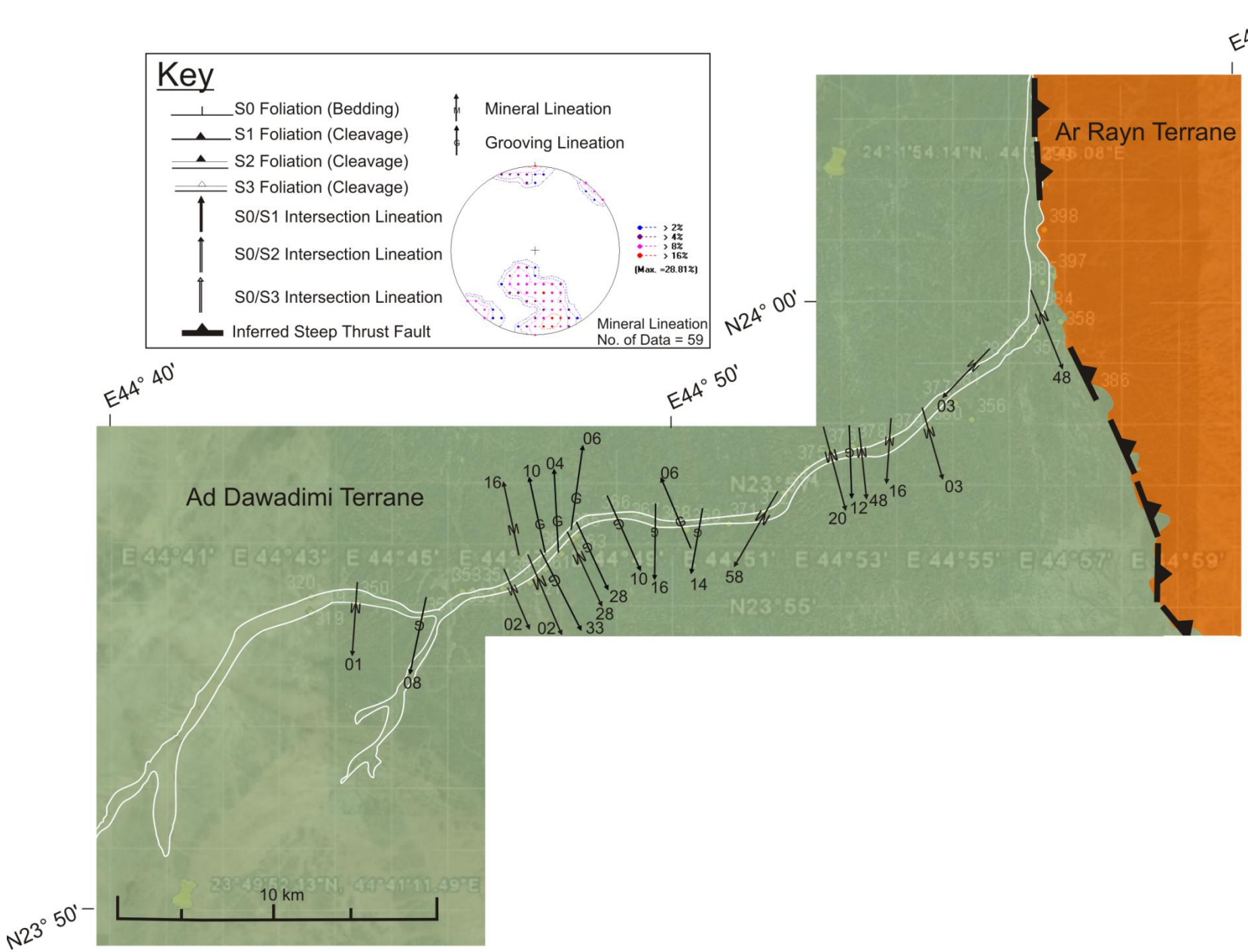
Key
S0 Foliation (Bedding)
S1 Foliation (Cleavage)
S2 Foliation (Cleavage)
S3 Foliation (Cleavage)
S0/S1 Intersection Lineation
S0/S2 Intersection Lineation
S0/S3 Intersection Lineation
Inferred Steep Thrust Fault
Mineral Lineation
Grooving Lineation
> 2%
> 4%
> 8%
> 16%
(Max. =28.81%)
Mineral Lineation
No. of Data = 59
Ar Rayn Terrane
Ad Dawadimi Terrane
E45° 00'
N24° 00'
E44° 40'
E44° 50'
N23° 50'
10 km

Figure 8

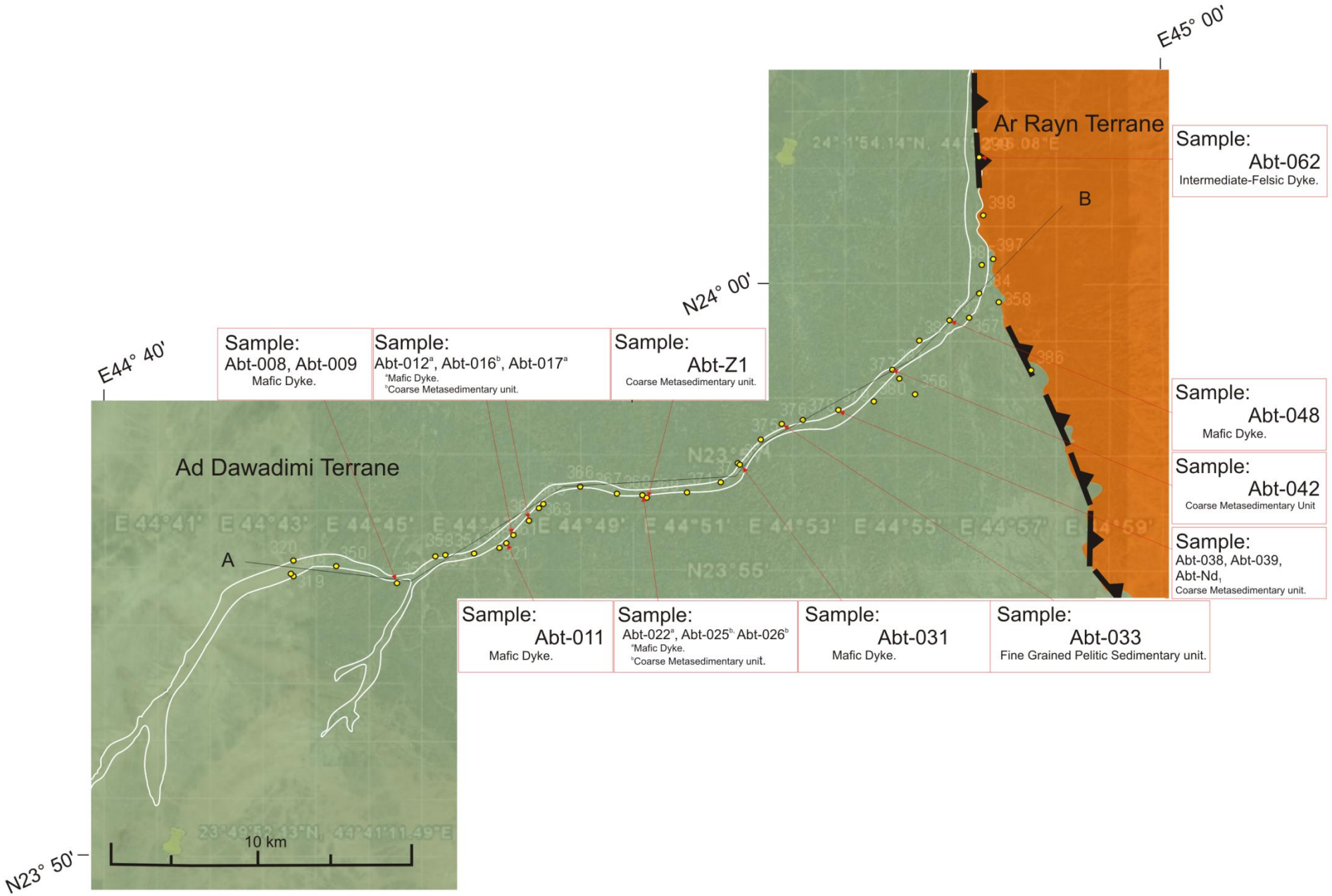
E45° 00'
N24° 00'
E44° 40'
N23° 50'
Ar Rayn Terrane
Ad Dawadimi Terrane
A
B
10 km
Sample:
Abt-062
Intermediate-Felsic Dyke.
Sample:
Abt-008, Abt-009
Mafic Dyke.
Sample:
Abt-012[a], Abt-016[b], Abt-017[a]
[a]Mafic Dyke.
[b]Coarse Metasedimentary unit.
Sample:
Abt-Z1
Coarse Metasedimentary unit.
Sample:
Abt-048
Mafic Dyke.
Sample:
Abt-042
Coarse Metasedimentary Unit
Sample:
Abt-038, Abt-039,
Abt-Nd1
Coarse Metasedimentary unit.
Sample:
Abt-011
Mafic Dyke.
Sample:
Abt-022[a], Abt-025[b] Abt-026[b]
[a]Mafic Dyke.
[b]Coarse Metasedimentary unit.
Sample:
Abt-031
Mafic Dyke.
Sample:
Abt-033
Fine Grained Pelitic Sedimentary unit.

Figure 9

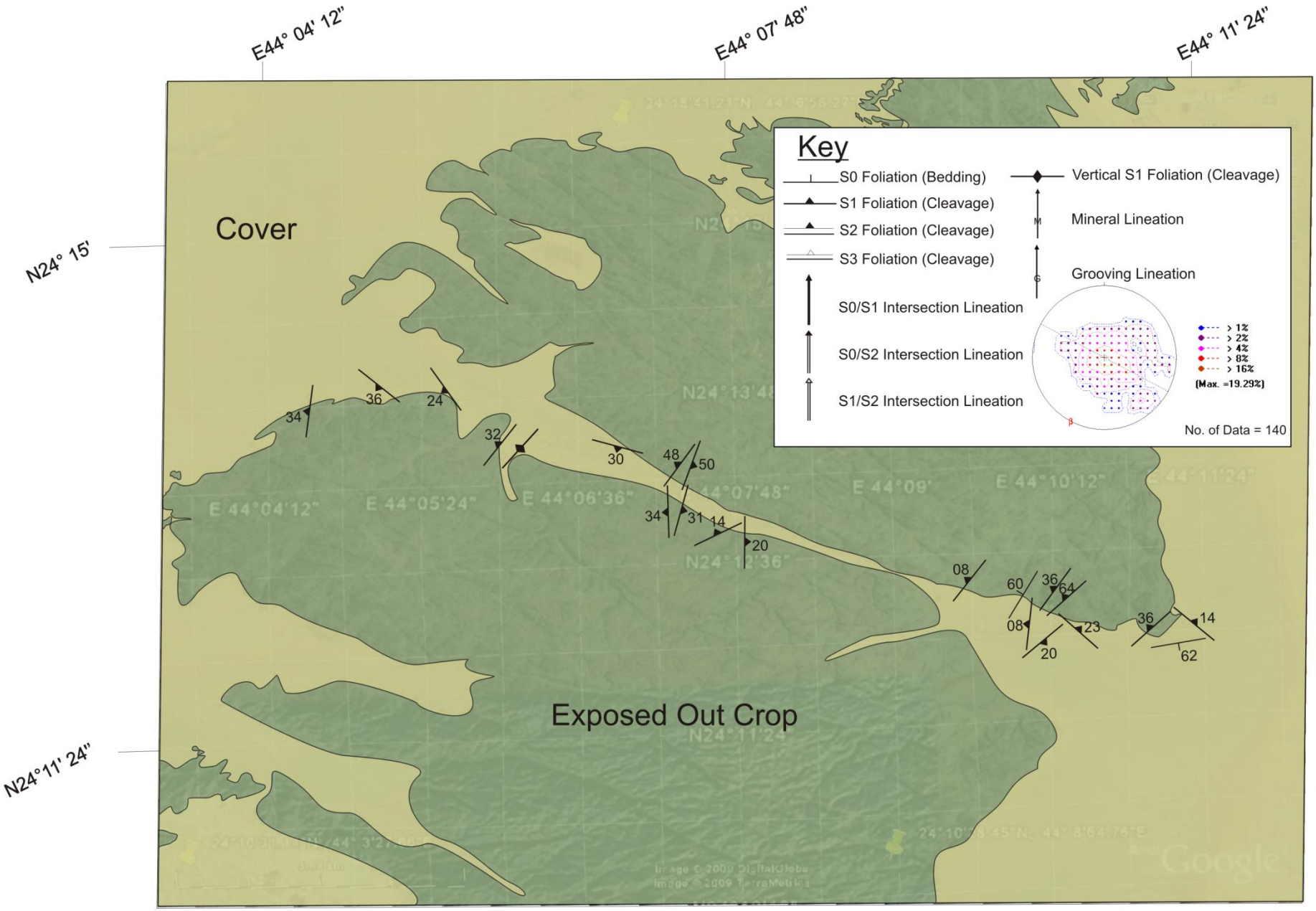
E44° 04' 12"
E44° 07' 48"
E44° 11' 24"
N24° 15'
N24°11' 24"
Cover
Exposed Out Crop
Key
S0 Foliation (Bedding)
S1 Foliation (Cleavage)
S2 Foliation (Cleavage)
S3 Foliation (Cleavage)
S0/S1 Intersection Lineation
S0/S2 Intersection Lineation
S1/S2 Intersection Lineation
Vertical S1 Foliation (Cleavage)
Mineral Lineation
Grooving Lineation
> 1%
> 2%
> 4%
> 8%
> 16%
(Max. =19.29%)
No. of Data = 140
34
36
24
32
30
48
50
34
31
14
20
08
60
36
64
08
23
20
36
14
62

Figure 10

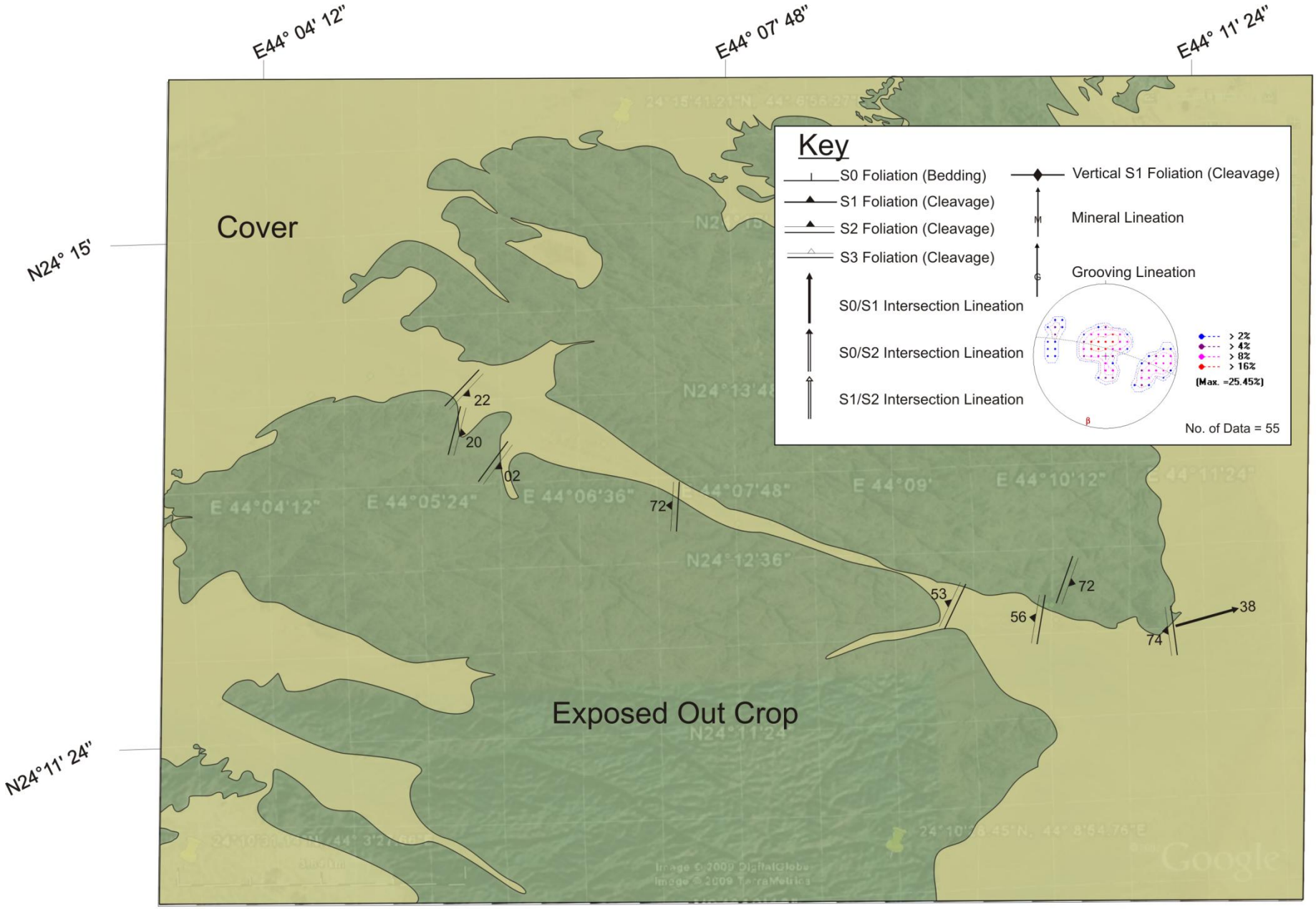
E44° 04' 12"
E44° 07' 48"
E44° 11' 24"
N24° 15'
N24°11' 24"
Cover
Exposed Out Crop
Key
S0 Foliation (Bedding)
S1 Foliation (Cleavage)
S2 Foliation (Cleavage)
S3 Foliation (Cleavage)
S0/S1 Intersection Lineation
S0/S2 Intersection Lineation
S1/S2 Intersection Lineation
Vertical S1 Foliation (Cleavage)
Mineral Lineation
Grooving Lineation
> 2%
> 4%
> 8%
> 16%
(Max. =25.45%)
No. of Data = 55
22
20
02
72
53
72
56
74
38

Figure 11

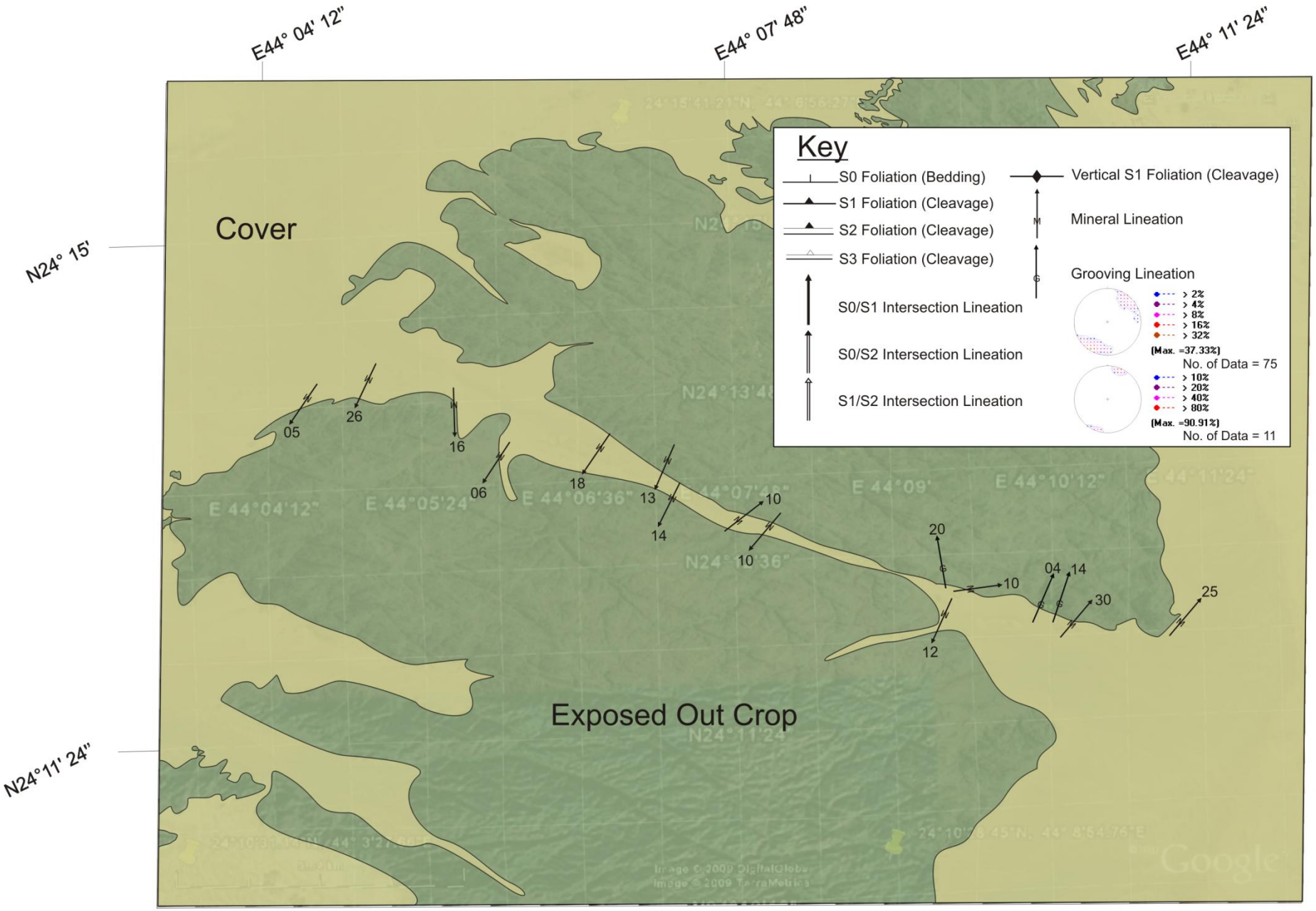
E44° 04' 12"
E44° 07' 48"
E44° 11' 24"
N24° 15'
N24°11' 24"
Cover
Exposed Out Crop
Key
S0 Foliation (Bedding)
S1 Foliation (Cleavage)
S2 Foliation (Cleavage)
S3 Foliation (Cleavage)
S0/S1 Intersection Lineation
S0/S2 Intersection Lineation
S1/S2 Intersection Lineation
Vertical S1 Foliation (Cleavage)
Mineral Lineation
Grooving Lineation
> 2%
> 4%
> 8%
> 16%
> 32%
(Max. =37.33%)
No. of Data = 75
> 10%
> 20%
> 40%
> 80%
(Max. =90.91%)
No. of Data = 11
05
26
16
06
18
13
14
10
10
20
10
04
14
30
25
12
E 44°04'12"
E 44°05'24
E 44°06'36"
E 44°09'
E 44°10'12"
N24°13'48
N24°11'24
Image © 2009 DigitalGlobe
Image © 2009 TerraMetrics
Google

Figure 12

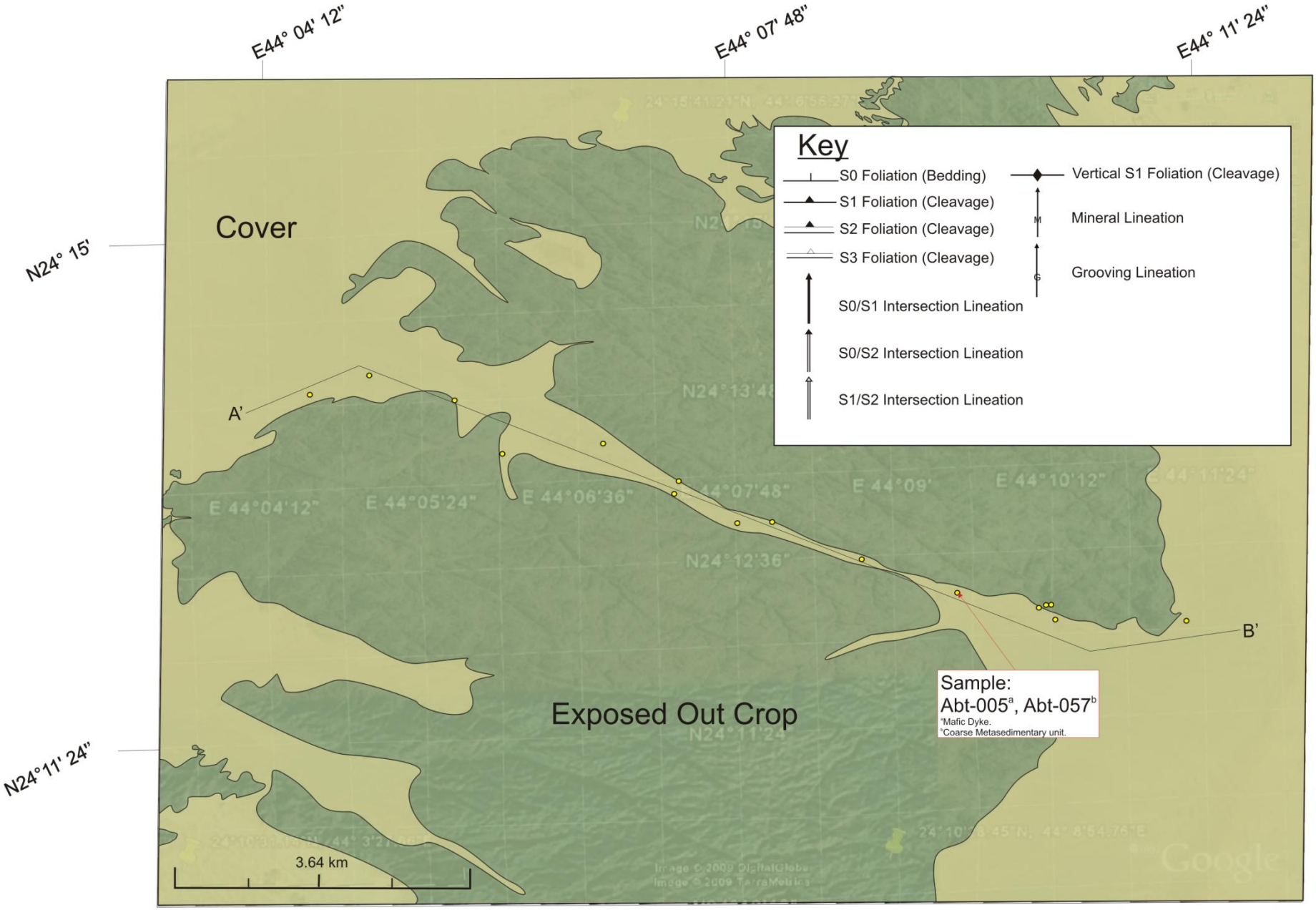
E44° 04' 12"
E44° 07' 48"
E44° 11' 24"
N24° 15'
N24°11' 24"
Cover
Exposed Out Crop
A'
B'
Key
S0 Foliation (Bedding)
S1 Foliation (Cleavage)
S2 Foliation (Cleavage)
S3 Foliation (Cleavage)
S0/S1 Intersection Lineation
S0/S2 Intersection Lineation
S1/S2 Intersection Lineation
Vertical S1 Foliation (Cleavage)
Mineral Lineation
Grooving Lineation
Sample:
Abt-005[a], Abt-057[b]
[a]Mafic Dyke.
[b]Coarse Metasedimentary unit.
3.64 km
E 44°04'12"
E 44°05'24"
E 44°06'36"
E 44°09'
E 44°10'12"
N24°12'36"
Google

Figure 13

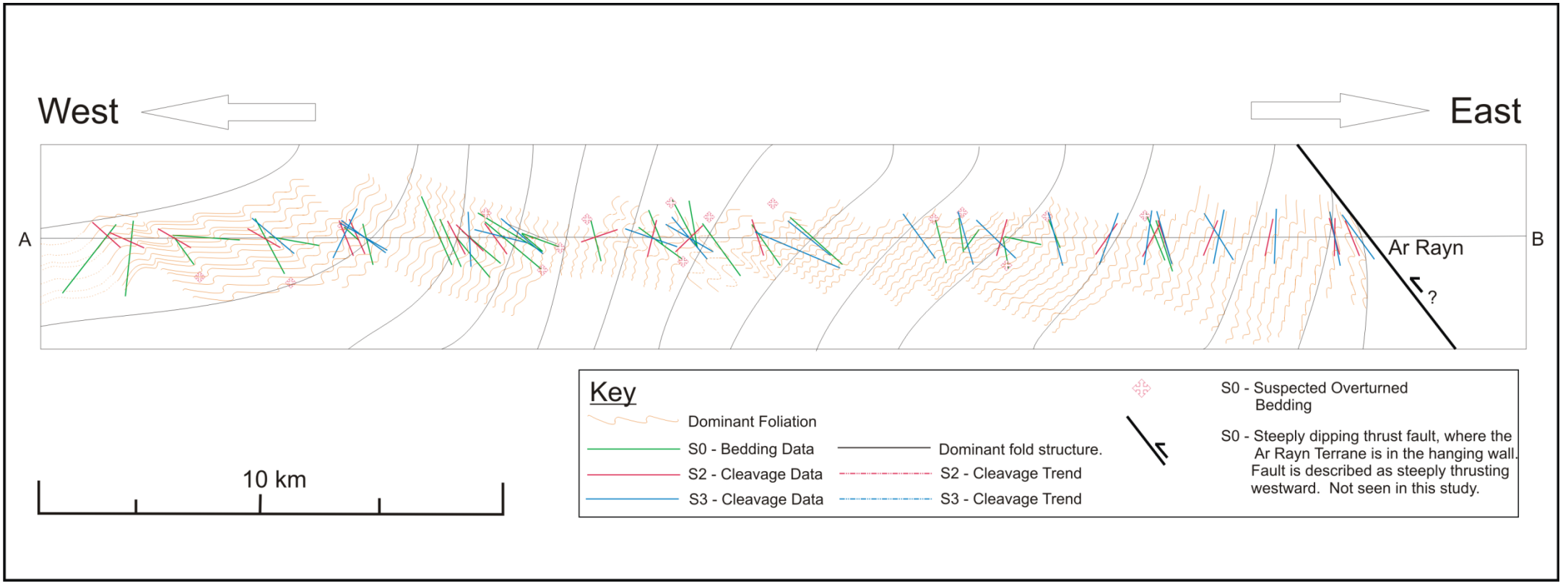
West
East
A
B
Ar Rayn
?
10 km
Key
Dominant Foliation
S0 - Bedding Data
S2 - Cleavage Data
S3 - Cleavage Data
Dominant fold structure.
S2 - Cleavage Trend
S3 - Cleavage Trend
S0 - Suspected Overturned Bedding
S0 - Steeply dipping thrust fault, where the Ar Rayn Terrane is in the hanging wall. Fault is described as steeply thrusting westward. Not seen in this study.

Figure 14

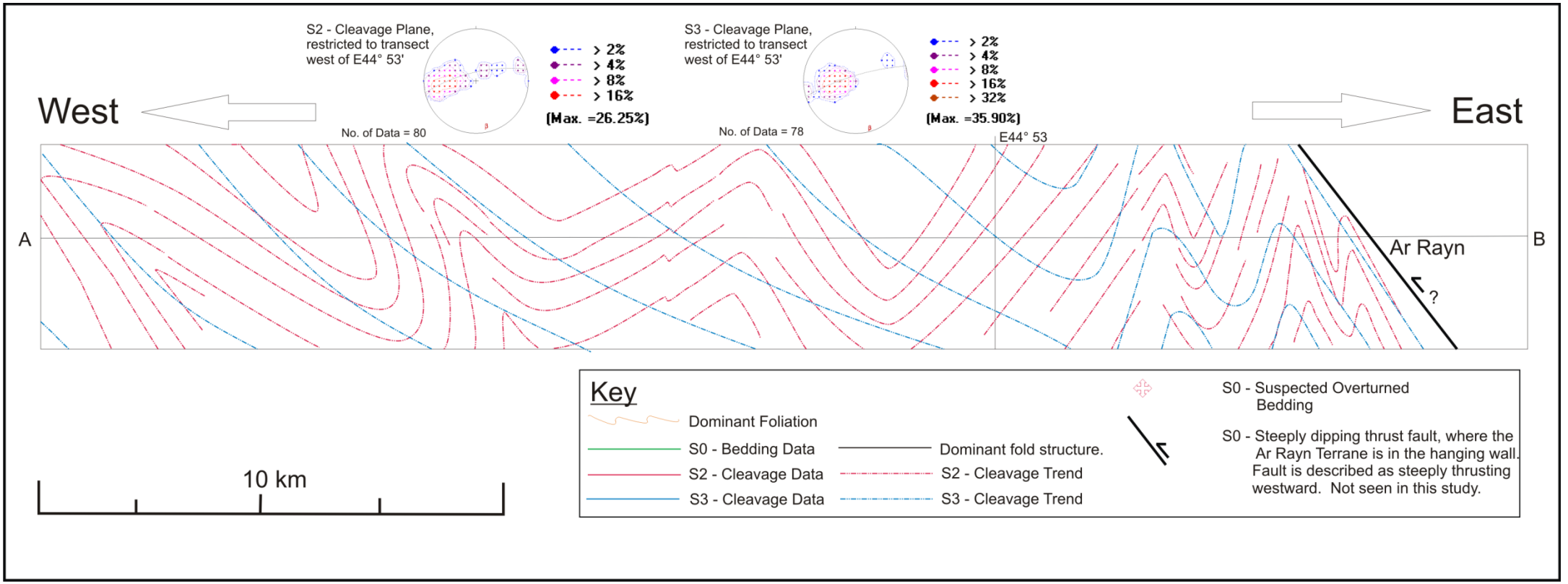
S2 - Cleavage Plane, restricted to transect west of E44° 53'
> 2%
> 4%
> 8%
> 16%
(Max. =26.25%)
No. of Data = 80
S3 - Cleavage Plane, restricted to transect west of E44° 53'
> 2%
> 4%
> 8%
> 16%
> 32%
(Max. =35.90%)
No. of Data = 78
West
East
E44° 53
A
B
Ar Rayn
?
10 km
Key
Dominant Foliation
S0 - Bedding Data
S2 - Cleavage Data
S3 - Cleavage Data
Dominant fold structure.
S2 - Cleavage Trend
S3 - Cleavage Trend
S0 - Suspected Overturned Bedding
S0 - Steeply dipping thrust fault, where the Ar Rayn Terrane is in the hanging wall. Fault is described as steeply thrusting westward. Not seen in this study.

Figure 15

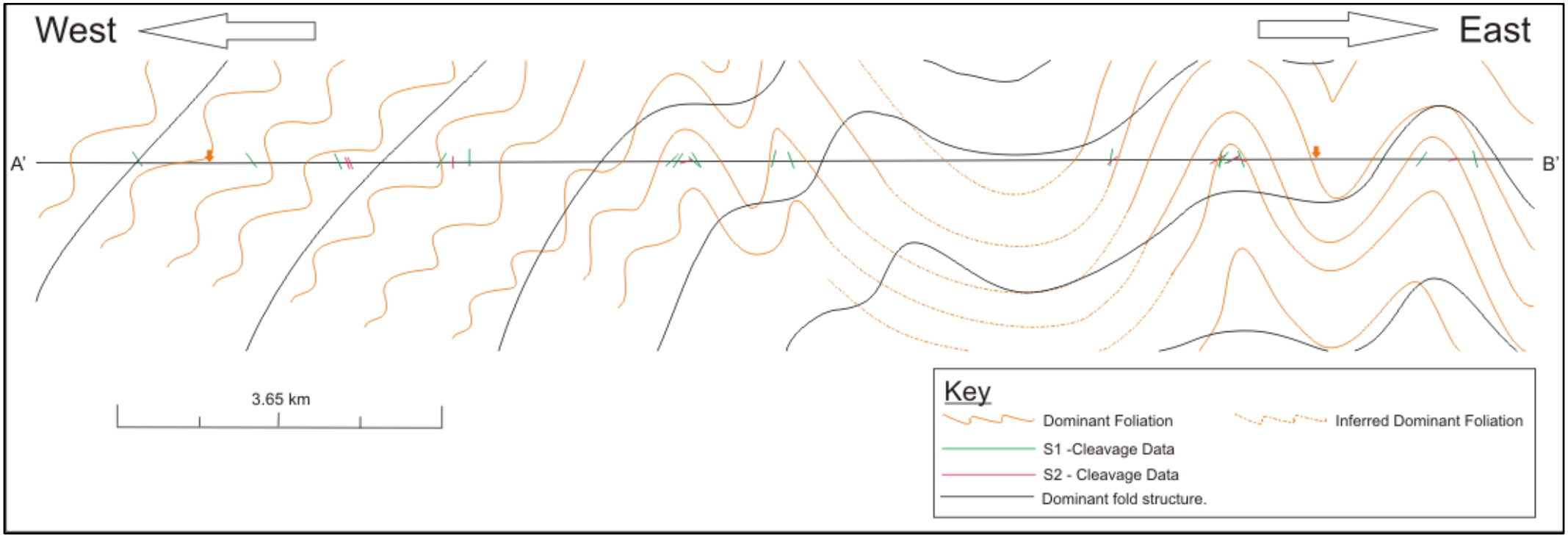
West
East
A'
B'
3.65 km
Key
Dominant Foliation
Inferred Dominant Foliation
S1 -Cleavage Data
S2 - Cleavage Data
Dominant fold structure.

Figure 16

Eastern Transect

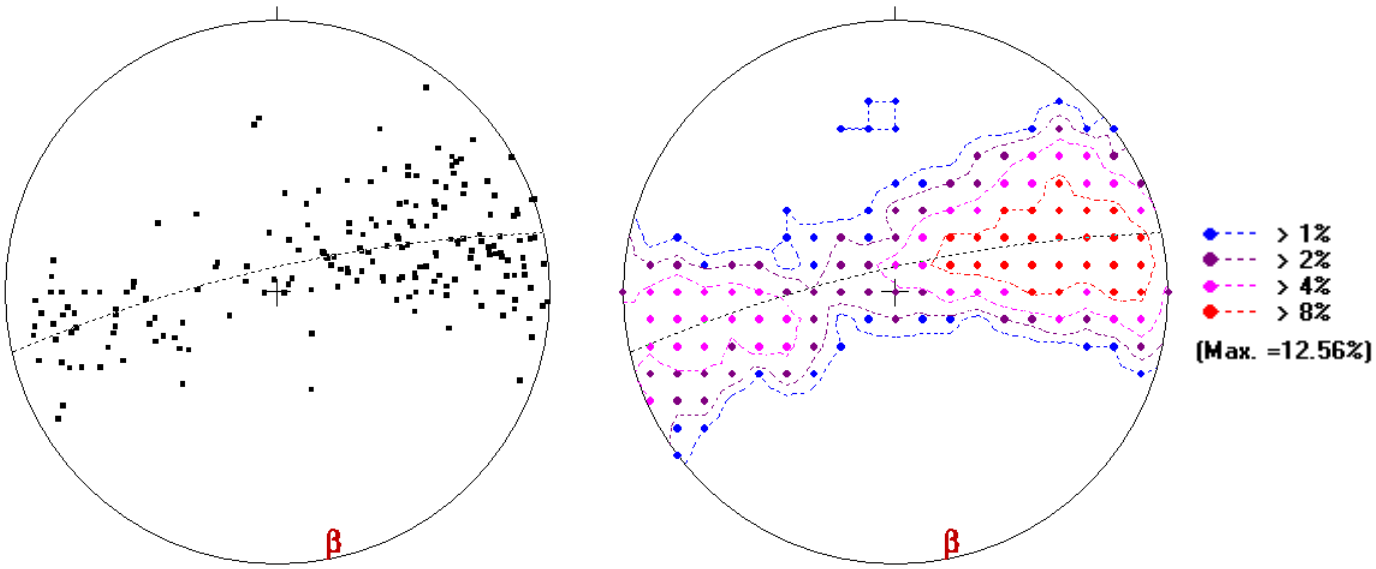

Figure 17: (S0) Bedding Plane

No. of Data = 199
Mean Principal Orientation = 58/253
Mean Resultant dir'n = 29-245
Mean Resultant length = 0.65
(Variance = 0.35)
Calculated. girdle: 82/347
Calculated beta axis: 8-167

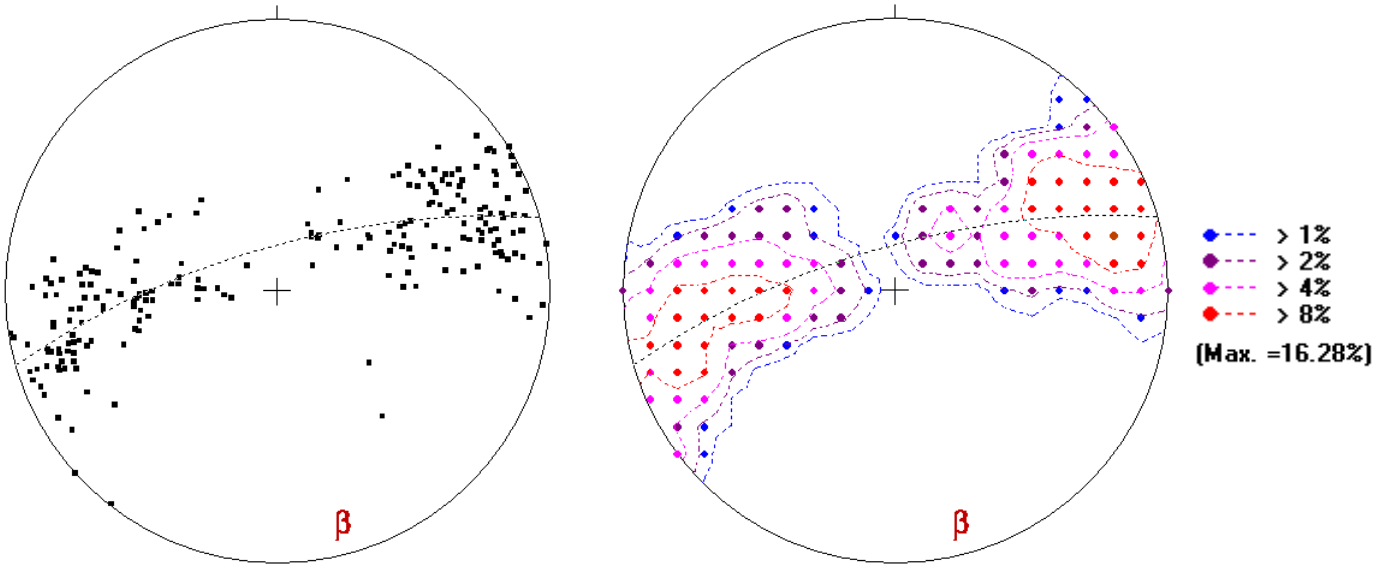

Figure 18: (S2) Cleavage Plane

No. of Data = 215
Mean Principal Orientation = 87/253
Mean Resultant dir'n = 16-205
Mean Resultant length = 0.50
(Variance = 0.50)
Calculated. girdle: 77/344
Calculated beta axis: 13-164

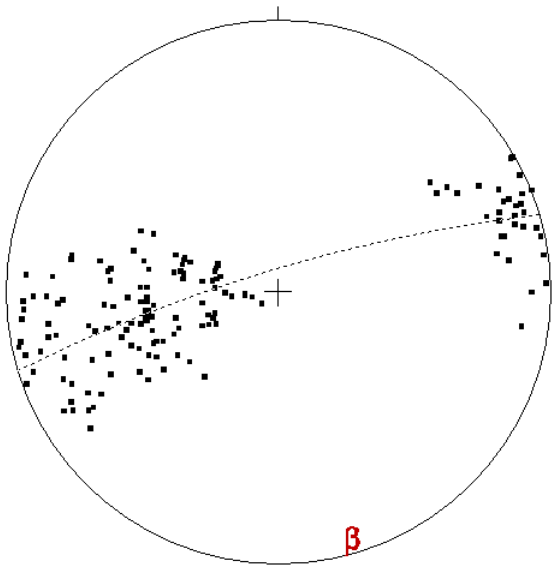

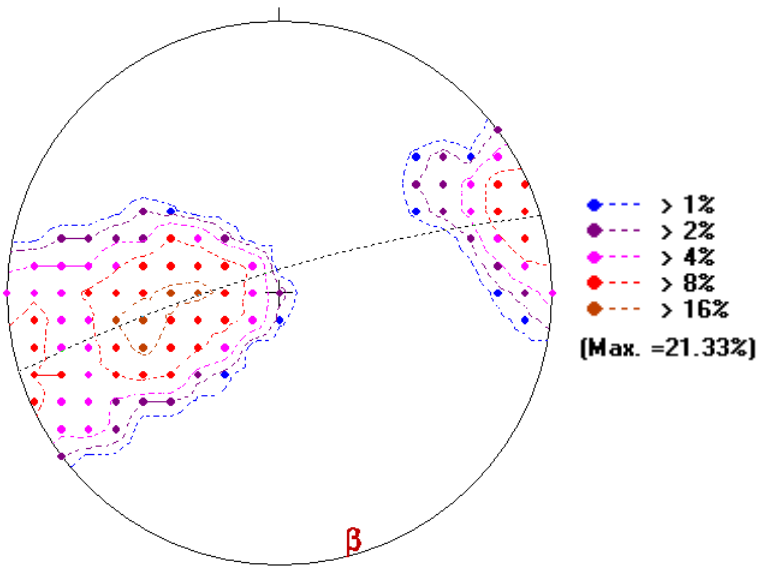

No. of Data = 150
Mean Principal Orientation = 55/078
Mean Resultant dir'n = 30-086
Mean Resultant length = 0.63
(Variance = 0.37)
Calculated. girdle: 83/343
Calculated beta axis: 7-163

Figure 19: (S3) Cleavage Plane

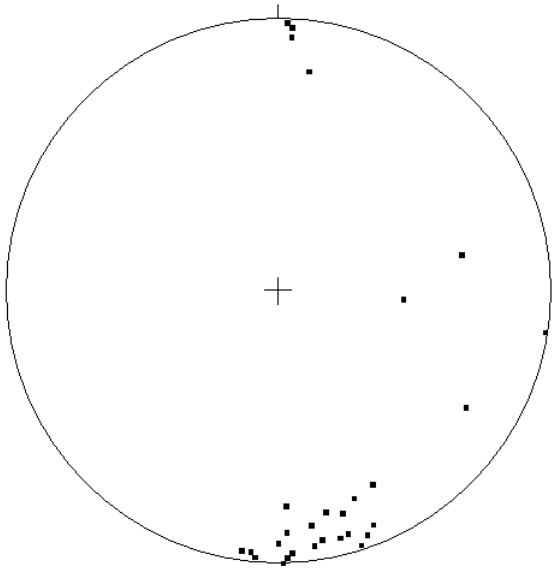

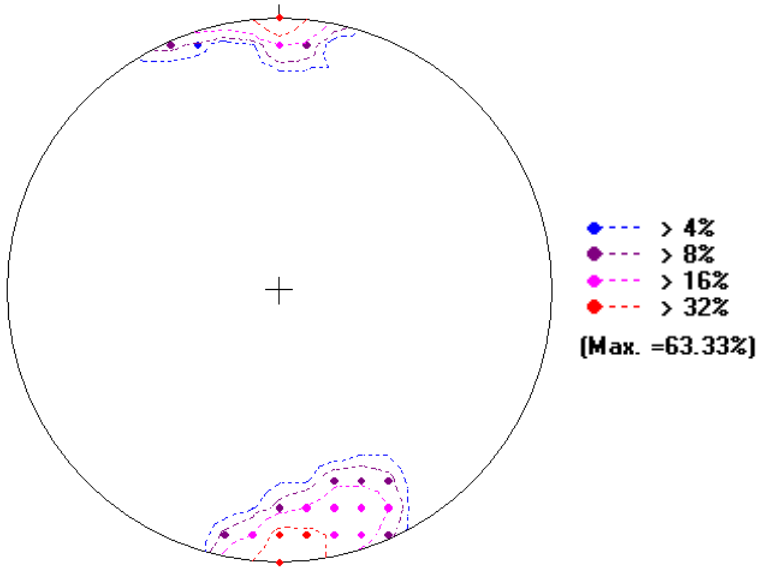

No. of Data = 30
Mean Principal Direction = 8-171
Mean Resultant dir'n = 17/159
Mean Resultant length = 0.66
(Variance = 0.34)
Calculated. girdle: 32/094

Figure 20: (S0/S2) Intersection Lineation

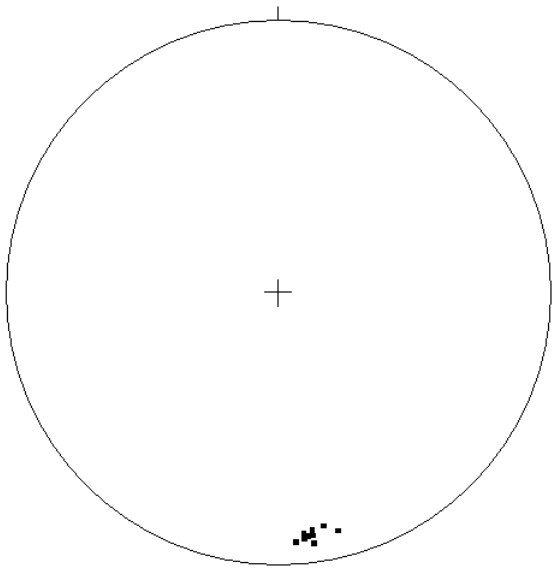

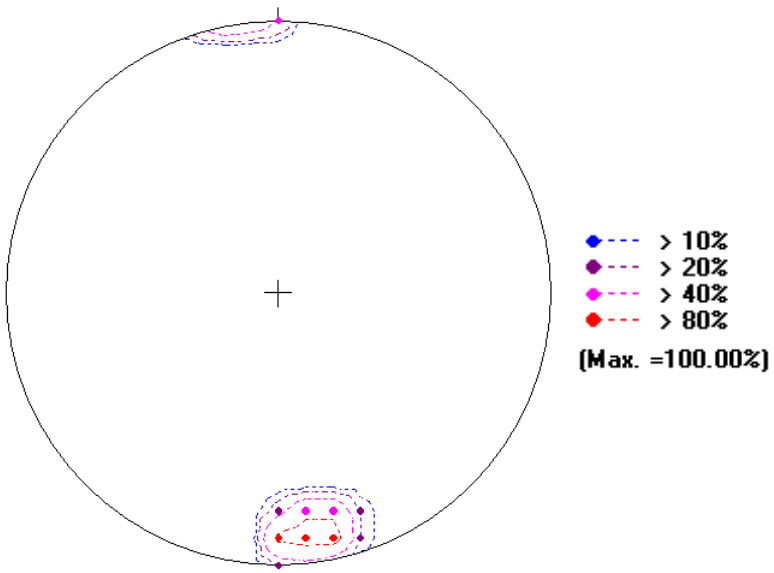

No. of Data = 10
Mean Principal Direction = 11-172
Mean Resultant dir'n = 11/172
Mean Resultant length = 1.00
(Variance = 0.00)
Calculated. girdle: 21/113

Figure 21: (S0/S3) Intersection Lineation

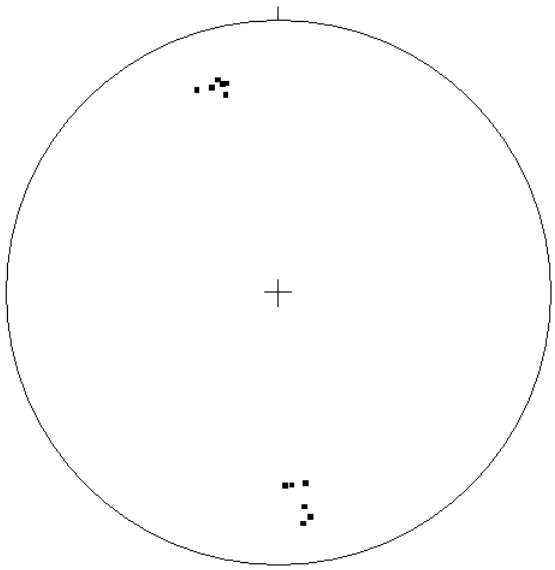

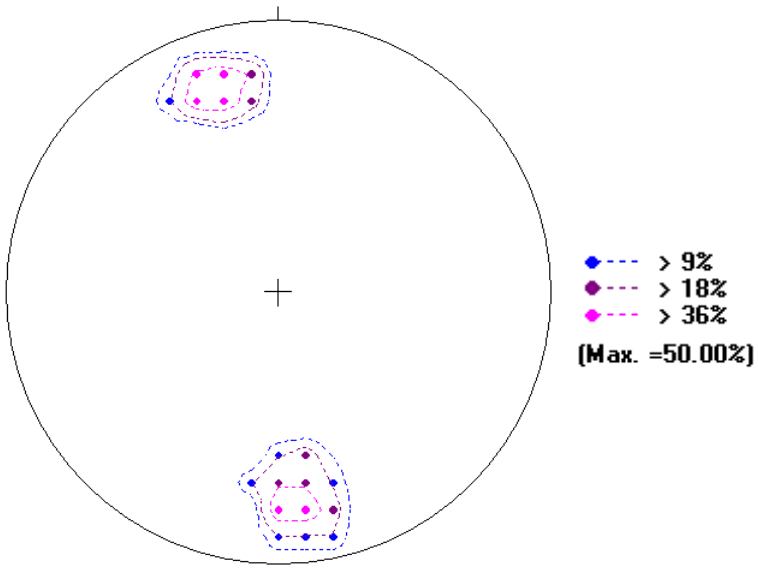

No. of Data = 12
Mean Principal Direction = 1-169
Mean Resultant dir'n = 78/265
Mean Resultant length = 0.40
(Variance = 0.60)
Calculated. girdle: 78/258

Figure 22: (S2/S3) Intersection Lineation

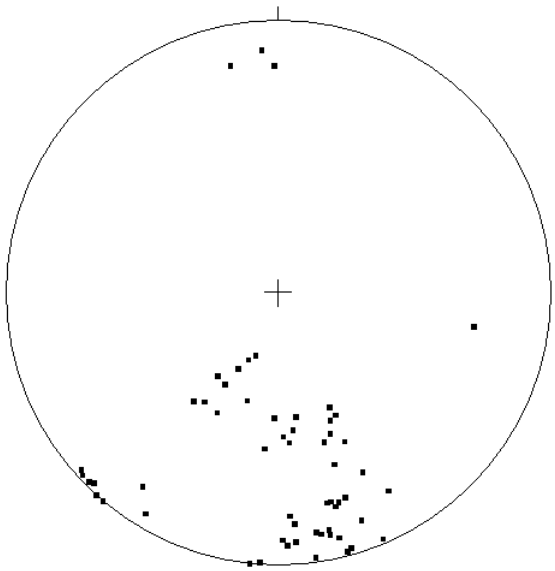

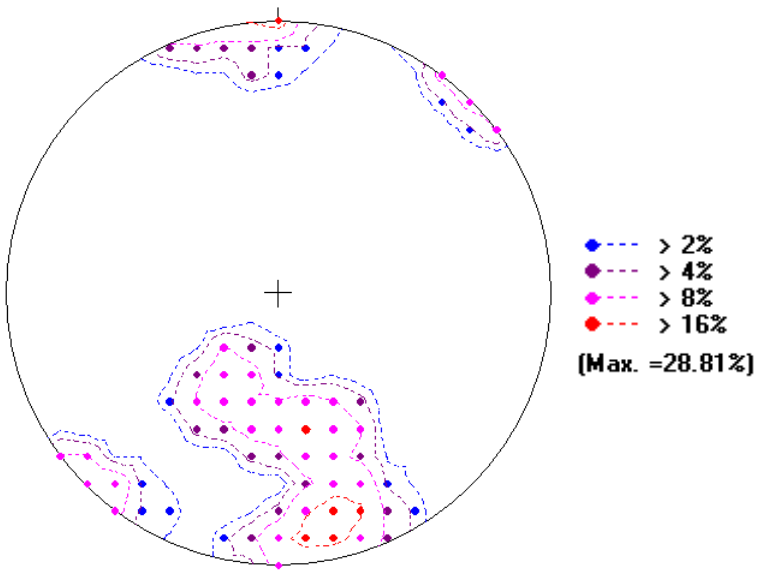

No. of Data = 59
Mean Principal Direction = 26-178
Mean Resultant dir'n = 31/180
Mean Resultant length = 0.78
(Variance = 0.22)
Calculated. girdle: 87/089

Figure 23: Mineral Stretching Lineation

Western Transect

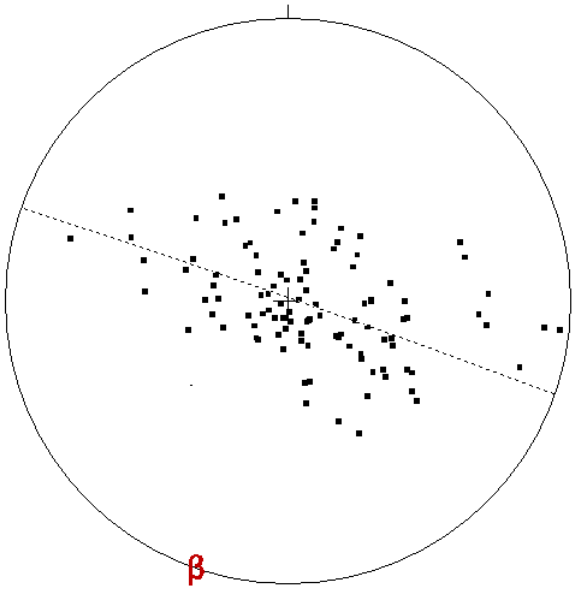

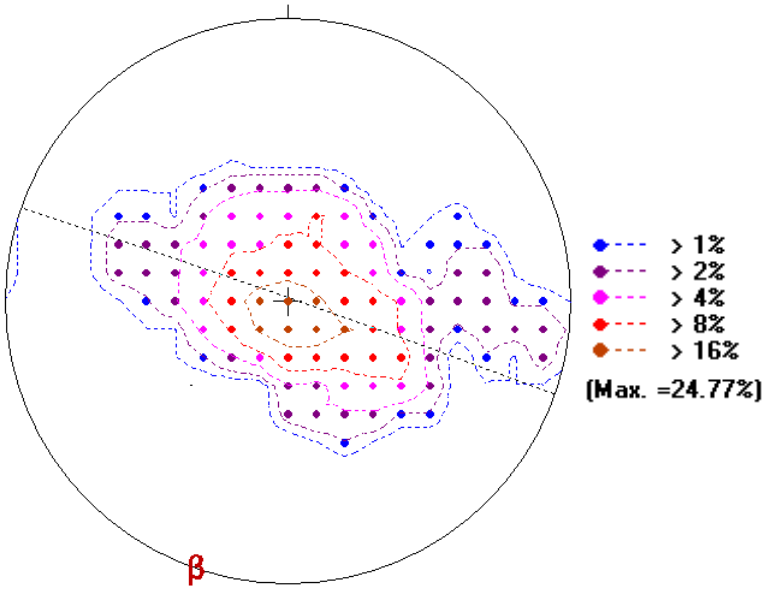

No. of Data = 109
Mean Principal Orientation = 6/278
Mean Resultant dir'n = 7-276
Mean Resultant length = 0.87
(Variance = 0.13)
Calculated. girdle: 89/019
Calculated beta axis: 1-199

Figure 24: (S1) Cleavage Plane

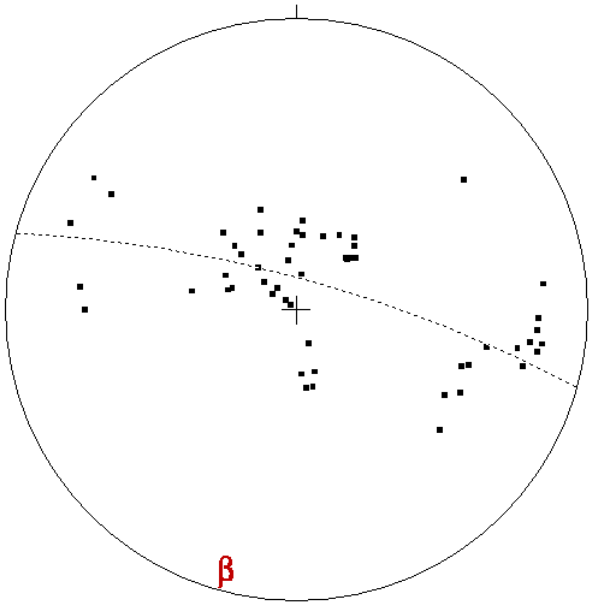

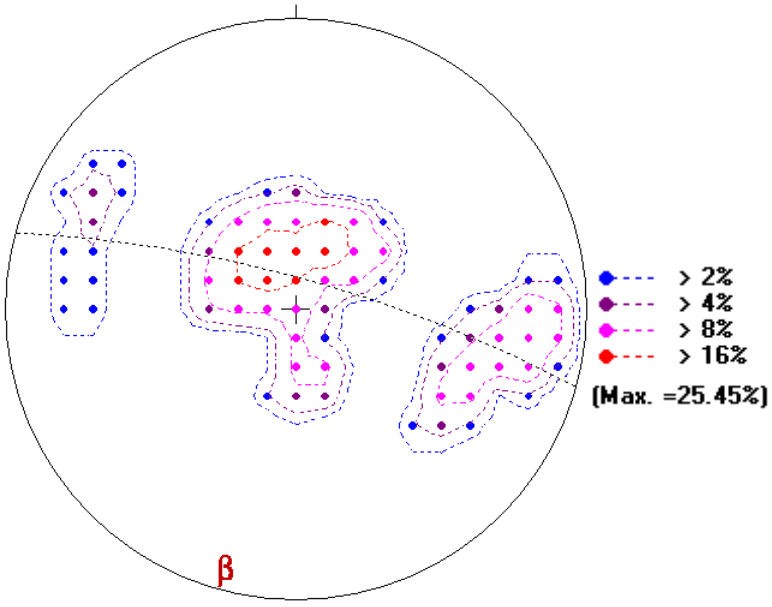

No. of Data = 55
Mean Principal Orientation = 11/229
Mean Resultant dir'n = 13-240
Mean Resultant length = 0.77
(Variance = 0.23)
Calculated. girdle: 81/015
Calculated beta axis: 9-195

Figure 25: (S2) Cleavage Plane

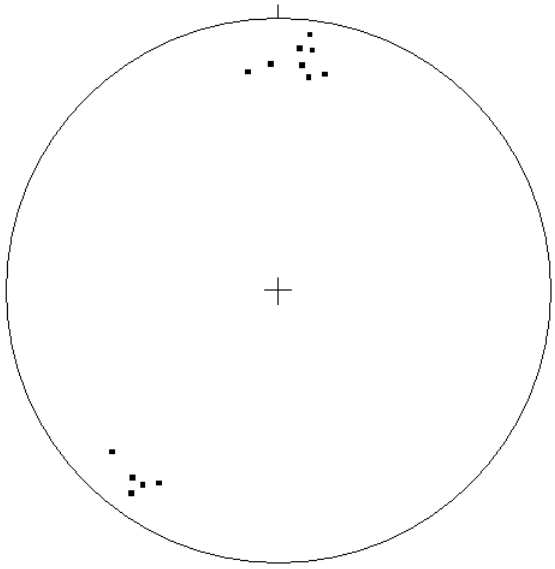

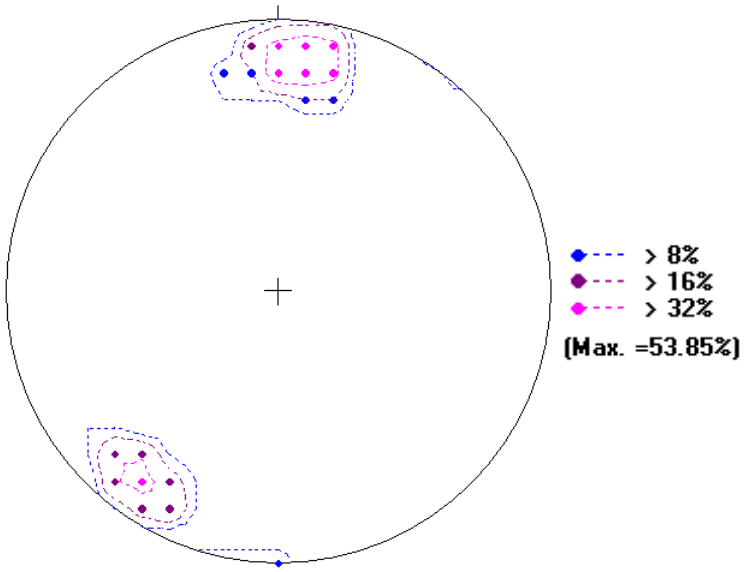

No. of Data = 13
Mean Principal Direction = 5-017
Mean Resultant dir'n = 38/328
Mean Resultant length = 0.43
(Variance = 0.57)
Calculated. girdle: 43/292

Figure 26: (S1S2) Intersection Lineation

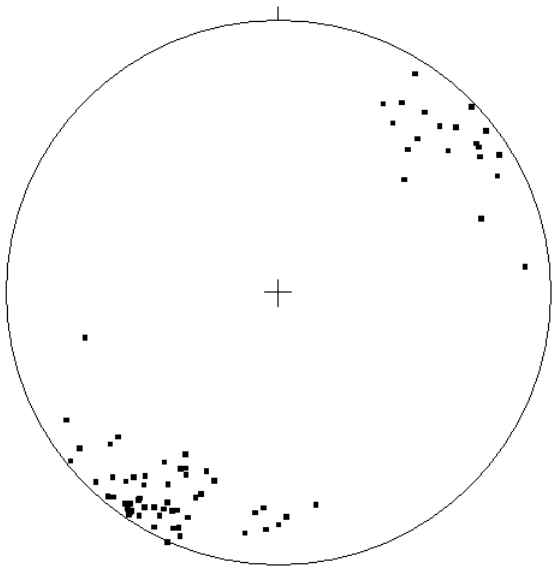

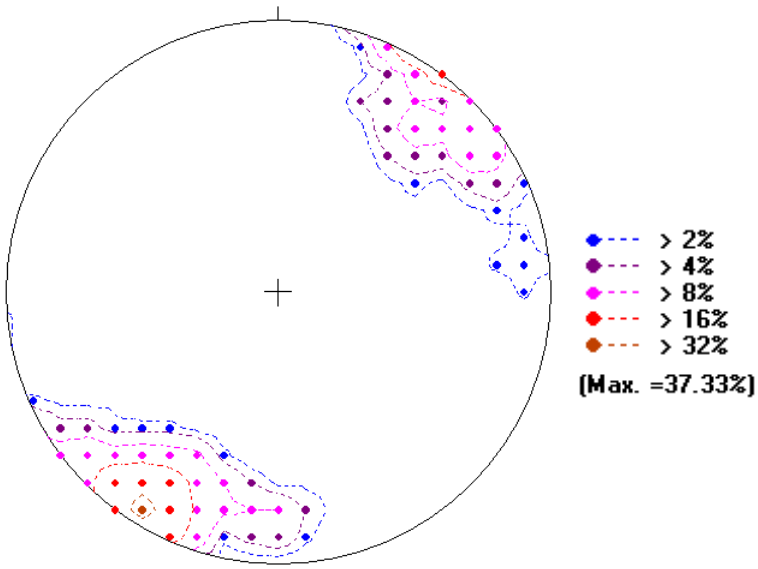

No. of Data = 75
Mean Principal Direction = 6-215
Mean Resultant dir'n = 28/198
Mean Resultant length = 0.50
(Variance = 0.50)
Calculated. girdle: 42/132

Figure 27: Mineral Stretching Lineation

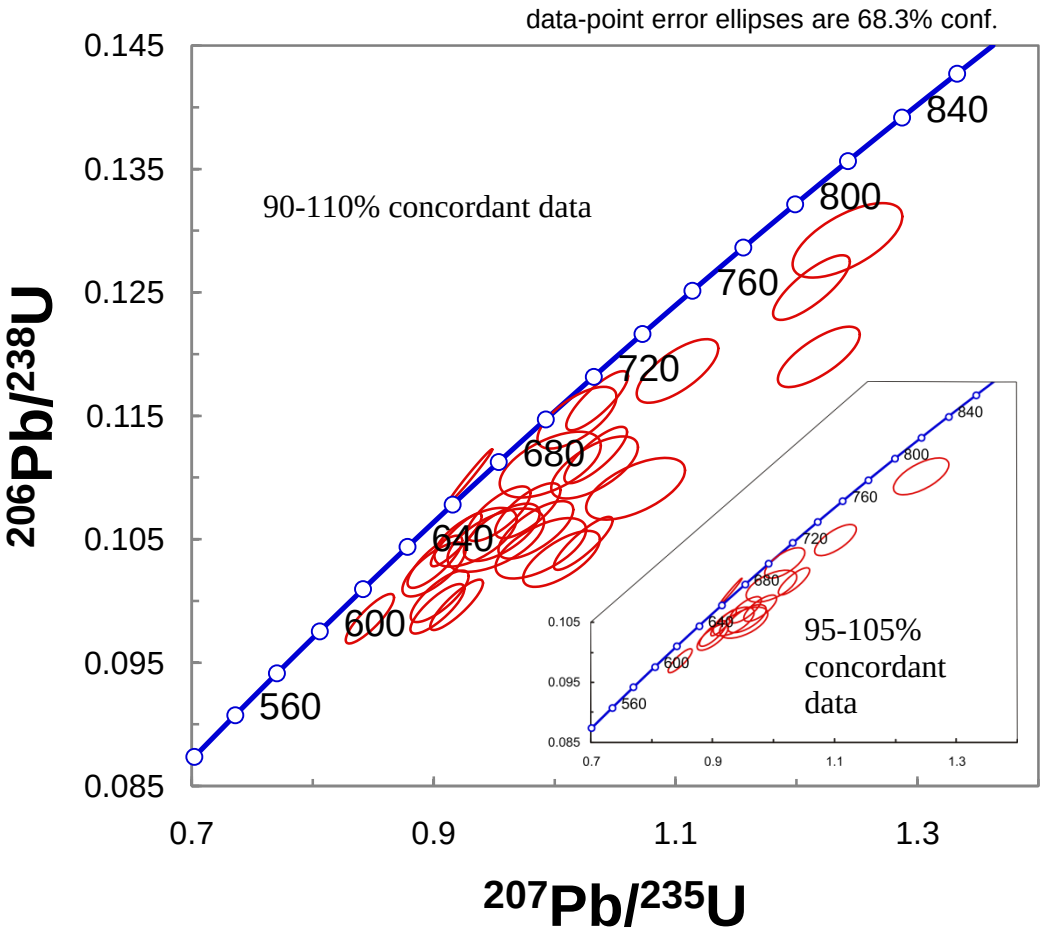

Figure 28

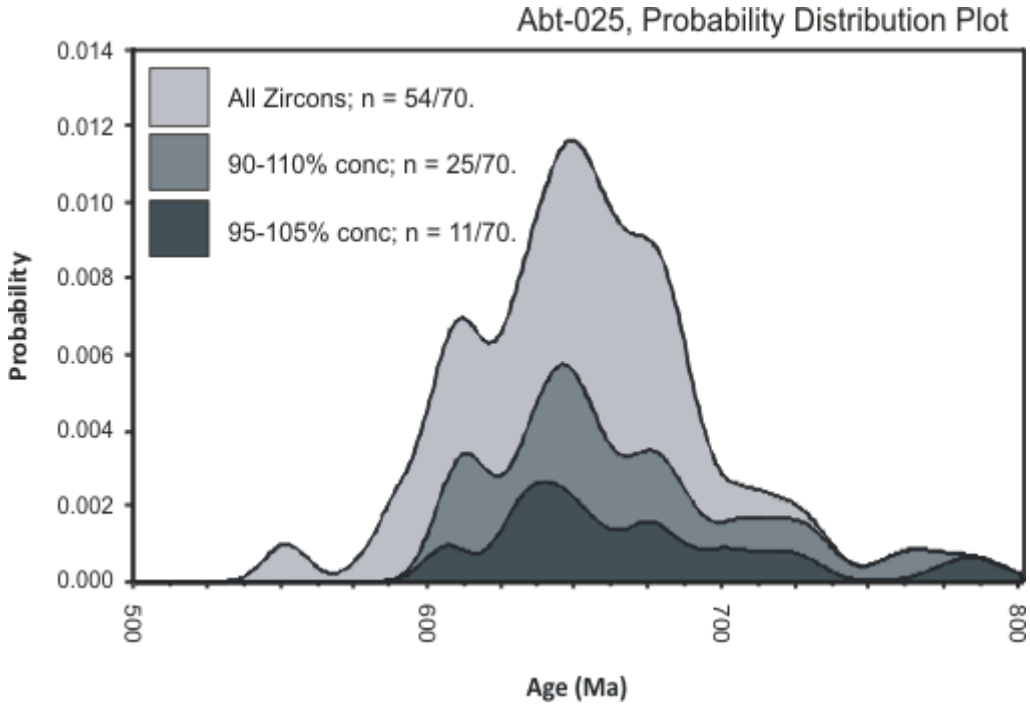

Figure 29

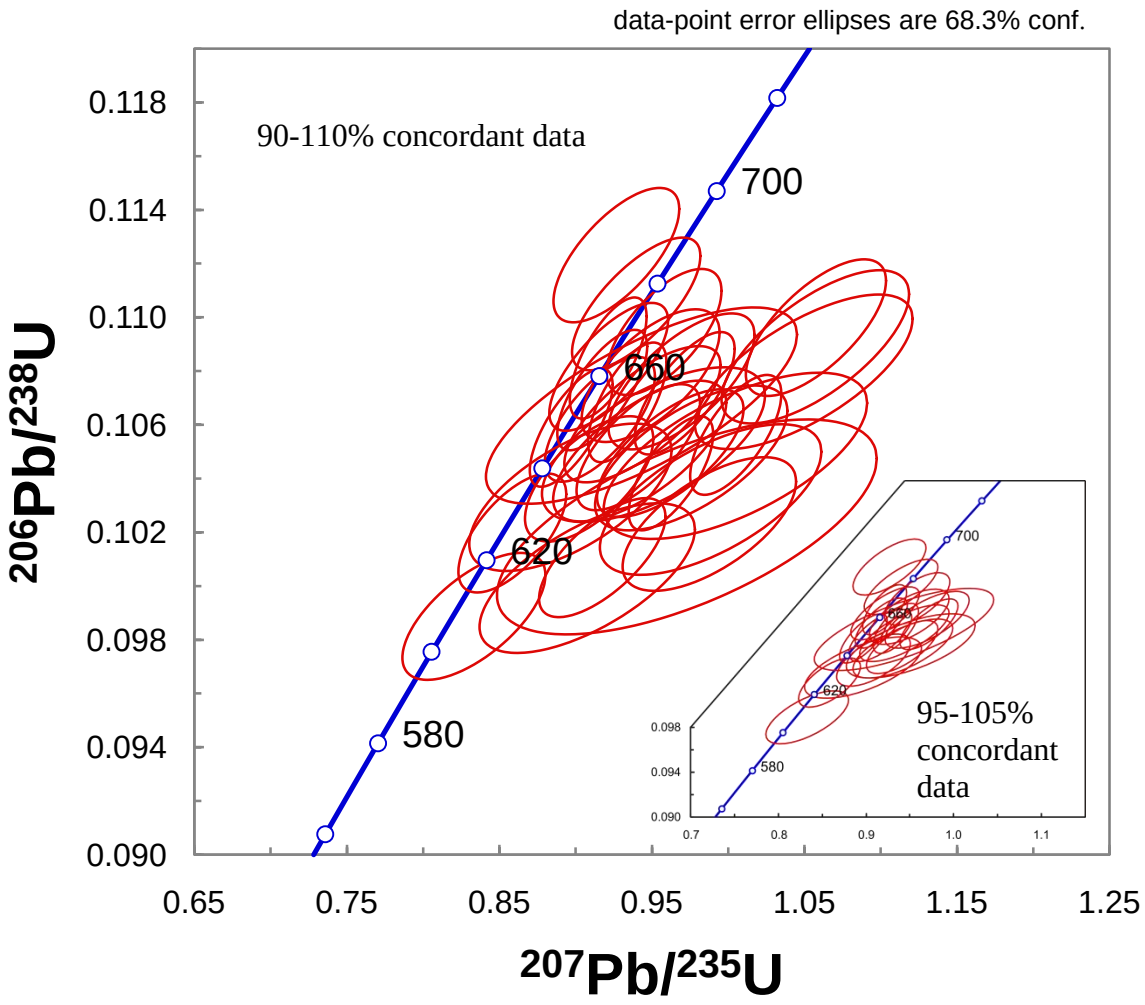

Figure 30

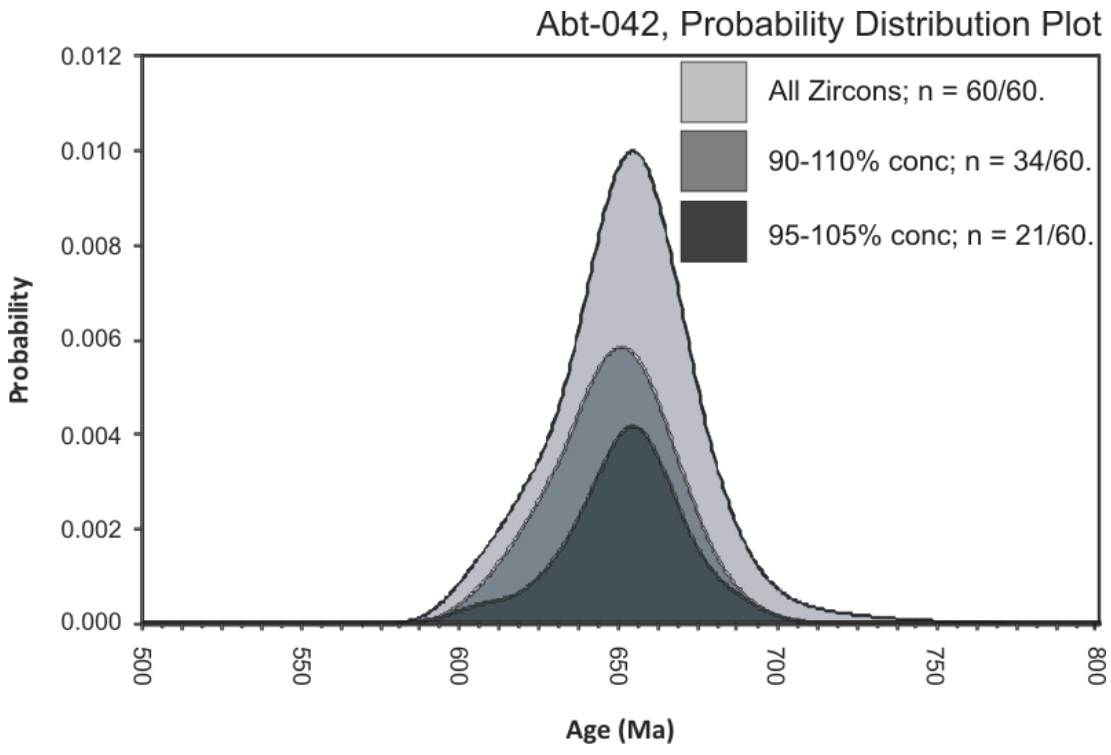

Figure 31

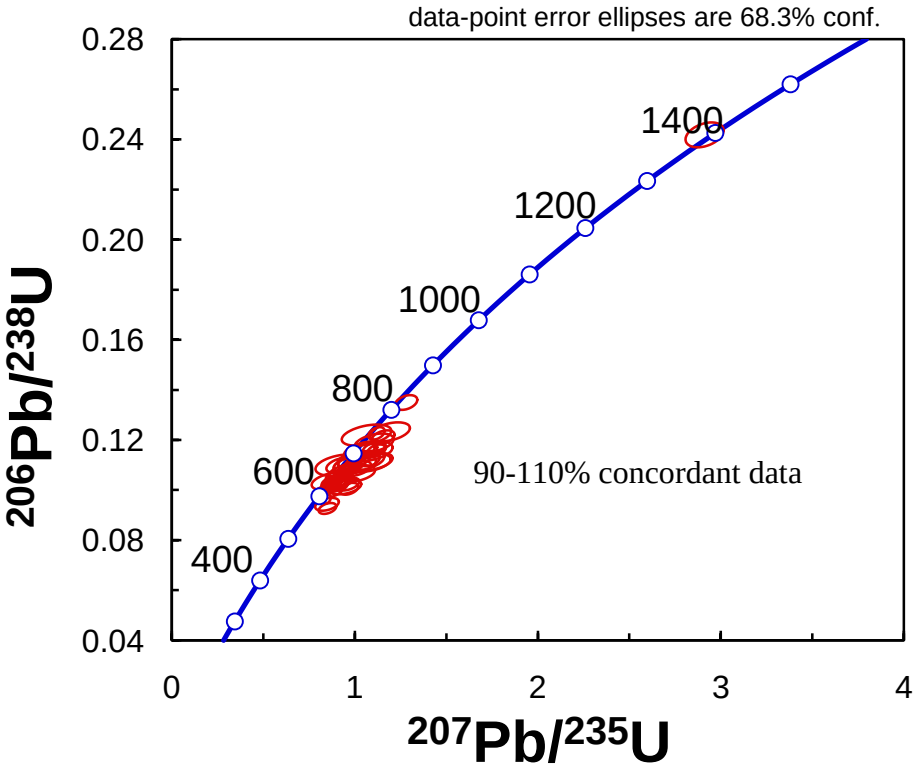

Figure 32

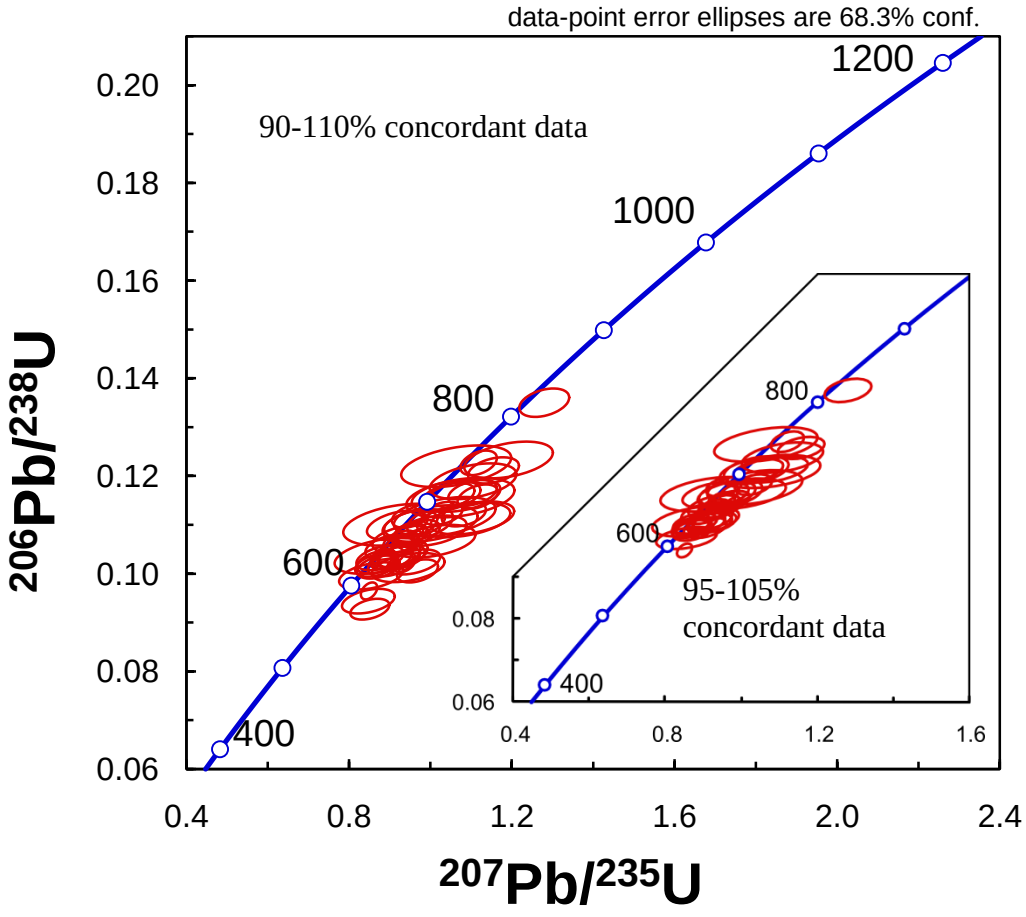

Figure 33

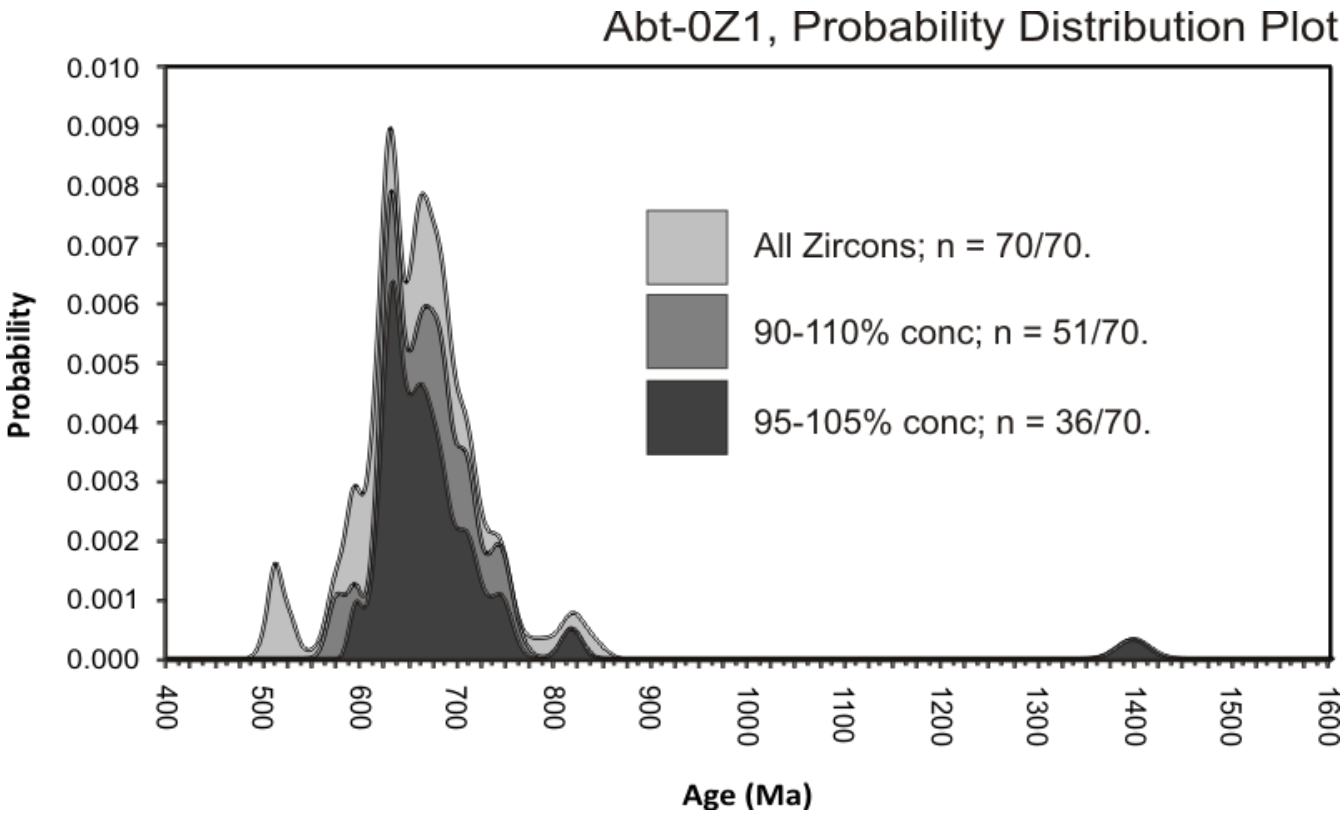
Abt-0Z1, Probability Distribution Plot
Probability
0.010
0.009
0.008
0.007
0.006
0.005
0.004
0.003
0.002
0.001
0.000
All Zircons; n = 70/70.
90-110% conc; n = 51/70.
95-105% conc; n = 36/70.
400
500
600
700
800
900
1000
1100
1200
1300
1400
1500
1600
Age (Ma)

Figure 34

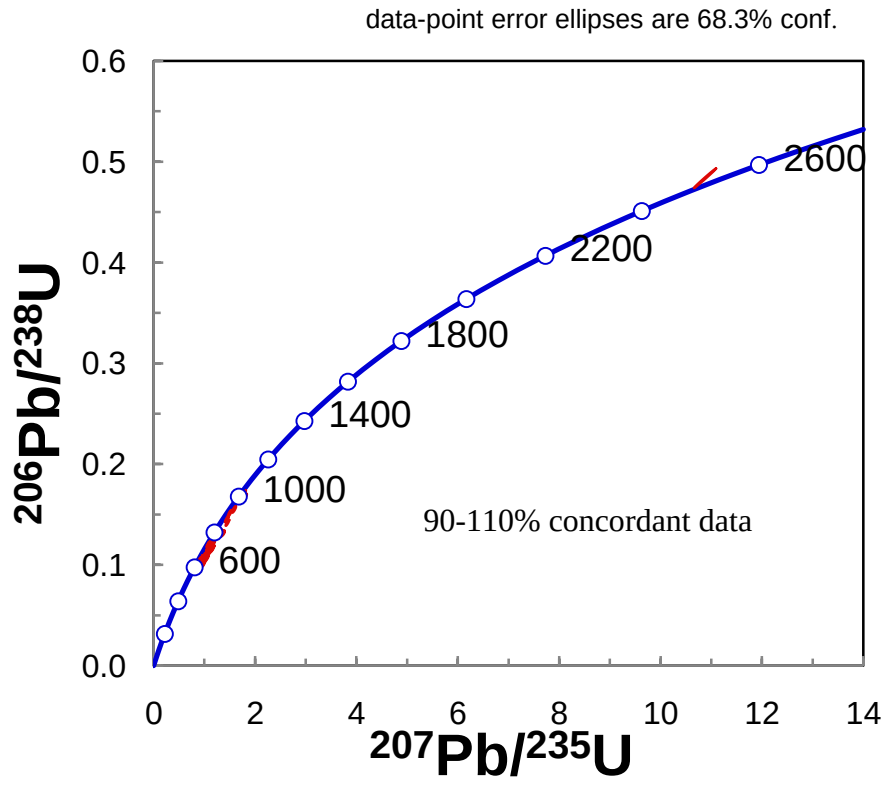

Figure 35

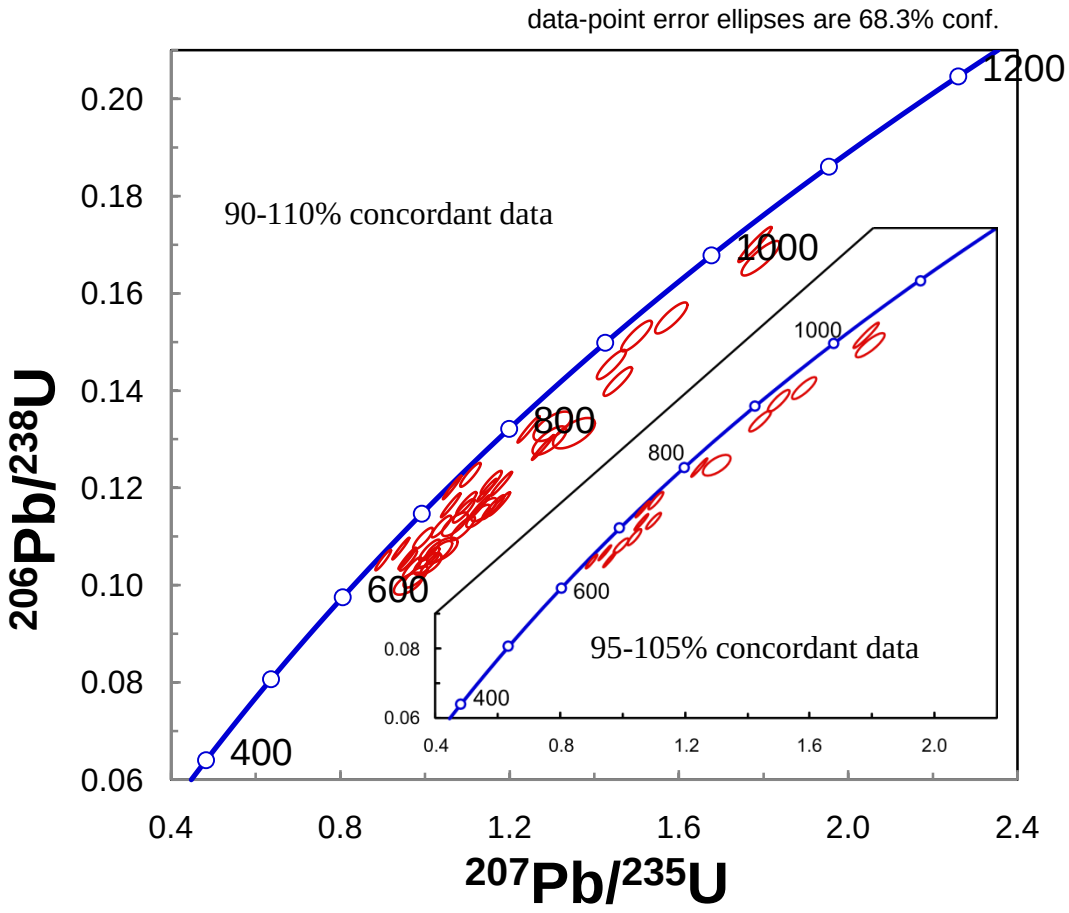

Figure 36

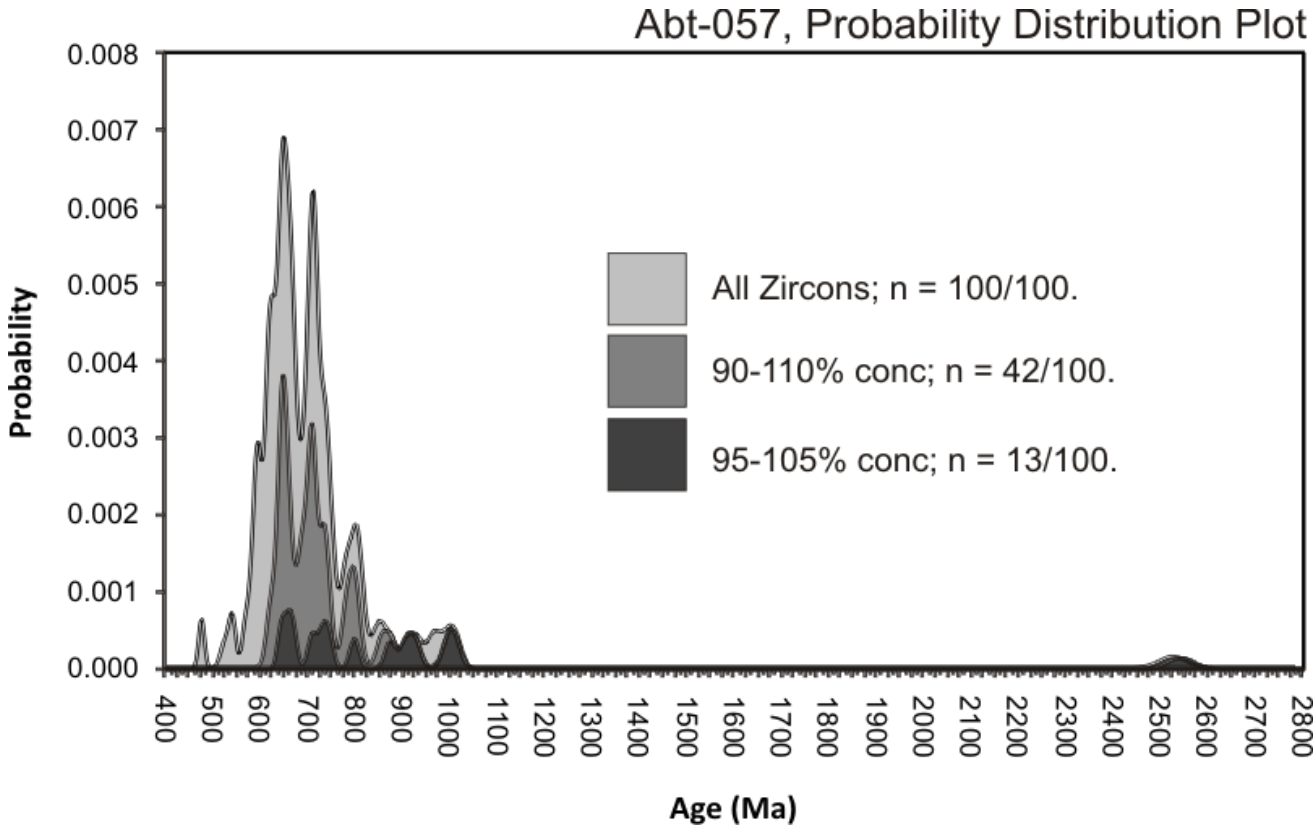
Abt-057, Probability Distribution Plot
Probability
0.008
0.007
0.006
0.005
0.004
0.003
0.002
0.001
0.000
All Zircons; n = 100/100.
90-110% conc; n = 42/100.
95-105% conc; n = 13/100.
400
500
600
700
800
900
1000
1100
1200
1300
1400
1500
1600
1700
1800
1900
2000
2100
2200
2300
2400
2500
2600
2700
2800
Age (Ma)

Figure 37

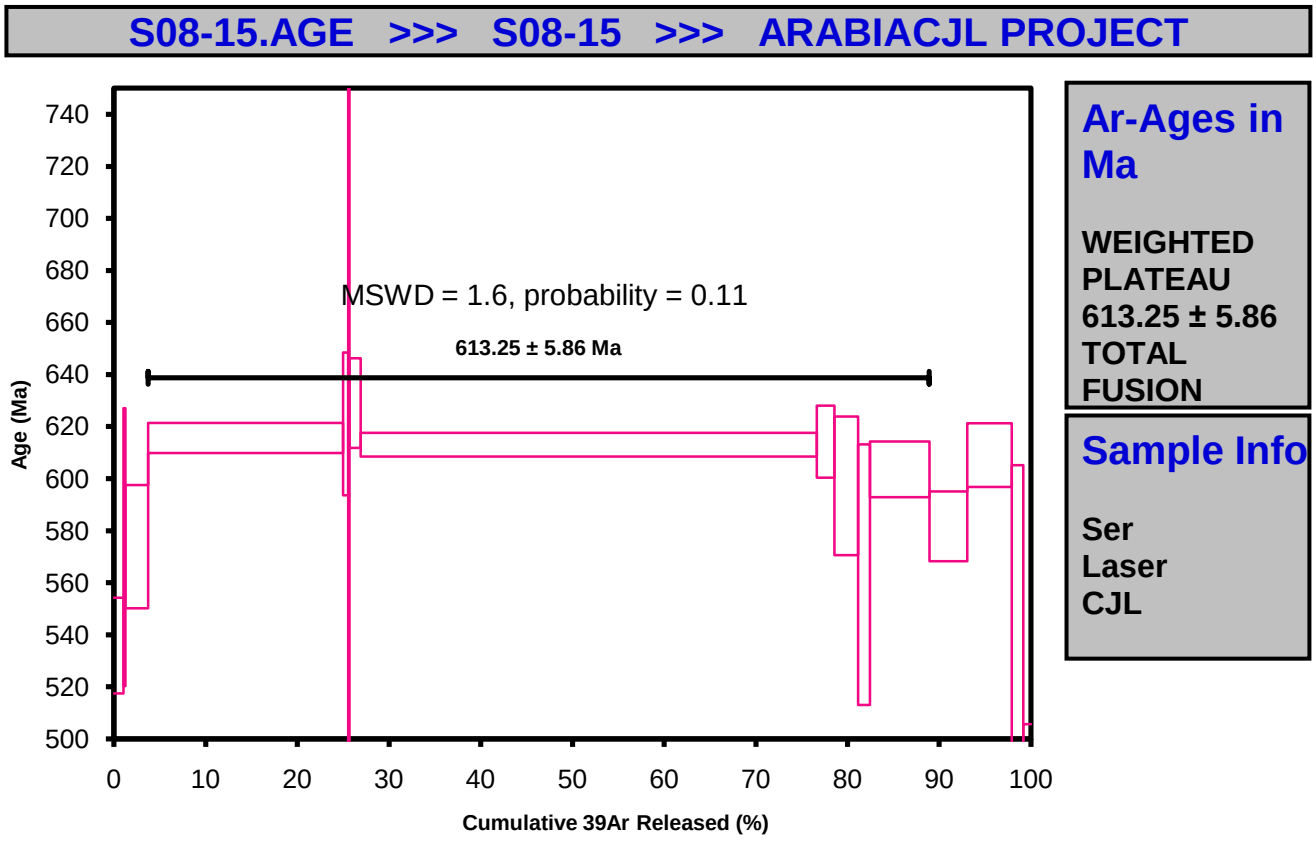

Figure 38

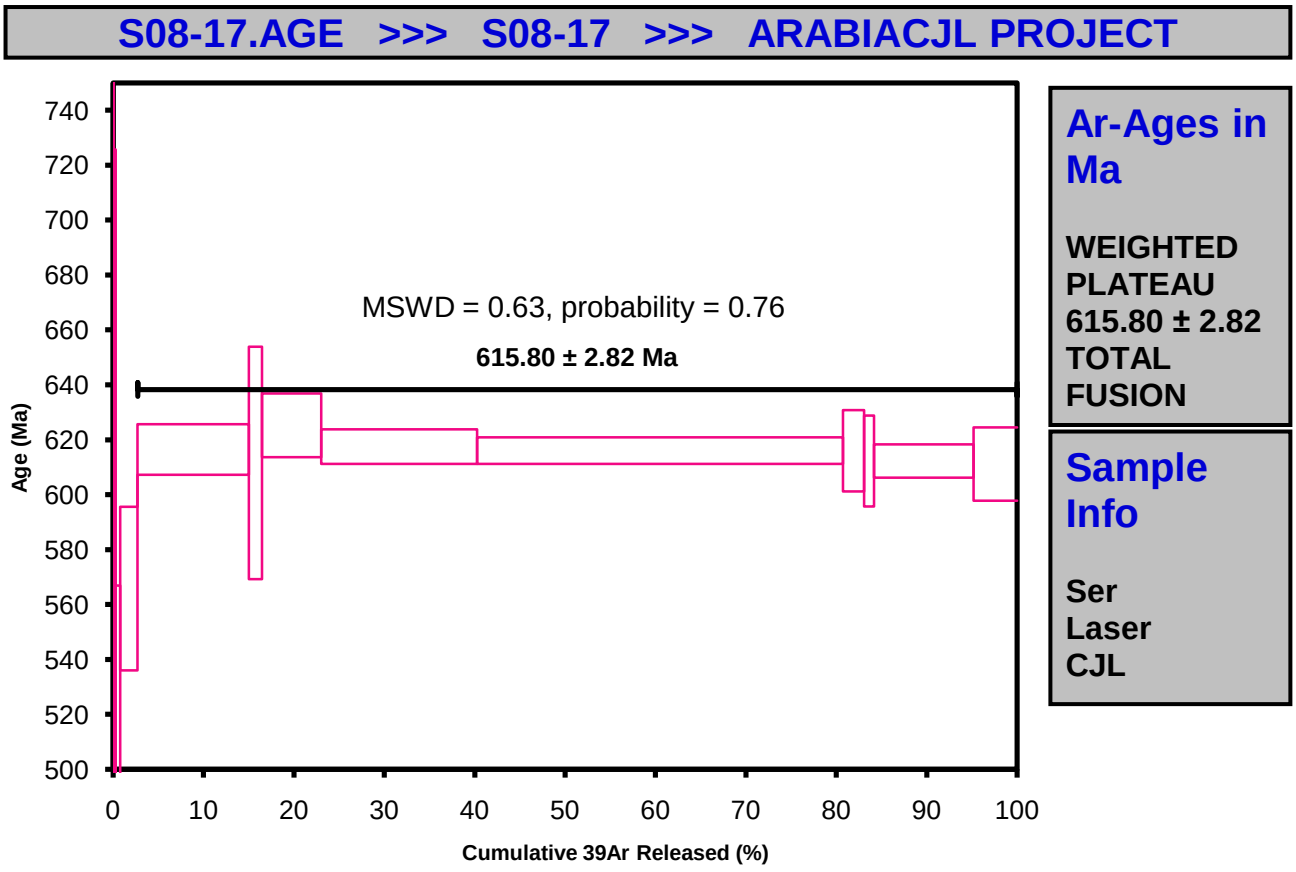

Figure 39

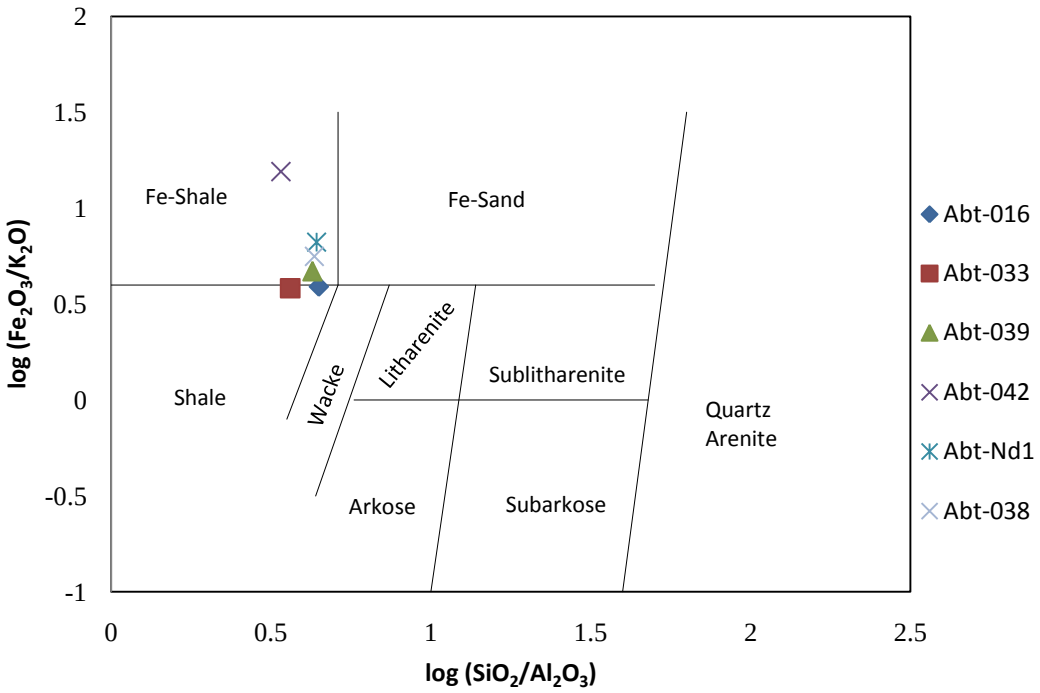

Figure 40

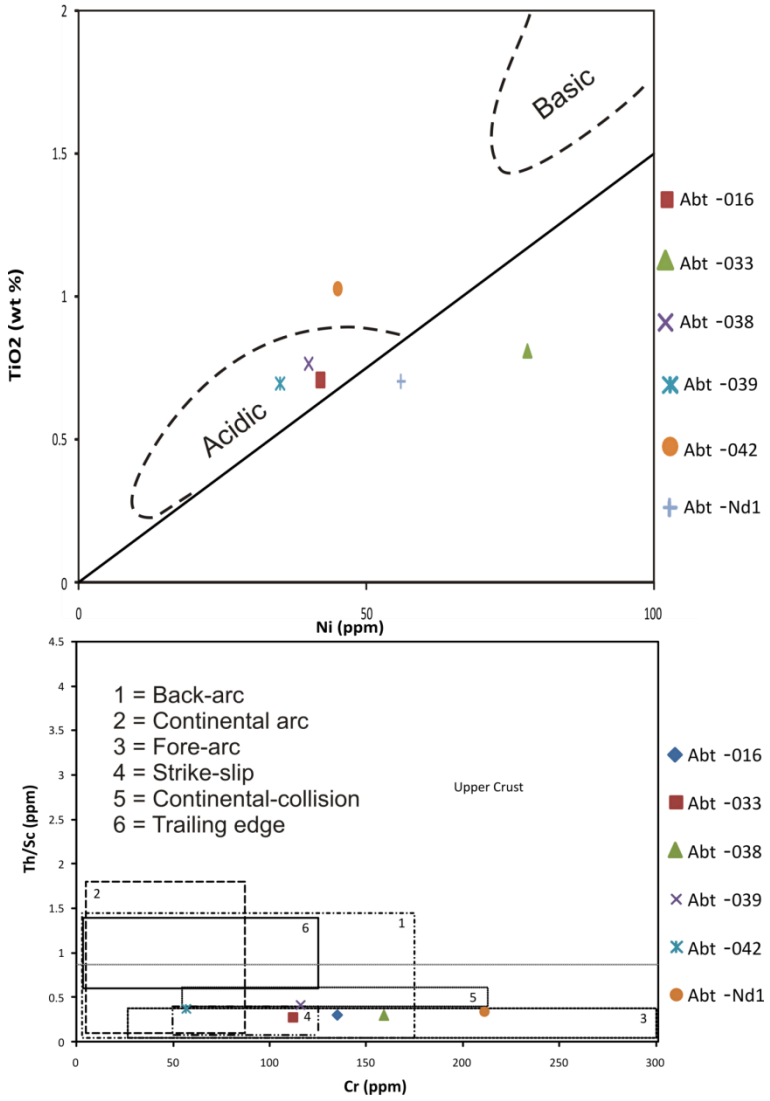

Figure 41

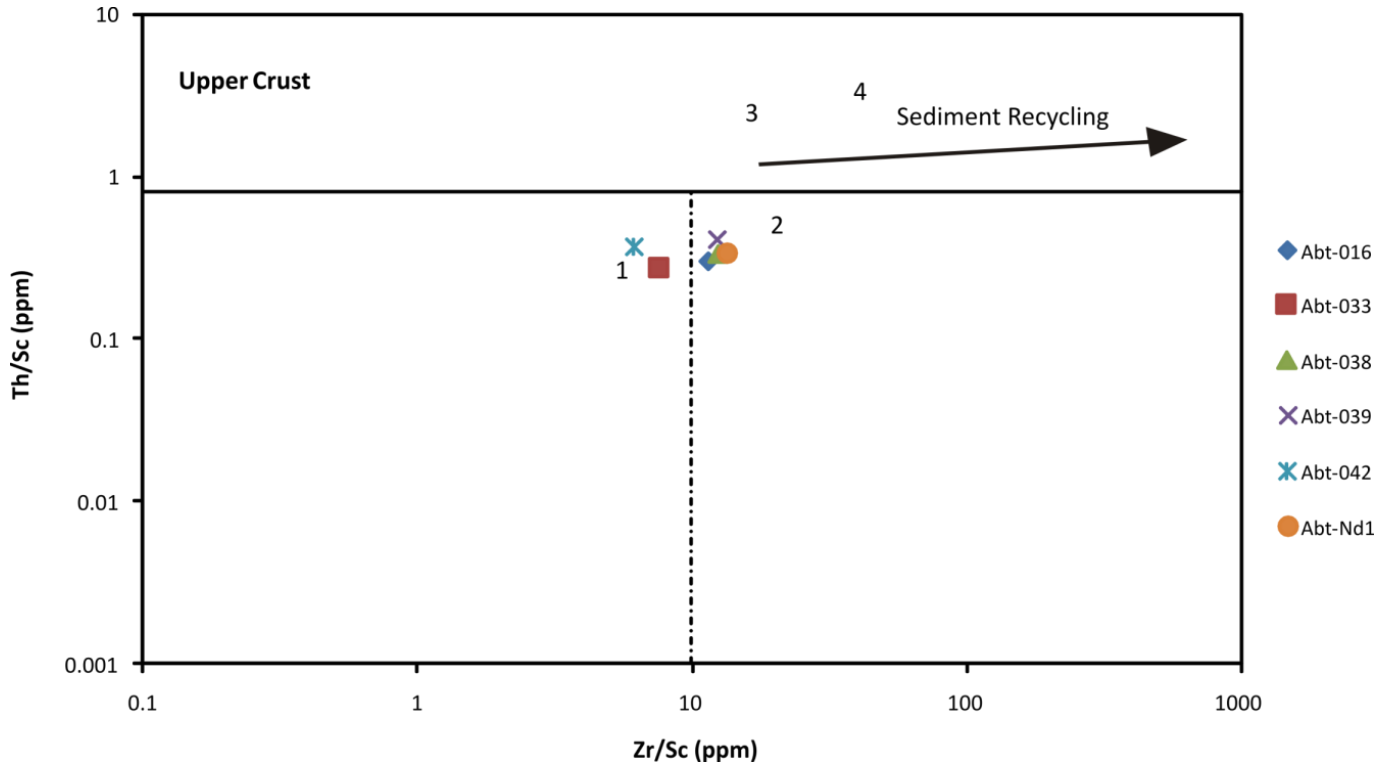
10
1
0.1
0.01
0.001
Th/Sc (ppm)
0.1
1
10
100
1000
Zr/Sc (ppm)
Upper Crust
1
2
3
4
Sediment Recycling
Abt-016
Abt-033
Abt-038
Abt-039
Abt-042
Abt-Nd1

Figure 42

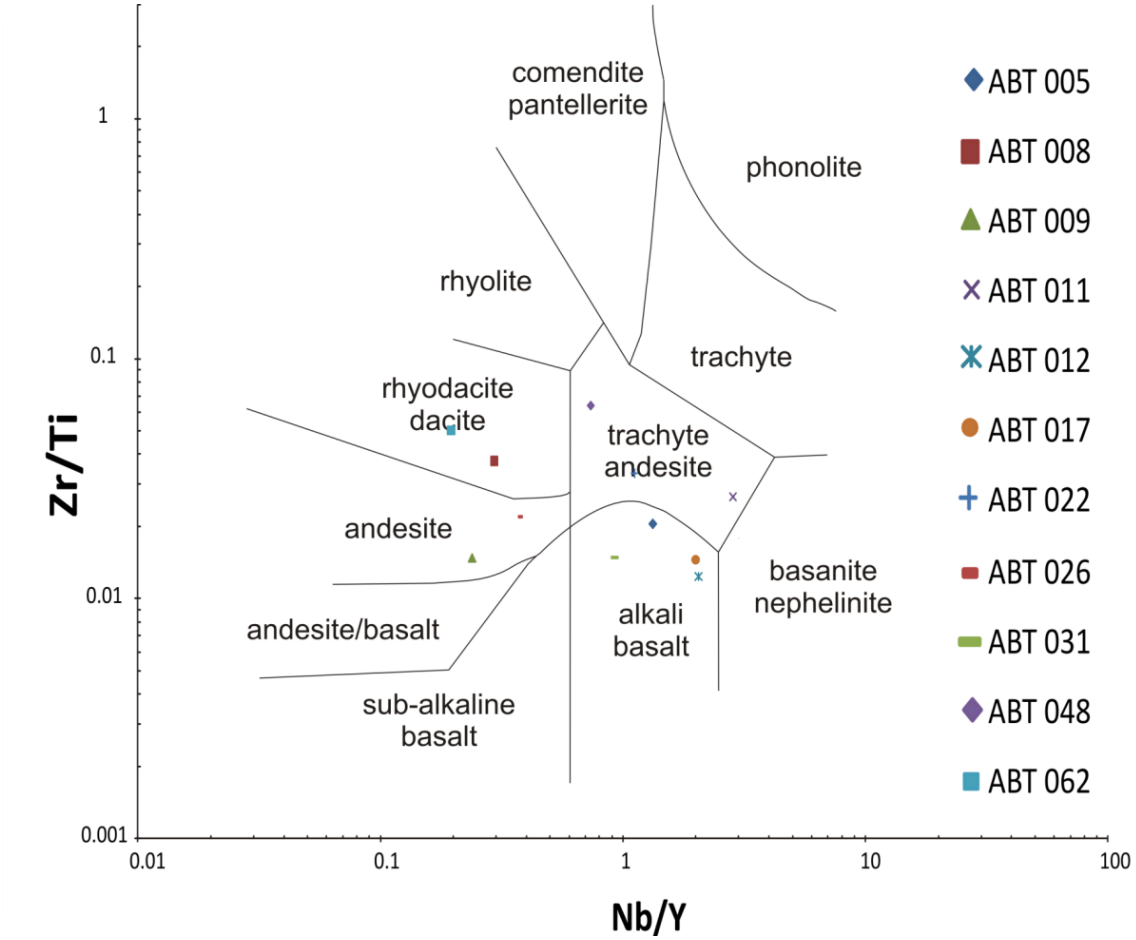

Figure 43

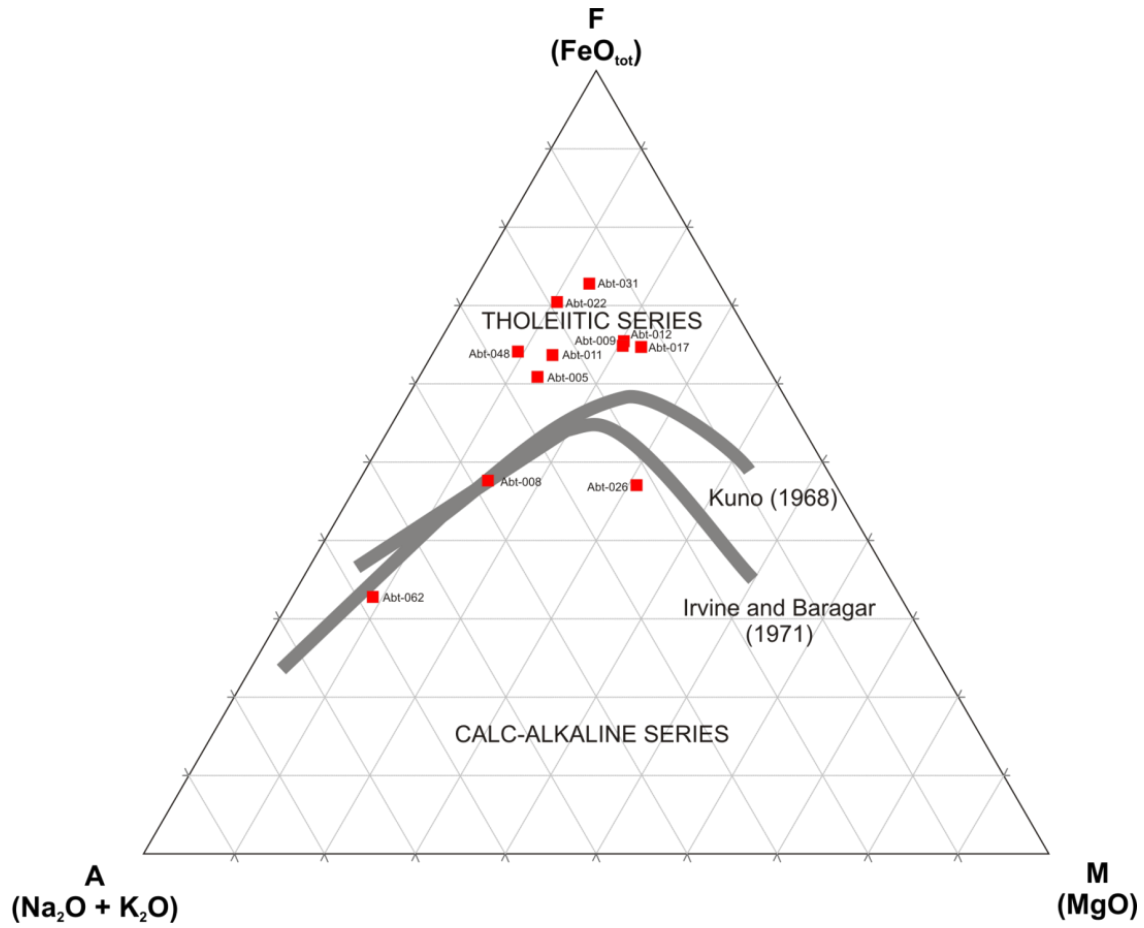

Figure 44

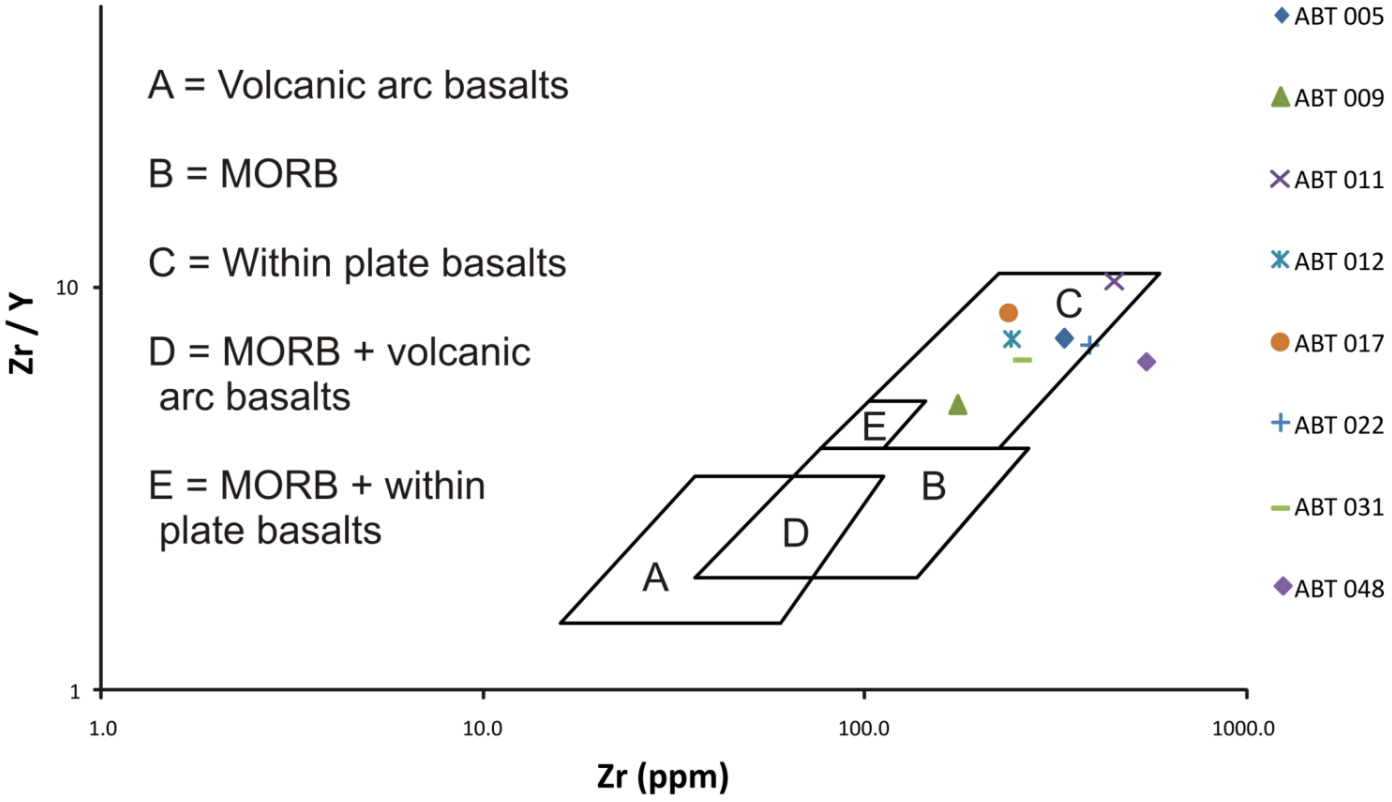

Figure 45

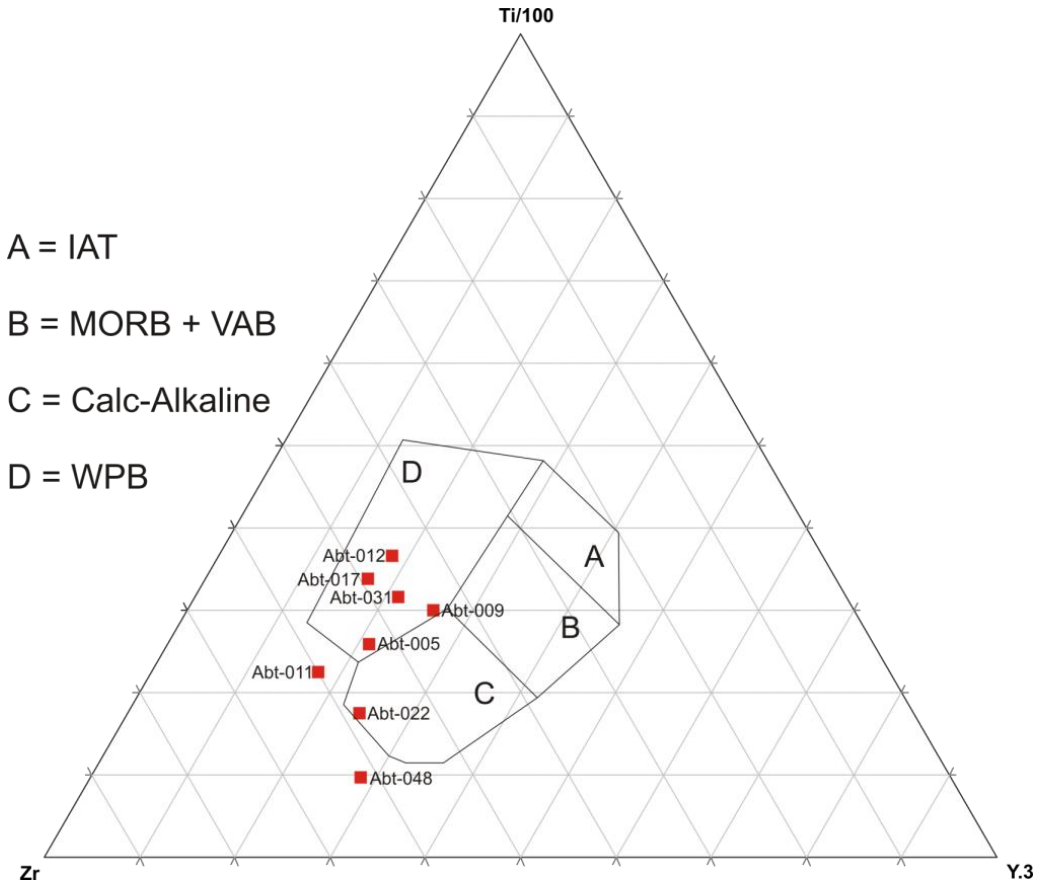

Figure 46

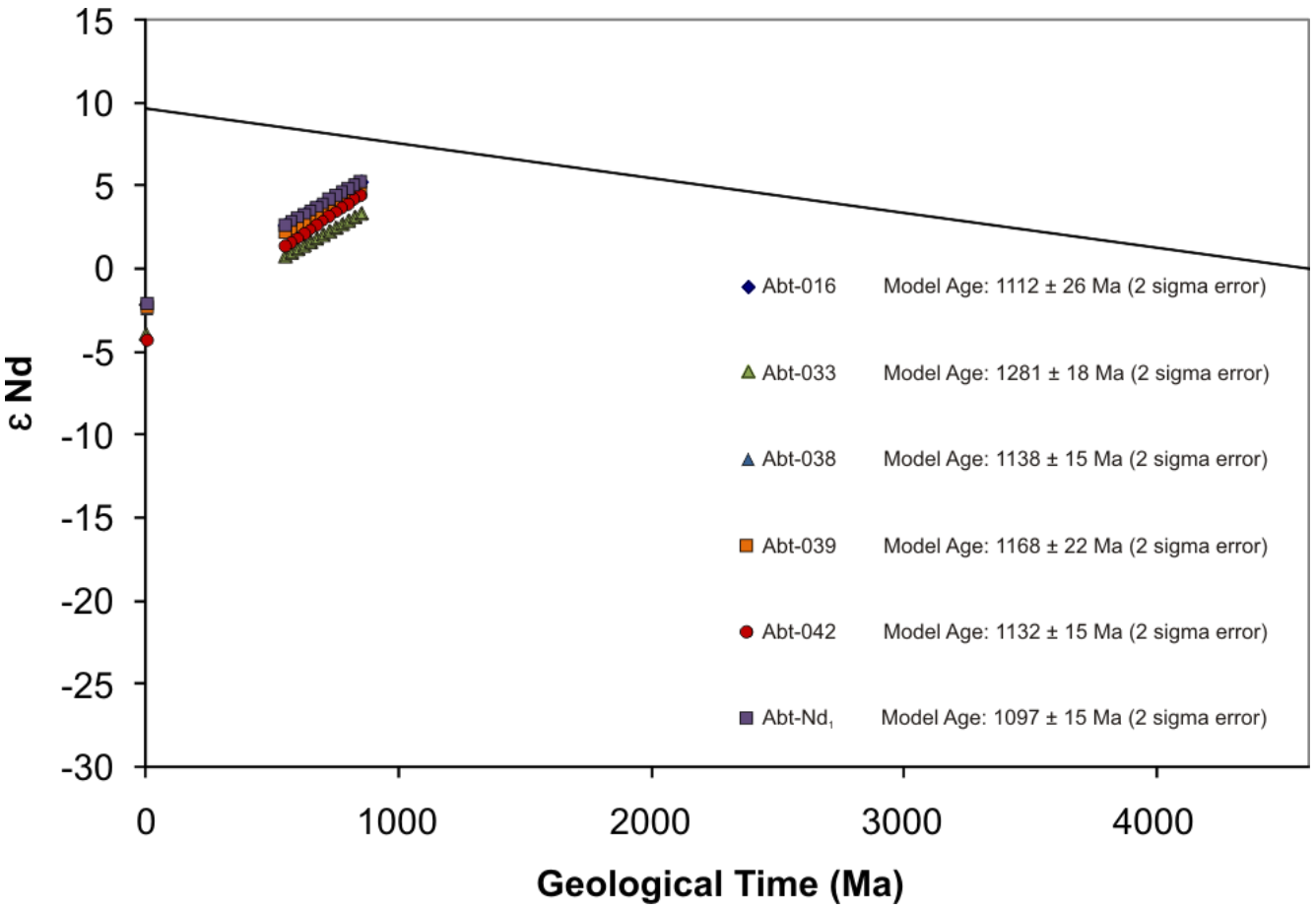

Figure 47

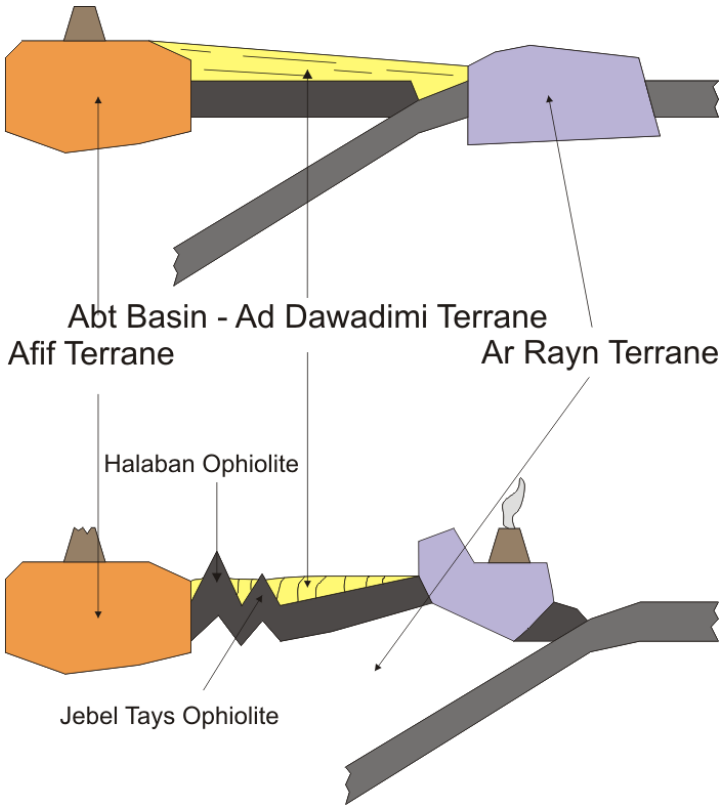

Figure 48

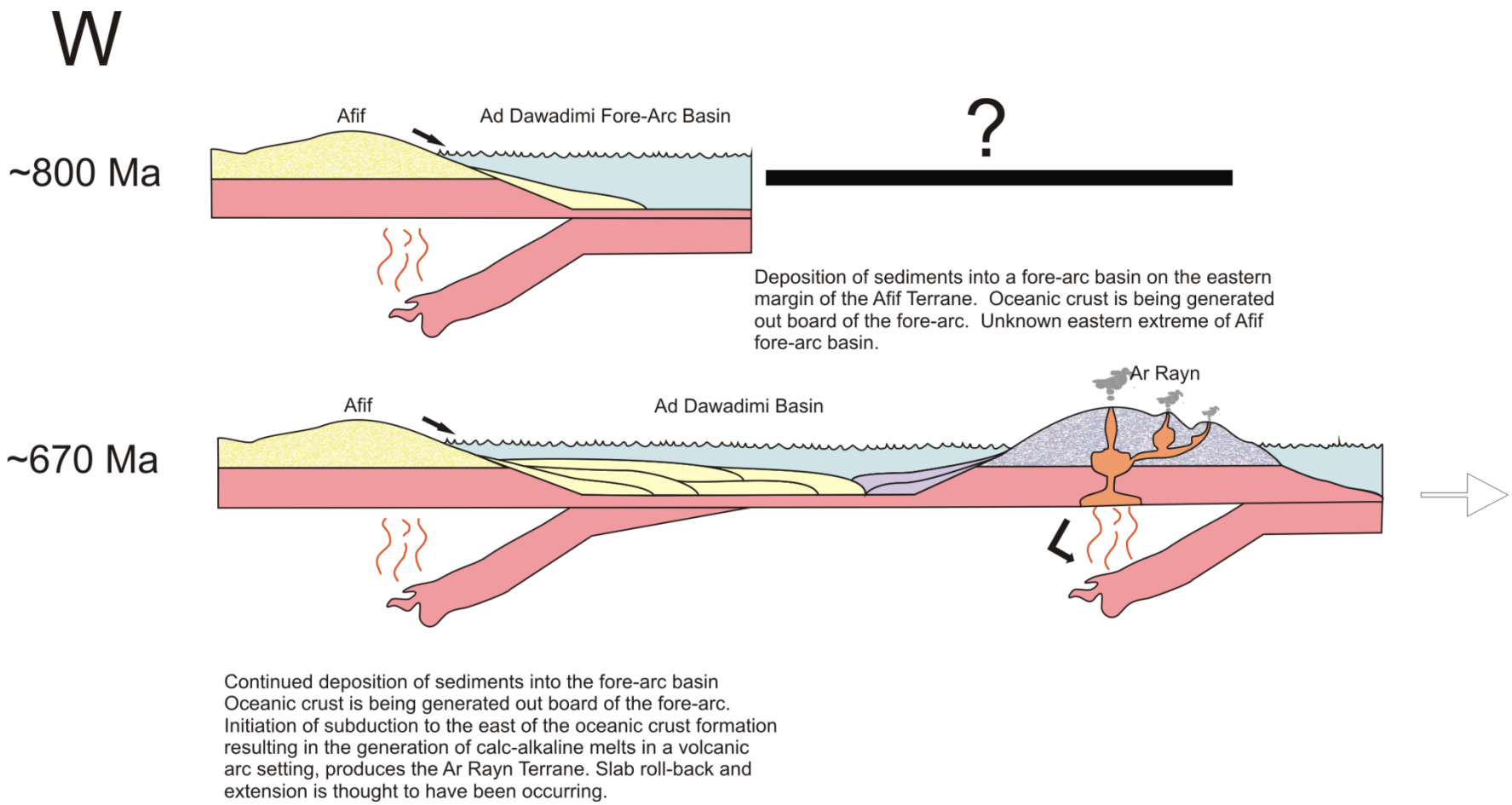
W
E
~800 Ma
Afif
Ad Dawadimi Fore-Arc Basin
?
Deposition of sediments into a fore-arc basin on the eastern margin of the Afif Terrane. Oceanic crust is being generated out board of the fore-arc. Unknown eastern extreme of Afif fore-arc basin.
~670 Ma
Afif
Ad Dawadimi Basin
Ar Rayn
Continued deposition of sediments into the fore-arc basin
Oceanic crust is being generated out board of the fore-arc.
Initiation of subduction to the east of the oceanic crust formation resulting in the generation of calc-alkaline melts in a volcanic arc setting, produces the Ar Rayn Terrane. Slab roll-back and extension is thought to have been occurring.

Figure 49

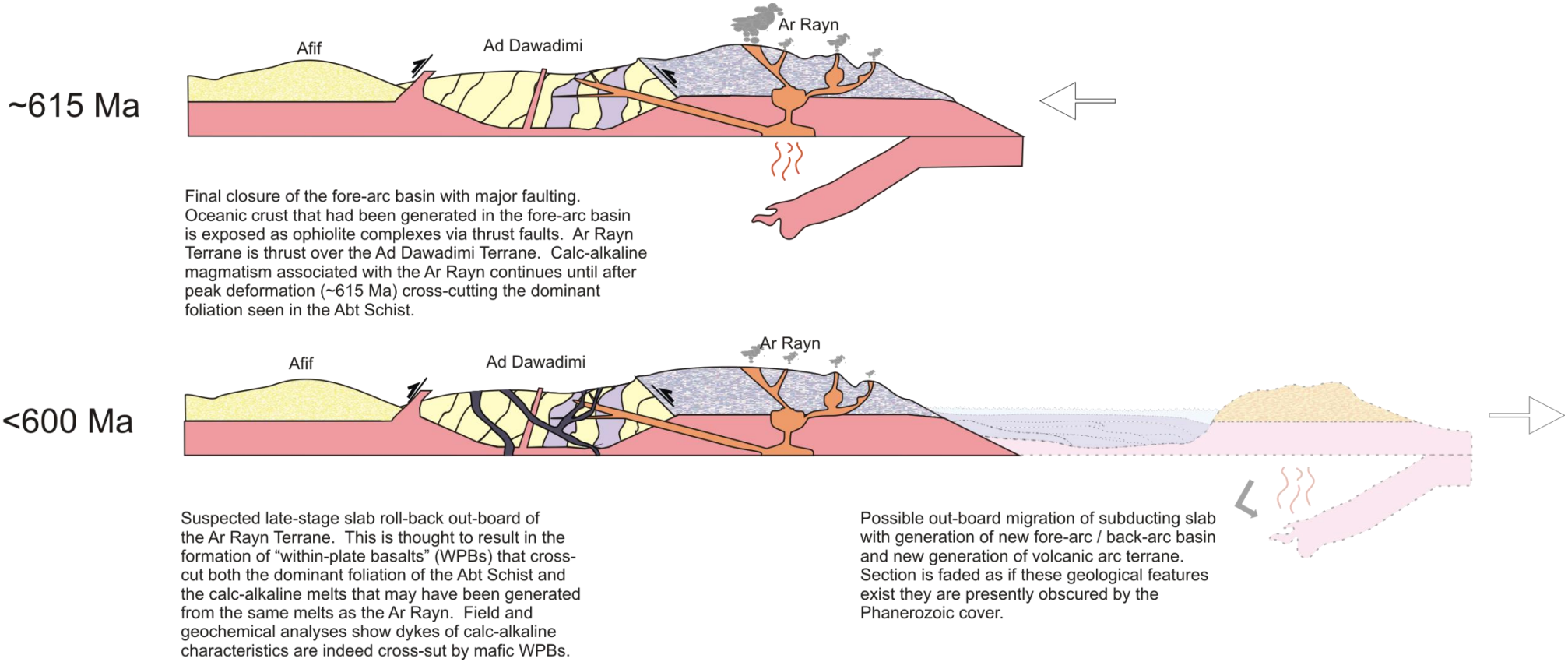
~615 Ma
Afif
Ad Dawadimi
Ar Rayn
Final closure of the fore-arc basin with major faulting. Oceanic crust that had been generated in the fore-arc basin is exposed as ophiolite complexes via thrust faults. Ar Rayn Terrane is thrust over the Ad Dawadimi Terrane. Calc-alkaline magmatism associated with the Ar Rayn continues until after peak deformation (~615 Ma) cross-cutting the dominant foliation seen in the Abt Schist.
<600 Ma
Afif
Ad Dawadimi
Ar Rayn
Suspected late-stage slab roll-back out-board of the Ar Rayn Terrane. This is thought to result in the formation of "within-plate basalts" (WPBs) that cross-cut both the dominant foliation of the Abt Schist and the calc-alkaline melts that may have been generated from the same melts as the Ar Rayn. Field and geochemical analyses show dykes of calc-alkaline characteristics are indeed cross-sut by mafic WPBs.
Possible out-board migration of subducting slab with generation of new fore-arc / back-arc basin and new generation of volcanic arc terrane. Section is faded as if these geological features exist they are presently obscured by the Phanerozoic cover.

Figure 50

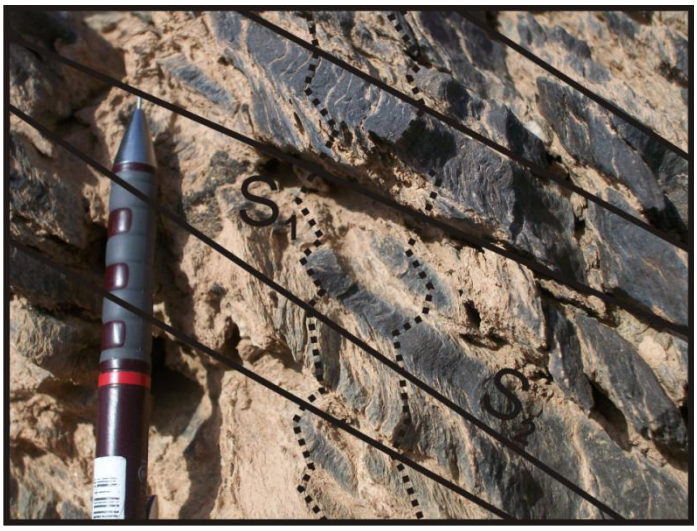

Figure 51

Figure 52

Figure 53

Figure 54

Figure 55

Figure 56

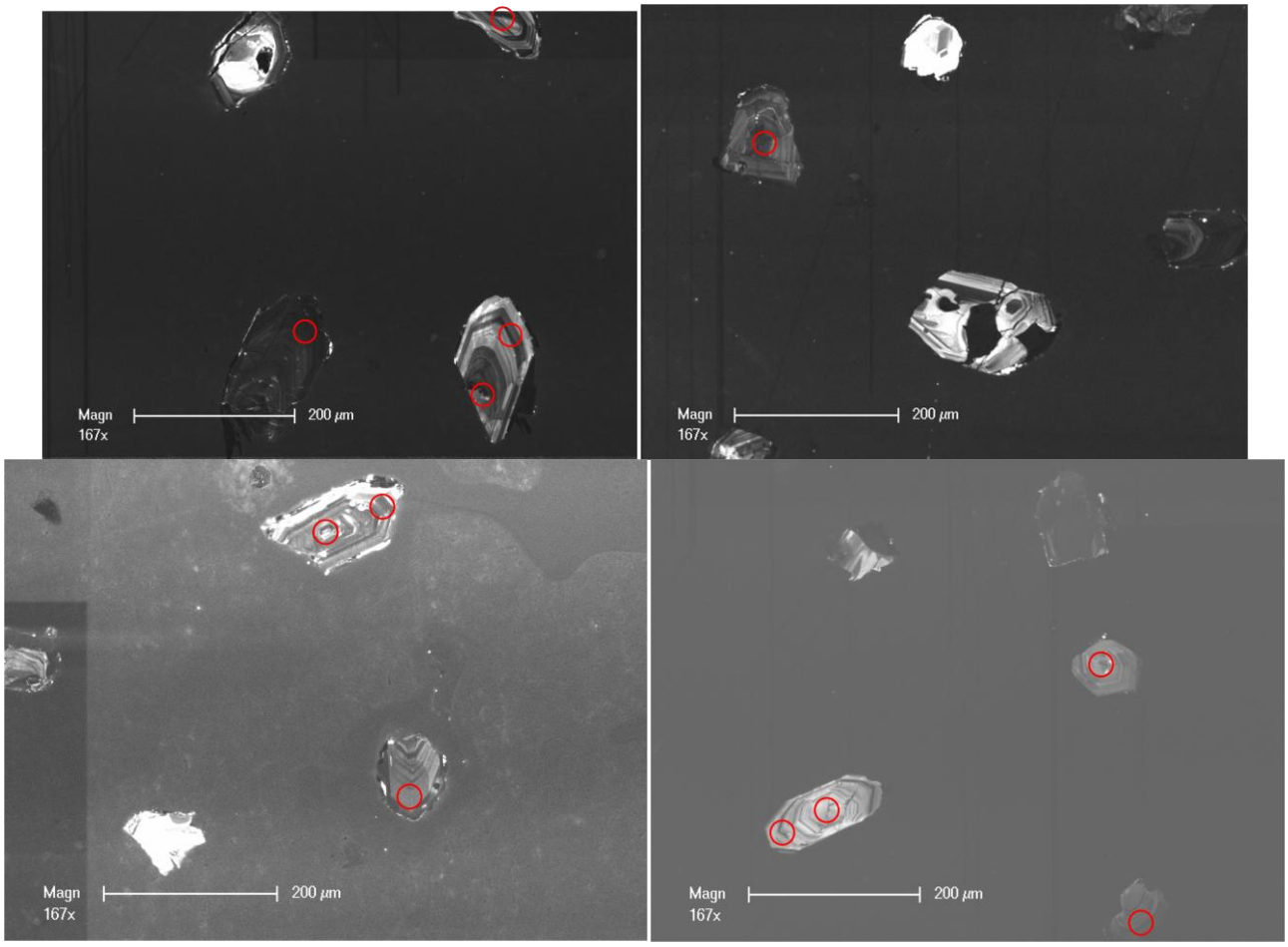

Figure 57

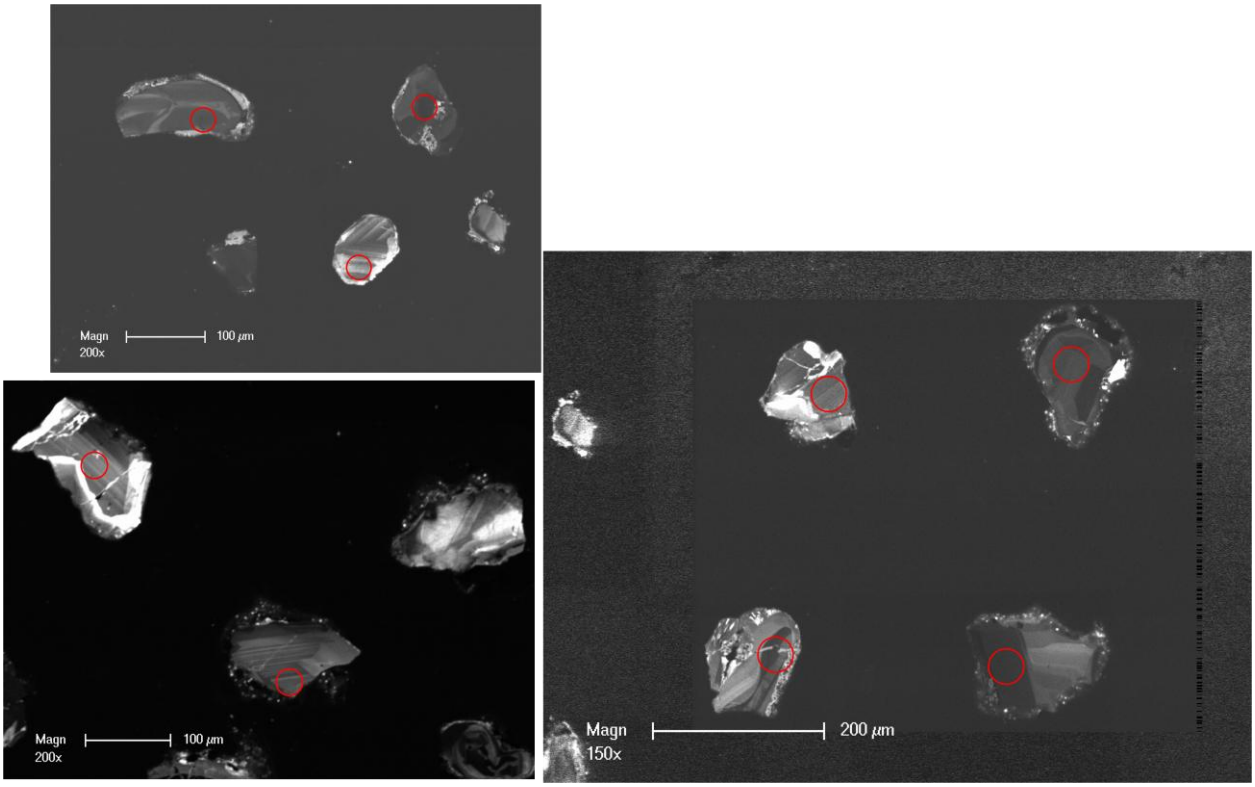

Figure 58

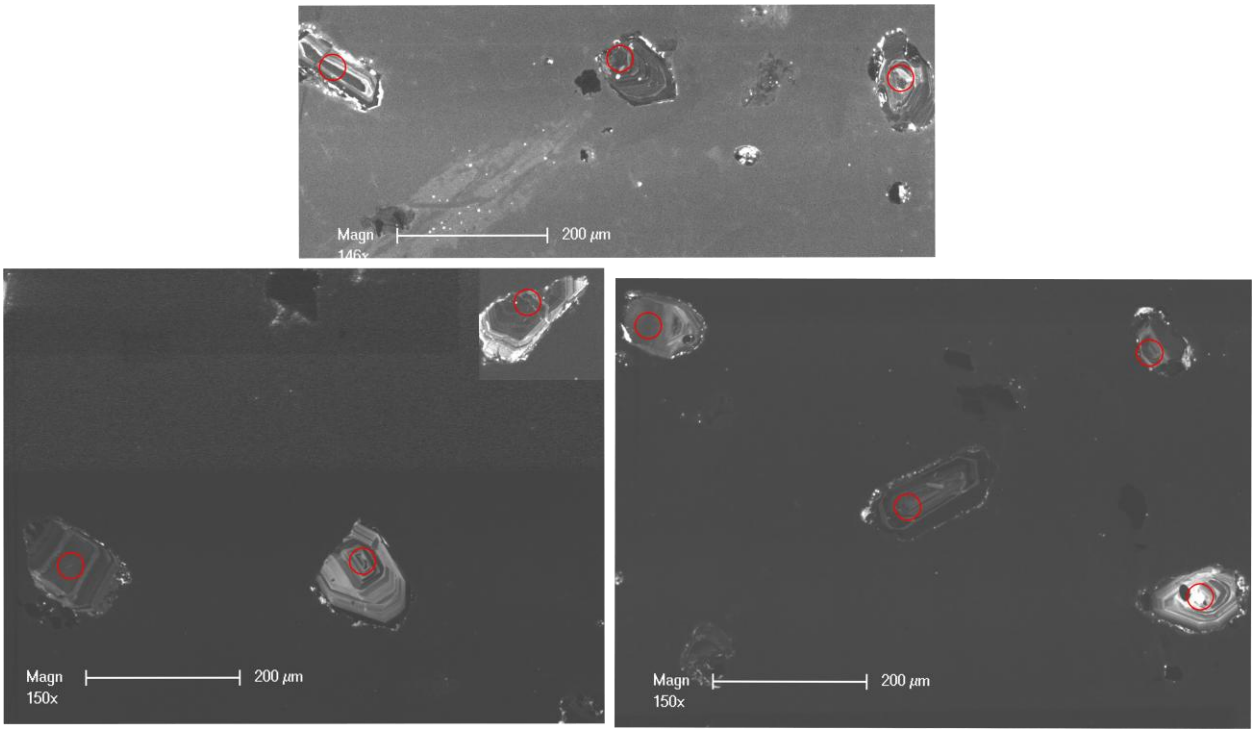

Figure 59

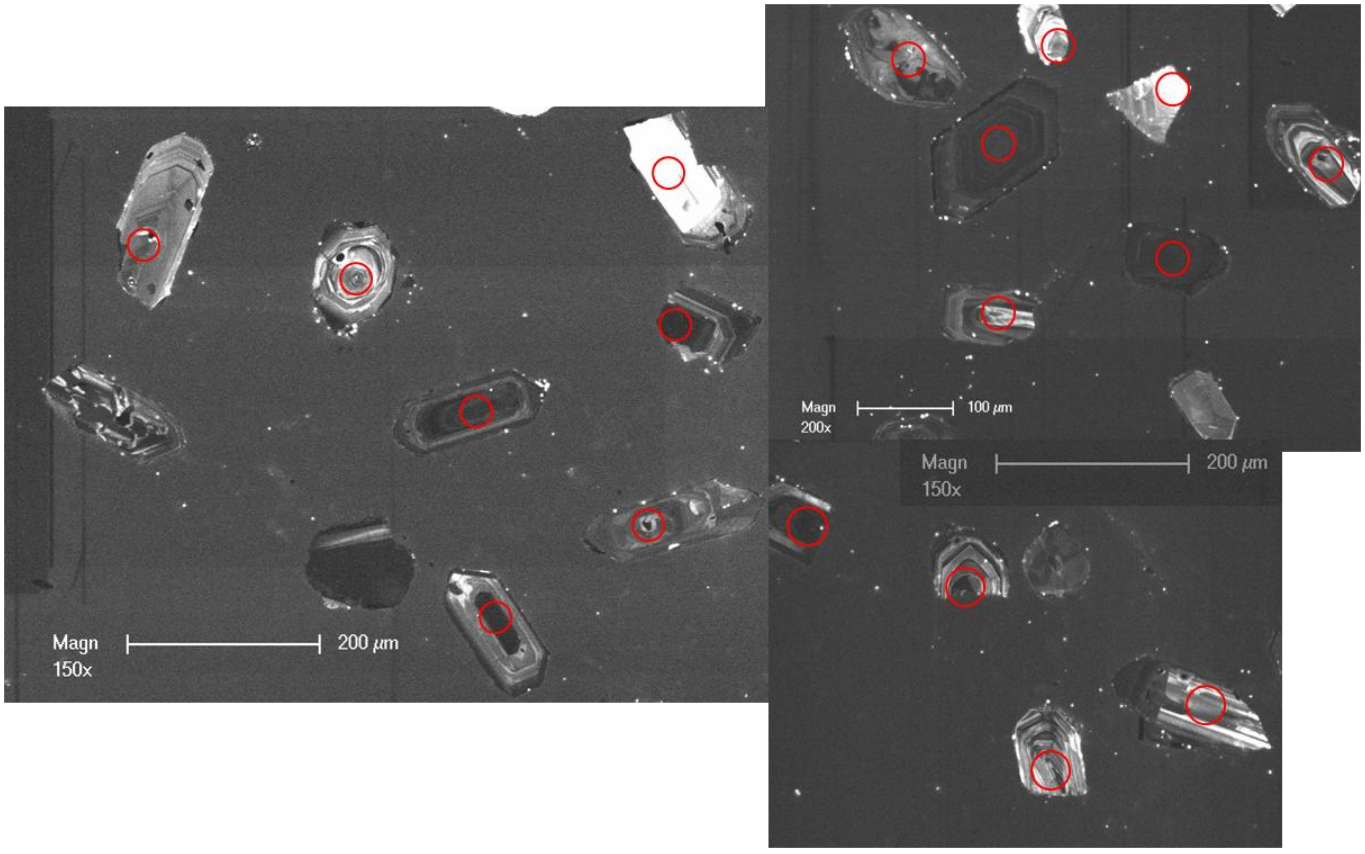

Figure 60

Tables

Table 1: Descriptions of rock samples that have had analyses conducted.

Rock Identification				***Analyses Conducted***				
Sample #	GPS Location	Rock Type	Field Description	U-Pb LA-ICMS	$^{40}Ar/^{39}Ar$	Geochemical Analyses	TIMS	Thin Section
Abt-005	N: 24° 12' 21.3'' E: 44° 09' 29.4''	Mafic Dyke Alkali-Basalt.	Fine grained matrix of olivine with minor pyroxenes and plagioclase hornblende and biotite growth. Glassy inclusions are present within the matrix. Grey/blue colouration.			**X**		**X**
Abt-008	N: 23° 54' 46.0'' E: 44° 45' 31.9''	Felsic-Intermediate Dyke Rhyodacite.	Fine grained matrix of olivine, minor pyroxenes with siliceous mottling. Mottles are ~0.05-0.2 mm. Biotite and muscovite present.			**X**		
Abt-009	N: 23° 54' 46.0'' E: 44° 45' 31.9''	Mafic-Intermediate Dyke Andesite.	Fine grained matrix of olivine with minor pyroxenes. Glassy inclusions are present within the matrix. Grey/blue colouration.			**X**		
Abt-011	N: 23° 55' 22.7'' E: 44° 47' 28.2''	Mafic-Intermediate Trachyte Andesite.	Fine grained olivine matrix. Larger quartz and pyroxene clasts sparsely scattered in matrix. Possibly lithic material incorporated from the host rock. Biotite, muscovite, hornblende and minor tourmaline present.			**X**		
Abt-012	N: 23° 55' 27.2'' E: 44° 47' 35.5''	Mafic Dyke. Alkali-Basalt.	Fine grained olivine and altered plagioclase matrix. Clinopyroxene, large quartz and augite (?) within the matrix with large glassy crystals. Dark grey colouration.			**X**		**X**
Abt-016	N: 23° 55' 27.2'' E: 44° 47' 35.5''	Metasedimentary Sandy-Siltstone.	Silt to clay sized grains, with larger quartz grains throughout. Muscovite, biotite, chlorite rich with minor quartz and			**X**	**X**	

			feldspar. Highly schistose texture.				
Abt-017	N: 23° 55' 51.3'' E: 44° 48' 00.5''	Mafic Dyke. Alkali-Basalt.	Fine grained olivine and altered plagioclase matrix. Clinopyroxene, large quartz and augite (?) within the matrix with large glassy crystals. Dark grey colouration.			X	
Abt-022	N: 23° 56' 17.3'' E: 44° 50' 09.3''	Mafic-Intermediate Dyke Trachyte Andesite.	Fine grained matrix dominated by olivine and highly altered plagioclase. Quartz and augite (?) clasts are rimmed by hornblende and biotite.			X	X
Abt-025	N: 23° 56' 17.3'' E: 44° 50' 09.3''	Metasedimentary Siltstone.	Muscovite and chlorite rich, biotite in lesser abundance. Moderately rich in quartz (~0.25 mm) and feldspars.	X			
Abt-026	N: 23° 56' 17.3'' E: 44° 50' 09.3''	Mafic-Intermediate Dyke Andesite.	Fine grained matrix of olivine with minor pyroxenes. Glassy inclusions are present within the matrix. Grey/blue colouration.			X	
Abt-031	N: 23° 56' 49.9'' E: 44° 52' 00.1''	Mafic Dyke Alkali-Basalt.	Fine grained olivine matrix. Black/brown glassy clasts. Quartz, pyroxene (augite?) present within matrix showing, hornblende biotite rims.			X	
Abt-033	N: 23° 57' 32.8'' E: 44° 52' 47.4''	Metasedimentary Shale.	Very fine grained dark grey – black claystone. Muscovite and biotite are present.			X	X
Abt-038	N: 23° 57' 47.0'' E: 44° 53' 51.7''	Metasedimentary Sandy-Siltstone.	Silt to clay sized grains, with larger quartz grains throughout. Muscovite, biotite, chlorite rich with minor quartz and feldspar. Highly schistose texture.			X	X

Abt-039	N: 23° 57’ 47.0’’ E: 44° 53’ 51.7’’	Metasedimentary Siltstone.	Silt to clay sized grains, with larger quartz grains throughout. Muscovite, biotite, chlorite, feldspar rich with minor quartz. Highly schistose texture.			**X**	**X**	
Abt-042	N: 23° 58’ 28.5’’ E: 44° 54’ 54.1’’	Metasedimentary Sandy-Siltstone.	Highly convoluted structure. Silt to clay sized grains. Muscovite, biotite chlorite rich with minor quartz and feldspar. Biotite exists in nodular pods within the schistose structure as well as in the major foliation.	**X**		**X**	**X**	
Abt-048	N: 23° 59’ 20.2’’ E: 44° 55’ 57.6’’	Mafic-Intermediate Dyke. Trachyte Andesite.	Light red/purple fresh surface colouration. Fine grained. Limited larger clasts. Silica rich altered plagioclase (limited olivine and pyroxene) matrix may have inclusions from the host rock.			**X**		**X**
Abt-057	N: 24° 12’ 21.3’’ E: 44° 09’ 29.4’’	Metasedimentary Sandstone.	Coarse quartz and andalusite grains. Very rich in muscovite, andalusite and chlorite. Andalusite grains (<0.5-1 mm) overprints the muscovite, biotite, chlorite schistose texture.	**X**				
Abt-062	N: 24° 12’ 21.3’’ E: 44° 09’ 29.4’’	Felsic-Intermediate Dyke Rhyodacite..	Silica rich dyke. High in quartz (<0.5-2 mm) and feldspar. Light green coloured fresh surface with quartz. Larger purple coloured crystals within matrix from the host rock (Ar Rayn Terrane?). No glass. Brecciated?			**X**		**X**

Abt-Nd_1	N: 23° 57' 47.0'' E: 44° 53' 51.7''	Metasedimentary Siltstone.	Silt to clay sized grains, with small quartz grains throughout. Muscovite, biotite, chlorite rich with minor quartz and feldspar. Highly schistose texture.				**X**	**X**
Abt-Z_1	N: 23° 56' 14.5'' E: 44° 50' 15.2''	Metasedimentary Siltstone.	Silt to clay sized grains, with larger quartz grains throughout. Muscovite, biotite, chlorite rich with minor quartz and feldspar. Highly schistose texture.	**X**				**X**
S08-015	N: 23° 54' 51.8'' E: 44° 43' 32.3''	Metasedimentary Siltstone.	Biotite, muscovite, chlorite rich with minor quartz and feldspar. Highly schistose. Weathering exploitation of schistose texture.		**X**			
S08-017	N: 23° 56' 58.3'' E: 44° 32' 16.0''	Metasedimentary Siltstone	Biotite, muscovite, chlorite rich with minor quartz and feldspar. Highly schistose. Weathering exploitation of schistose texture.		**X**			

Table 2: LA-ICPMS data for Abt-025; $^{206}Pb/^{238}U$ zircon analysis. Age error is displayed at 1σ.

Abt-025	Isotopic Ratios					Ages					
Analysis_#	Pb207/U235	1σ error	Pb206/U238	1σ error	rho	Pb207/Pb206 Age (Ma)	± Ma	Pb206/U238 Age (Ma)	± Ma	Conc. %	Rim/Core
1	0.97595	0.0163	0.10306	0.00135	0.784302491	888.9	32.1	632.3	7.88	71	c
2	1.06674	0.0184	0.10586	0.00141	0.772196769	1016.2	32.65	648.7	8.24	64	r
3	0.976	0.01798	0.10642	0.00143	0.729412016	822.6	36.34	651.9	8.35	79	r
4	0.95812	0.01597	0.10555	0.0014	0.795764916	801.6	31.95	646.9	8.19	81	c
6	1.08668	0.01907	0.10033	0.00139	0.789468796	1162.1	32.09	616.3	8.12	53	r
7	1.05703	0.01685	0.10996	0.00146	0.832924301	921	29.4	672.5	8.5	73	c
10	1.03513	0.02231	0.11227	0.00161	0.66536121	834.4	43.31	685.9	9.35	82	r
21	0.95807	0.01611	0.10818	0.00148	0.813610302	749	31.66	662.1	8.61	88	r
22	0.91494	0.01537	0.10248	0.00138	0.801601861	765.9	31.97	628.9	8.09	82	c
23	1.17847	0.02373	0.10748	0.00155	0.716184361	1185.1	38.02	658.1	9	56	r
24	2.20071	0.03783	0.1106	0.00165	0.867871232	2280	27.04	676.2	9.55	30	r
25	0.99128	0.01936	0.11104	0.00156	0.71934319	766.1	38.7	678.8	9.03	89	c
26	0.88833	0.01524	0.102	0.00139	0.794335533	713.7	33.02	626.1	8.12	88	c
27	1.27587	0.01823	0.10806	0.00145	0.93912369	1329.9	22.93	661.5	8.44	50	c
28	1.03515	0.01689	0.11622	0.00158	0.833201135	761.2	30.39	708.8	9.13	93	c
29	0.82824	0.01275	0.09599	0.00128	0.866223565	693.9	28.42	590.9	7.55	85	r
30	0.93025	0.01204	0.1101	0.00144	0.989581654	649.2	21.38	673.3	8.38	104	c
31	1.21229	0.02091	0.12538	0.00173	0.799963787	932.8	31.95	761.5	9.91	94	c
32	1.01831	0.02158	0.11485	0.00165	0.677924786	751.8	42.67	700.8	9.51	98	r
33	0.98438	0.02038	0.10576	0.00154	0.703327956	853.9	40.6	648.1	8.95	93	r
34	1.14716	0.02352	0.10501	0.00161	0.747793861	1177.5	37.87	643.7	9.39	83	c
35	1.03302	0.02367	0.1108	0.00166	0.653851011	857.3	45.7	677.4	9.65	94	r
36	0.84046	0.01453	0.08919	0.00125	0.810672206	879.2	31.74	550.7	7.4	89	c
37	0.95623	0.02077	0.10556	0.00153	0.667295072	796.9	43.73	646.9	8.91	95	c
38	1.03395	0.01711	0.11182	0.00151	0.81603162	839.8	30.96	683.3	8.77	95	r
39	1.21827	0.02235	0.11977	0.00162	0.737280907	1035	35.3	729.2	9.34	90	c
40	0.84716	0.01325	0.09855	0.00132	0.85638069	686.3	29.24	605.9	7.74	97	c
41	1.17085	0.02142	0.10715	0.00157	0.800920244	1178.9	32.74	656.2	9.12	83	r
42	0.95366	0.01738	0.10706	0.00146	0.748289087	762	35.76	655.7	8.49	96	c
43	0.90494	0.01582	0.10037	0.00138	0.786481422	787.7	33.31	616.6	8.07	94	c
44	1.03135	0.02866	0.09478	0.00155	0.58849785	1170.5	54.81	583.8	9.15	81	c
45	1.38331	0.04287	0.1169	0.00204	0.563095024	1334.7	60.71	712.7	11.76	81	r
46	1.0668	0.02694	0.10909	0.00165	0.598941517	955.8	51.08	667.5	9.61	91	r
47	1.20761	0.03186	0.09757	0.00168	0.652640328	1421.3	50.05	600.1	9.86	75	r
48	0.95135	0.02639	0.10493	0.00169	0.580614616	799.3	57.1	643.2	9.85	95	c
49	0.93458	0.02243	0.10516	0.00157	0.622065741	757.1	49.13	644.6	9.16	96	c
50	1.12448	0.02367	0.11067	0.00159	0.682528345	1033.3	40.89	676.7	9.21	88	r
51	0.90295	0.01478	0.09936	0.00133	0.81776652	803.8	30.82	610.7	7.81	93	r
52	0.91885	0.01436	0.09968	0.00135	0.866594481	833.5	28.27	612.6	7.89	93	r
53	0.90086	0.01499	0.10317	0.00139	0.809686765	719.5	31.78	633	8.12	97	c
54	0.98841	0.02471	0.10426	0.00161	0.617692802	891.7	50.45	639.3	9.4	92	r
55	1.01786	0.01876	0.09865	0.00137	0.753492079	1064.2	34.73	606.5	8.05	85	r
56	1.88374	0.04095	0.11212	0.00175	0.717995981	1983.7	38.8	685.1	10.13	64	c
58	1.24197	0.02992	0.12922	0.00199	0.639253119	919.8	48.01	783.4	11.37	96	c
59	1.10147	0.02227	0.11862	0.0017	0.708832232	848.4	39.58	722.6	9.82	96	c

60	2.23377	0.03086	0.10841	0.00144	0.961469872	2339.6	20.02	663.5	8.35	56	c
61	1.26868	0.03168	0.0985	0.00157	0.638308081	1496.7	47.28	605.6	9.2	73	c
62	0.9979	0.02768	0.09874	0.00163	0.595134899	1024.1	55.2	607	9.56	86	r
63	1.00566	0.02097	0.10341	0.0015	0.695635067	945.2	40.63	634.3	8.75	90	c
64	0.97774	0.01787	0.1073	0.00147	0.749577329	809.5	35.61	657	8.55	95	c
65	0.91857	0.01391	0.10495	0.00142	0.893492742	725.4	26.9	643.4	8.28	97	r
66	1.02357	0.01603	0.10467	0.00142	0.866263761	956.4	27.62	641.7	8.3	90	r
67	1.19361	0.04764	0.1119	0.00224	0.501543525	1130.8	80.78	683.8	13.01	86	r
68	0.99621	0.02758	0.11104	0.00176	0.572518928	777	57.39	678.8	10.23	97	r
70	0.90023	0.01726	0.10255	0.00145	0.737471137	731.7	37.44	629.3	8.5	97	r

Table 3: LA-ICPMS data for Abt-042; $^{206}Pb/^{238}U$ zircon analysis. Age error is displayed at 1σ.

Abt-042	Isotopic Ratios					Ages					
Analysis_#	Pb207/U235	1σ error	Pb206/U238	1σ error	rho	Pb207/Pb206 Age (Ma)	± Ma	Pb206/U238 Age (Ma)	± Ma	Conc. %	Rim/Core
1	1.05717	0.04056	0.1089	0.00188	0.449963	940.4	76.45	666	11	91	u
2	0.96939	0.03162	0.10761	0.00167	0.475774	784.8	66.35	659	10	96	u
3	1.95782	0.19706	0.11568	0.00446	0.383046	1997.5	176.49	706	26	64	r
4	0.94202	0.03744	0.10502	0.00173	0.414475	775.5	81.7	644	10	96	c
5	0.9214	0.01661	0.10848	0.00149	0.76193	659.9	34.13	664	9	100	c
6	1.00493	0.01971	0.10562	0.00147	0.709611	898.6	36.73	647	9	92	r
7	1.0576	0.03036	0.10961	0.00168	0.533923	927.9	56.38	671	10	92	r
8	0.92675	0.02724	0.11231	0.00165	0.499828	597.9	61.3	686	10	103	u
9	1.04951	0.04711	0.10797	0.0019	0.392034	942.7	90.35	661	11	91	u
10	1.1273	0.07226	0.11009	0.00245	0.347184	1048	126.54	673	14	88	r
11	1.10155	0.04197	0.10508	0.00175	0.437102	1095.9	74.9	644	10	85	c
12	1.07753	0.03537	0.10635	0.00173	0.495568	1028.2	64.26	652	10	88	u
13	1.14847	0.02527	0.10747	0.00152	0.642792	1134.2	41.01	658	9	85	c
14	1.0731	0.02837	0.10799	0.00158	0.553419	987.9	51.77	661	9	89	u
15	1.1684	0.05862	0.10892	0.00206	0.376969	1142	98.34	667	12	85	r
16	1.09759	0.03482	0.10878	0.0017	0.492619	1019.1	62.38	666	10	88	r
17	0.93387	0.01693	0.10683	0.00147	0.759021	721.8	34.08	654	9	98	c
18	1.06128	0.04243	0.10729	0.00181	0.421965	979	79.6	657	11	89	c
19	1.21967	0.06453	0.11147	0.00219	0.371336	1181.3	102.98	681	13	84	r
20	1.06875	0.07032	0.10481	0.00231	0.33497	1040.6	130.04	643	14	87	u
21	0.97296	0.08215	0.1022	0.00264	0.305943	900.5	169.29	627	15	91	r
22	0.98847	0.04794	0.10321	0.00185	0.369586	912.9	98.36	633	11	91	r
23	1.00477	0.05701	0.10484	0.00204	0.34294	914.2	114.8	643	12	91	r
24	0.95103	0.04824	0.10526	0.0019	0.355858	791.7	104.66	645	11	95	r
25	0.89657	0.04383	0.1033	0.00181	0.358419	706.8	102.15	634	11	98	u
26	1.04477	0.03041	0.10629	0.00161	0.520401	966	57.55	651	9	90	r
27	0.90881	0.02776	0.10398	0.00154	0.484869	721.5	62.99	638	9	97	c
28	0.98765	0.03752	0.1023	0.00164	0.421996	929.2	76.82	628	10	90	c
29	1.09224	0.10326	0.10492	0.00303	0.305471	1082.6	183.75	643	18	86	r
30	1.79413	0.07575	0.10102	0.00197	0.461881	2082	75.34	620	12	59	r
31	1.01293	0.07448	0.10154	0.00243	0.325468	996.3	146.05	623	14	88	r
32	0.85843	0.02335	0.10197	0.00146	0.526379	641.2	56.26	626	9	99	c
33	0.97575	0.04164	0.10476	0.00178	0.398155	854.7	87.09	642	10	93	u
34	1.88665	0.12053	0.11365	0.00292	0.40217	1962.6	114.91	694	17	64	u
35	0.90766	0.04661	0.10029	0.00184	0.357276	794.8	105.72	616	11	94	r
36	0.83329	0.03101	0.09887	0.00156	0.423989	643.6	78.09	608	9	99	u
37	0.95801	0.02484	0.10945	0.00155	0.546178	724.4	52.82	670	9	98	u
38	1.2648	0.02366	0.10997	0.00151	0.734023	1279.1	33.36	673	9	81	c
39	1.51689	0.38056	0.1141	0.0088	0.307417	1557.5	424.86	697	51	74	r
40	0.94918	0.02986	0.10783	0.00163	0.480515	736.5	64.66	660	9	97	u
41	0.94323	0.06733	0.10671	0.00241	0.316389	745.6	146.96	654	14	97	c
42	0.89705	0.01793	0.10589	0.00145	0.685093	654.3	39.37	649	8	100	r
43	0.91748	0.01947	0.10729	0.00148	0.65003	674.5	42.09	657	9	99	r
44	0.94382	0.03375	0.10639	0.00167	0.438966	752.4	73.7	652	10	97	u
45	1.1619	0.08676	0.10995	0.00267	0.325211	1111.3	145.92	673	16	86	u
46	0.97161	0.02161	0.10717	0.0015	0.629296	798.1	43.71	656	9	95	u

47	0.92167	0.02564	0.10815	0.00157	0.521832	667	57.26	662	9	100	c
48	0.93965	0.02778	0.11049	0.00163	0.498998	662.8	61.12	676	9	100	u
49	1.08048	0.03591	0.10726	0.00167	0.468468	1014.8	65.89	657	10	88	u
50	1.05766	0.03194	0.10747	0.00162	0.499159	967.4	59.99	658	9	90	u
51	1.13001	0.033	0.10606	0.00157	0.506893	1128.8	56.9	650	9	85	u
52	1.35805	0.04508	0.11038	0.00177	0.483075	1409.8	62.5	675	10	77	u
53	0.91586	0.02379	0.1062	0.00153	0.554628	693.5	52.88	651	9	99	u
54	1.25195	0.03315	0.10838	0.00161	0.561022	1288	49.84	663	9	80	r
55	1.32097	0.04219	0.09816	0.00162	0.51673	1579.3	58.77	604	10	71	r
56	1.25698	0.02402	0.10527	0.00147	0.730749	1352.6	33.53	645	9	78	u
57	0.94106	0.02669	0.10516	0.00155	0.519697	772	57.54	645	9	96	u
58	0.91752	0.02739	0.10105	0.00146	0.483994	802.8	61.06	621	9	94	u
59	0.96202	0.03176	0.10494	0.00157	0.453171	822.9	67.57	643	9	94	u
60	0.96253	0.01827	0.10419	0.0014	0.707909	839.6	36.33	639	8	93	u

Table 4: LA-ICPMS data for Abt-0Z_1; $^{206}Pb/^{238}U$ zircon analysis. Age error is displayed at 1σ.

Abt-Z1	Isotopic Ratios					Ages					
Analysis_#	Pb207/U235	1σ error	Pb206/U238	1σ error	rho	Pb207/Pb206 Age (Ma)	± Ma	Pb206/U238 Age (Ma)	± Ma	Conc. %	Rime/Core
1	1.10393	0.03961	0.11652	0.00174	0.416184	892.4	73.27	710.5	10.02	94	c
2	0.93667	0.01788	0.10228	0.00131	0.670965	819.4	37.62	627.8	7.66	94	c
3	1.29685	0.03999	0.1139	0.00165	0.469784	1263.7	59.74	695.3	9.53	82	c
4	1.00147	0.0581	0.10878	0.00205	0.324838	837.3	118.77	665.6	11.91	94	u
5	1.08209	0.07551	0.11099	0.00235	0.303419	951.1	139.35	678.5	13.63	91	u
6	0.96108	0.04908	0.11017	0.00191	0.339488	725.3	106.65	673.7	11.09	99	c
7	0.9465	0.02358	0.10828	0.00142	0.526401	727.8	51.58	662.8	8.27	98	c
8	1.08254	0.03605	0.11212	0.00164	0.439238	934.4	67.49	685.1	9.5	92	u
9	0.93108	0.02784	0.10593	0.00146	0.460948	739.6	62.26	649	8.53	97	u
10	0.9145	0.02703	0.10339	0.00143	0.467945	753.2	61.38	634.2	8.33	96	c
11	1.11629	0.0326	0.11574	0.00165	0.488157	928.8	58.75	706	9.52	93	c
12	1.07451	0.06072	0.10827	0.00212	0.346503	989.2	113.19	662.7	12.32	89	c
13	1.02928	0.06544	0.1008	0.00207	0.322998	1044.1	125.88	619.1	12.1	86	c
14	1.10323	0.0677	0.1114	0.00221	0.323284	982.3	122.55	680.8	12.83	90	c
15	1.0635	0.08924	0.12199	0.00279	0.272557	716.1	171.78	742	16.04	101	u
16	0.98034	0.02437	0.11033	0.00151	0.55056	757.5	50.52	674.7	8.75	97	u
17	1.14035	0.04112	0.0847	0.00141	0.461658	1583.6	67.26	524.1	8.39	68	u
18	1.05461	0.03946	0.0965	0.00157	0.434818	1181.2	73.19	593.9	9.21	81	c
19	1.176	0.04552	0.10717	0.00171	0.412219	1187.5	75.39	656.3	9.97	83	c
20	1.19564	0.03342	0.10754	0.00154	0.512324	1213.3	53.77	658.5	8.95	82	c
21	1.04417	0.04269	0.11587	0.0018	0.379968	786.9	84.88	706.8	10.38	97	u
22	0.84905	0.01339	0.09644	0.00116	0.7627	738.7	31.65	593.5	6.81	95	c
23	0.95942	0.0427	0.10237	0.00168	0.368738	868.8	91.32	628.3	9.81	92	u
24	0.91829	0.04921	0.1099	0.00197	0.334499	625.2	113.27	672.2	11.44	102	r
25	1.78308	0.08425	0.13809	0.00267	0.409213	1500.5	89.23	833.9	15.15	80	c
26	1.0598	0.10813	0.1013	0.00285	0.275748	1093	196.12	622	16.7	85	u
27	0.87616	0.03835	0.10315	0.00165	0.365454	661.2	92.3	632.9	9.64	99	c
28	0.87923	0.07569	0.10365	0.00241	0.270092	658.6	177.9	635.8	14.05	99	c
29	1.58826	0.0818	0.11141	0.00233	0.406069	1688.3	96.19	680.9	13.53	71	c
30	0.96805	0.03637	0.1085	0.00164	0.402317	765.5	77.91	664	9.56	97	c
31	0.92673	0.02796	0.10655	0.00148	0.460388	713.5	63.18	652.7	8.61	98	c
32	0.95186	0.03067	0.11177	0.00155	0.430394	667.4	68.94	683	9.01	101	c
33	0.90267	0.03716	0.10192	0.00162	0.386108	756.6	86.08	625.6	9.49	96	c
34	1.19251	0.0721	0.12327	0.00247	0.331411	936.8	121.64	749.4	14.17	94	c
35	1.10498	0.07057	0.11889	0.00241	0.317399	852.3	130.08	724.2	13.87	96	c
36	0.85416	0.05204	0.09952	0.00183	0.301816	684.4	127	611.6	10.72	98	c
37	0.84777	0.043	0.09437	0.00166	0.346804	784.1	105.46	581.3	9.79	93	c
38	1.11873	0.02951	0.12267	0.00166	0.51301	812.9	53.98	745.9	9.56	98	c
39	0.85097	0.03177	0.09271	0.00142	0.41026	826.7	77.27	571.5	8.35	91	c
40	0.8983	0.03824	0.1054	0.00167	0.372203	669.3	89.79	646	9.73	99	c
40	0.94549	0.05917	0.10125	0.00196	0.309326	861.2	126.75	621.8	11.5	92	u
41	1.03857	0.05583	0.11583	0.00209	0.335655	777.2	111	706.5	12.09	98	u
42	0.88405	0.02049	0.10299	0.00135	0.565553	683.8	48.09	631.9	7.87	98	c
43	0.85177	0.05294	0.08178	0.00167	0.328555	1084	122.66	506.7	9.97	81	c
44	1.08869	0.1402	0.09243	0.00345	0.289843	1323.2	237.92	569.9	20.34	76	c

45	0.86655	0.03427	0.10174	0.00155	0.385229	659.8	84.4	624.6	9.06	99	c
46	1.07961	0.06095	0.11598	0.00218	0.33294	854.9	115.18	707.4	12.58	95	u
47	0.92882	0.01703	0.08238	0.00105	0.695159	1241.3	34.25	510.3	6.23	77	c
48	0.91569	0.03971	0.10388	0.00166	0.368489	740.3	90.28	637.1	9.72	97	c
50	1.11341	0.0529	0.11119	0.002	0.378585	1004.8	96.53	679.7	11.6	89	c
51	0.92812	0.03855	0.10342	0.00163	0.379457	778.4	86.23	634.4	9.52	95	c
52	0.86899	0.03329	0.10236	0.00152	0.387627	660.3	81.92	628.2	8.86	99	c
53	0.94839	0.02812	0.10793	0.00152	0.474978	733.9	61.52	660.7	8.86	98	c
54	0.872	0.03435	0.10134	0.00157	0.393286	688.9	82.66	622.2	9.2	98	c
55	0.9683	0.03335	0.10057	0.00155	0.447484	923.2	69.91	617.7	9.07	90	c
56	0.92829	0.04656	0.10703	0.00183	0.340892	706.7	104.76	655.5	10.63	98	c
57	0.99928	0.0772	0.11024	0.00245	0.287671	799.1	156.99	674.1	14.21	96	c
58	1.0081	0.06763	0.10662	0.0022	0.307573	887.2	135.64	653.1	12.81	92	c
59	0.99297	0.02595	0.09571	0.00133	0.531732	1076.1	51.31	589.2	7.84	84	c
60	1.03524	0.08272	0.11164	0.00266	0.298189	846.6	161.8	682.3	15.44	95	c
61	1.51167	0.10328	0.12994	0.00293	0.330039	1300.5	134.02	787.5	16.71	84	c
62	1.15534	0.04119	0.12112	0.00178	0.412213	904.2	78.08	737	10.24	95	c
63	0.9161	0.03856	0.10318	0.00161	0.370712	754.8	87.91	633	9.43	96	c
64	1.37756	0.05496	0.11852	0.00188	0.397585	1301	79.24	722.1	10.83	82	c
65	1.0805	0.02384	0.09882	0.00128	0.587062	1180	43.27	607.5	7.53	82	c
66	2.91088	0.06886	0.24183	0.00324	0.566359	1367.7	45.38	1396.2	16.8	101	c
67	0.92076	0.08905	0.11002	0.00282	0.265027	628.1	200.51	672.8	16.38	102	c
68	1.07412	0.08791	0.11556	0.00269	0.284419	851.8	165.12	705	15.53	95	c
69	1.27999	0.04062	0.13501	0.00191	0.445794	891.9	66.8	816.4	10.84	98	c
70	1.02979	0.033	0.11236	0.00156	0.433259	825.1	68.07	686.4	9.02	95	c

Table 5: LA-ICPMS data for Abt-057; $^{206}Pb/^{238}U$ zircon analysis. Age error is displayed at 1σ.

Abt-057	Isotopic Ratios					Ages					
Analysis_#	Pb207/U235	1σ error	Pb206/U238	1σ error	rho	Pb207/Pb206 Age (Ma)	± Ma	Pb206/U238 Age (Ma)	± Ma	Conc. %	Rime/ Core
1	1.31392	0.01899	0.12316	0.00163	0.915718278	1131.6	24.38	748.8	9.33	88	c
2	1.49991	0.02381	0.15123	0.00209	0.870590932	985.1	27.63	907.9	11.73	98	c
3	1.28497	0.02207	0.08723	0.00122	0.814300335	1746.8	29.2	539.2	7.21	64	c
4	1.47101	0.02097	0.11477	0.00154	0.94125985	1487.6	22.33	700.4	8.88	76	c
5	1.00177	0.02096	0.10209	0.00145	0.678830805	963	41.24	626.6	8.46	89	c
6	1.01427	0.01657	0.0918	0.00124	0.826818291	1201.1	28.97	566.2	7.32	80	c
7	1.46598	0.02146	0.10742	0.00141	0.896669283	1605.8	23.82	657.7	8.22	72	c
8	1.22093	0.02359	0.10833	0.00155	0.740535324	1240.5	35.46	663	9.01	82	c
9	1.03852	0.01551	0.11207	0.00147	0.878276029	845	26.95	684.7	8.5	95	r
10	1.44994	0.02783	0.10831	0.00157	0.755210329	1570.4	34.18	662.9	9.11	73	u
11	1.09902	0.01584	0.10466	0.00137	0.908218314	1099.4	24.77	641.6	7.99	85	c
12	1.14621	0.01522	0.11953	0.00154	0.97027165	915.3	22.21	727.9	8.89	94	c
13	1.13128	0.01548	0.10933	0.00144	0.96254778	1070	22.29	668.9	8.37	87	c
14	1.97903	0.03144	0.11714	0.00159	0.854400994	1993.2	26.2	714.1	9.15	64	c
15	1.20499	0.0224	0.10526	0.0015	0.766590297	1270.5	33.74	645.2	8.77	80	c
16	3.71603	0.0586	0.13939	0.00196	0.891673888	2771.1	24.68	841.2	11.07	53	c
17	1.0914	0.01699	0.11527	0.0016	0.891649684	889.6	26.99	703.3	9.25	94	c
18	1.09803	0.01579	0.11686	0.00154	0.91640387	873.4	25.09	712.4	8.92	95	c
19	1.63802	0.03358	0.12387	0.00183	0.720648456	1546.5	37.54	752.8	10.5	76	c
20	1.2488	0.01973	0.12023	0.00171	0.900220851	1078.1	25.99	731.9	9.85	89	u
21	1.08258	0.02264	0.1014	0.00147	0.693207027	1132.7	40.08	622.6	8.62	84	c
22	1.26464	0.0177	0.0994	0.00128	0.920062295	1473.5	23.14	610.9	7.51	74	c
23	1.29428	0.02646	0.12973	0.00194	0.731475378	996.3	38.55	786.3	11.05	93	c
24	1.26049	0.01698	0.07621	0.00104	0.987135802	1955.8	18.05	473.5	6.22	57	c
25	1.01092	0.01612	0.10718	0.00145	0.848410434	881.4	28.85	656.4	8.47	93	c
26	1.08977	0.01884	0.11171	0.00164	0.84919171	950	30.05	682.7	9.49	91	c
27	1.12218	0.01983	0.09614	0.00139	0.818183077	1307.8	30.52	591.7	8.19	77	r
28	1.16783	0.01932	0.09396	0.00128	0.823454234	1428.9	28.77	578.9	7.56	74	c
29	1.97509	0.05113	0.16328	0.00278	0.657692519	1375.8	48.4	975	15.4	88	c
30	1.19615	0.01949	0.11735	0.0016	0.836778849	1039.5	29.18	715.3	9.23	90	c
31	1.71524	0.03432	0.12729	0.00183	0.718512652	1580.7	36.84	772.4	10.45	76	c
33	0.96997	0.0145	0.10363	0.00138	0.890807548	867.2	26.82	635.6	8.05	92	c
34	0.97804	0.0189	0.10169	0.00145	0.73787801	922.6	37.2	624.3	8.49	90	c
35	1.58208	0.02522	0.15495	0.00209	0.84613189	1043.7	28.63	928.6	11.67	96	c
36	0.96086	0.02255	0.10031	0.00148	0.628682039	913.4	47.38	616.2	8.7	90	c
37	1.00692	0.02162	0.10434	0.00149	0.665081264	928.6	42.89	639.8	8.67	90	c
38	1.12546	0.01854	0.11421	0.00153	0.813219219	971.8	30.62	697.1	8.85	91	c
39	0.96066	0.01365	0.10506	0.00136	0.911042356	817	25.56	644	7.91	94	c
40	1.52561	0.02801	0.1331	0.00183	0.74886486	1272.7	34.18	805.6	10.4	86	c
41	0.97254	0.02033	0.0967	0.00139	0.687635707	1013.5	40.51	595	8.17	86	c
42	0.99537	0.01544	0.10956	0.00146	0.859088852	803.8	28.55	670.2	8.47	96	c
43	1.13952	0.01988	0.11553	0.00158	0.783913034	973.6	32.71	704.8	9.13	91	c
44	1.19166	0.02152	0.1097	0.00151	0.762220131	1166.8	33.55	671	8.77	84	c
45	1.21976	0.02474	0.10535	0.00162	0.758150048	1292.1	36.18	645.7	9.43	80	c
46	1.17582	0.0166	0.11635	0.00157	0.955797785	1022.8	22.61	709.5	9.08	90	c

47	1.30126	0.02969	0.13266	0.002	0.660760214	962.4	44.74	803	11.36	95	u
48	1.2446	0.01735	0.13203	0.00179	0.972547284	881.7	22.26	799.5	10.19	97	c
49	1.61999	0.03241	0.12067	0.00178	0.737316567	1574.9	35.84	734.4	10.24	75	c
50	1.27874	0.0171	0.12831	0.00169	0.984945816	994.7	21.06	778.2	9.66	93	c
51	1.35607	0.02204	0.10276	0.00139	0.832264217	1543.1	27.9	630.5	8.1	72	c
52	1.37168	0.02317	0.11394	0.00161	0.836520202	1368.8	28.74	695.6	9.3	79	c
53	1.06428	0.01456	0.12008	0.00161	0.980053362	752.1	22.49	731	9.24	99	c
54	1.03964	0.02481	0.10727	0.00166	0.648464228	938.8	47.25	656.9	9.65	91	u
55	1.0103	0.01585	0.10563	0.00141	0.850849836	910.7	28.46	647.3	8.22	91	c
56	0.90118	0.01241	0.10516	0.00137	0.946040552	680.7	24.02	644.6	8.01	99	c
57	1.18026	0.0194	0.10276	0.00144	0.852539197	1277.5	28.35	630.6	8.42	80	u
58	1.42834	0.02658	0.1093	0.00152	0.747308717	1525.5	33.67	668.7	8.85	74	u
59	1.5198	0.03234	0.11689	0.00173	0.695528882	1516.1	39.18	712.6	10.01	76	u
60	0.99672	0.01723	0.10014	0.00138	0.797185507	992.3	32.07	615.2	8.06	88	c
61	1.10723	0.01611	0.12268	0.00163	0.913179474	789.4	25.69	746	9.33	99	c
62	1.01165	0.01465	0.10453	0.00142	0.938080385	934.5	23.87	640.9	8.3	90	u
63	1.17601	0.0167	0.11671	0.00159	0.9593644	1017.5	22.84	711.6	9.19	90	c
64	1.15635	0.01656	0.12112	0.00158	0.910898941	904.9	25.11	737	9.11	94	c
65	1.45568	0.02238	0.14187	0.00196	0.898610183	1053.1	25.84	855.2	11.05	94	c
66	1.07091	0.02022	0.11254	0.00159	0.748276379	899.5	35.93	687.5	9.24	93	u
67	1.02297	0.02307	0.09973	0.00153	0.680269367	1052.8	43.24	612.8	8.99	86	c
68	1.35221	0.0326	0.13126	0.00207	0.654130635	1060.8	46.65	795	11.8	92	c
69	1.12345	0.02849	0.10828	0.00171	0.622743442	1074.9	49.79	662.7	9.95	87	c
70	1.44056	0.02254	0.14536	0.002	0.879351525	982.2	26.96	874.9	11.28	97	c
71	1.25487	0.01986	0.09543	0.00137	0.907099935	1536.6	24.75	587.5	8.06	71	c
72	1.12695	0.01641	0.11597	0.00165	0.977089517	943.2	22.8	707.3	9.5	92	c
73	1.79317	0.02982	0.16723	0.00236	0.848616826	1141.2	28.77	996.8	13.01	96	c
74	1.01279	0.01906	0.09558	0.00137	0.761640535	1117.5	34.68	588.4	8.05	83	c
75	10.8777	0.14433	0.48372	0.00644	0.99661567	2488	17.04	2543.4	27.97	101	c
76	1.92991	0.03959	0.16043	0.00249	0.756598225	1367.6	36.79	959.2	13.82	88	c
77	1.19942	0.024	0.10612	0.00157	0.739371074	1245.2	36.54	650.2	9.14	81	c
78	1.0642	0.01651	0.10013	0.00139	0.894801628	1123.7	25.98	615.2	8.13	84	r
79	1.06066	0.0152	0.11645	0.00162	0.970751621	808.4	23.04	710.1	9.34	97	r
80	1.08792	0.01548	0.10747	0.00147	0.961293687	1026	22.7	658	8.54	88	c
81	1.18073	0.01628	0.12087	0.00162	0.972059144	953.3	22.16	735.5	9.34	93	c
82	1.38379	0.03899	0.11168	0.00194	0.616514474	1423.9	53.61	682.5	11.26	77	c
83	1.58589	0.08197	0.12858	0.00333	0.501059081	1413.4	104.21	779.8	19.01	81	c
84	0.98035	0.03022	0.09657	0.00173	0.581153108	1031	61.49	594.3	10.15	86	c
85	1.43341	0.02363	0.11433	0.00165	0.87544819	1444.8	26.82	697.8	9.56	77	c
86	1.0371	0.02983	0.09948	0.00165	0.576654318	1083.5	57.41	611.4	9.7	85	c
87	1.04804	0.02274	0.10062	0.00152	0.696220286	1082.8	41.31	618	8.92	85	c
88	1.27908	0.02474	0.12029	0.00177	0.760749638	1123.9	35.45	732.3	10.17	88	c
89	1.24794	0.02085	0.11662	0.00163	0.836569859	1135.8	29.41	711.1	9.38	86	c
90	1.32511	0.02057	0.11756	0.00162	0.887714016	1238.5	25.97	716.5	9.32	84	c
91	1.04915	0.01635	0.09681	0.00134	0.888186988	1162.3	26.24	595.7	7.86	82	c
92	0.94262	0.01331	0.10751	0.00148	0.974925541	728.4	23	658.3	8.61	98	c
93	1.11999	0.04467	0.0848	0.00181	0.535156636	1542	77.36	524.7	10.78	69	c
94	1.04697	0.0172	0.10471	0.00145	0.842918592	1001.4	29.43	641.9	8.44	88	c
95	1.77976	0.0261	0.17005	0.0024	0.962399835	1093	22.63	1012.4	13.22	98	c

96	1.1614	0.01724	0.11605	0.00161	0.934598956	1002.6	24.2	707.8	9.31	90	c
97	0.99833	0.01481	0.10189	0.00144	0.952686461	959.5	23.69	625.5	8.41	89	c
98	1.03469	0.01957	0.10676	0.00154	0.762661076	937.8	35.65	653.9	8.95	91	c
99	0.95812	0.01369	0.1055	0.00146	0.968538422	802.5	23.16	646.6	8.52	95	c
100	1.50479	0.03014	0.13466	0.00199	0.737814379	1224	36.93	814.4	11.32	87	c

Table 6: S08-17, summary $^{40}Ar/^{39}Ar$ results.

S08-17	Plateau Age (Ma)	2σ	MSWD	Isochron Age (Ma)	2σ	MSWD
Muscovite	615.8	2.8	0.62	617.5	5.3	0.11

Table 7: S08-15, summary $^{40}Ar/^{39}Ar$ results.

S08-15	Plateau Age (Ma)	2σ	MSWD	Isochron Age (Ma)	2σ	MSWD
Muscovite	613.3	5.9	1.66	615.5	6.4	0.12

Table 8: Major element XRF data table. Symbol ‡ denotes the metasedimentary samples.

Major Element XRF Analyses from Fused Discs														
Sample Name		SiO_2 %	Al_2O_3 %	Fe_2O_3T %	MnO %	MgO %	CaO %	Na_2O %	K_2O %	TiO_2 %	P_2O_5 %	SO_3 %	LOI %	Total %
	Abt-005	51.77	14.67	10.51	0.16	3.37	4.51	2.93	3.80	2.73	0.68	0.12	4.03	99.29
	Abt-008	64.42	14.49	5.18	0.08	2.31	2.86	5.46	0.76	0.67	0.18	0.02	3.22	99.66
	Abt-009	47.76	16.99	12.10	0.13	5.72	5.71	3.43	0.66	1.99	0.36	0.04	4.84	99.72
	Abt-011	43.41	15.64	13.01	0.22	4.09	8.76	4.61	2.44	2.82	0.82	0.16	3.41	99.39
	Abt-012	42.66	14.51	13.75	0.19	6.43	10.25	3.03	1.46	3.30	0.54	0.10	3.53	99.74
‡	Abt-016	63.47	14.21	5.63	0.08	2.39	4.05	3.89	1.44	0.71	0.19	0.01	3.35	99.40
	Abt-017	42.70	13.84	12.64	0.17	6.65	9.57	2.71	1.01	2.73	0.45	0.22	7.16	99.83
	Abt-022	47.26	14.86	11.79	0.23	2.64	7.04	2.93	1.87	1.95	1.00	0.09	8.19	99.82
	Abt-026	52.84	13.91	6.36	0.11	6.27	6.59	3.62	0.83	0.69	0.25	0.14	8.13	99.73
	Abt-031	45.69	15.63	14.22	0.24	3.75	8.40	3.41	0.82	2.92	0.51	0.19	4.11	99.88
‡	Abt-033	56.79	15.63	8.79	0.09	4.55	2.45	2.70	2.30	0.81	0.20	0.10	5.00	99.41
‡	Abt-038	63.53	14.69	5.93	0.09	2.67	3.30	4.46	1.06	0.77	0.19	0.01	2.71	99.40
‡	Abt-039	64.20	15.05	5.52	0.08	2.49	3.32	4.44	1.18	0.70	0.19	0.00	2.42	99.58
‡	Abt-042	51.99	15.30	7.88	0.11	4.80	5.83	4.96	0.51	1.03	0.28	0.02	7.06	99.76
	Abt-048	52.91	14.75	9.89	0.22	2.14	3.76	5.46	0.68	1.44	0.96	0.09	6.56	98.86
	Abt-062	75.99	12.19	1.70	0.03	0.69	3.00	4.02	0.51	0.17	0.05	0.01	1.26	99.61
‡	Abr-Nd_1	63.33	14.42	5.73	0.08	2.59	3.86	4.25	0.86	0.70	0.19	0.03	3.59	99.63

Table 9: Trace element XRF data table. All elemental values are represented as ppm. Symbol ‡ denotes the metasedimentary samples.

Trace Element XRF Analyses from Press Pellets																			
Sample Name		**Zr**	**Nb**	**Y**	**Sr**	**Rb**	**U**	**Th**	**Pb**	**Ga**	**Ni**	**Zn**	**Ba**	**Sc**	**Co**	**V**	**Ce**	**Nd**	**La**	**Cr**
	Abt-005	335.0	59.5	44.8	890.1	97.1	2.3	5.8	5.2	20.1	32	107	1036	19.9	31	161	105	48	47	18
	Abt-008	150.8	7.6	25.8	221.6	18.6	2.4	4.3	7.3	12.7	39	59	236	13.9	48	106	40	18	12	108
	Abt-009	175.7	8.2	34.3	409.7	15.2	1.3	0.8	1.0	19.2	97	89	190	27.6	56	244	51	23	11	34
	Abt-011	450.2	124.0	43.6	1200.2	66.8	4.6	10.7	7.9	23.4	17	115	1014	15.4	44	170	162	74	86	3
	Abt-012	244.2	67.2	32.8	841.9	39.8	1.8	5.6	3.5	20.4	125	92	655	23.4	61	327	106	46	48	104
‡	Abt-016	160.2	6.9	26.6	284.0	38.2	2.2	4.2	7.6	16.0	42	66	432	13.9	44	113	42	18	15	135
	Abt-017	238.6	55.0	27.6	721.9	24.3	1.5	5.8	2.1	20.5	182	92	422	25.7	60	288	90	43	37	202
	Abt-022	389.0	60.5	54.2	470.7	29.7	1.3	5.3	5.6	21.2	3	177	134	18.0	35	67	122	63	49	0
	Abt-026	90.7	3.9	10.5	604.5	24.5	2.2	3.7	11.8	16.3	175	62	229	19.6	35	157	41	18	12	349
	Abt-031	259.8	36.4	39.4	567.4	12.9	0.6	3.2	-0.4	24.0	45	139	271	22.1	52	249	78	42	30	0
‡	Abt-033	162.9	9.8	30.7	99.3	65.6	3.4	5.9	10.0	20.9	78	112	517	21.4	25	185	55	23	19	112
‡	Abt-038	179.3	7.7	28.9	266.7	28.4	1.9	4.8	16.5	16.4	40	67	276	14.3	47	125	49	22	14	158
‡	Abt-039	156.7	6.3	26.1	284.6	32.2	2.4	5.2	5.8	16.0	35	62	329	12.6	37	112	39	20	13	116
‡	Abt-042	116.7	3.3	12.8	403.0	14.3	3.4	7.0	13.0	16.4	45	101	206	18.9	31	195	60	30	24	57
	Abt-048	549.2	61.9	83.9	305.9	13.1	2.5	5.8	-0.3	22.1	3	94	1021	15.8	20	29	134	81	59	1
	Abt-062	50.0	0.9	4.6	835.9	9.1	2.0	1.4	4.6	12.8	10	24	192	4.9	83	24	17	3	5	31
‡	Abr-Nd_1	155.4	7.5	25.2	258.8	24.4	0.8	3.9	8.1	14.3	56	56	303	11.5	29	110	39	19	13	211